Lehrstuhl für Hochfrequenztechnik der Technischen Universität München
Univ.-Prof. Dr. techn. Peter Russer

A Si Schottky Diode Demultiplexer Circuit for High Bit Rate Fiber Optical Receivers

Jung Han Choi

Vollständiger Abdruck der von der Fakultät für Elektrotechnik und Informationstechnik der Technischen Universtät München zur Erlangung des akademischen Grades eines

Doktor-Ingenieurs

genehmigten Dissertation.

Vorsitzender: Univ.-Prof. Dr.-Ing. Fernando Puente León
Prüfer der Dissertation: 1. Univ.-Prof. Dr. techn. Peter Russer
2. Univ.-Prof. Dr.-Ing. Norbert Hanik

Die Dissertation wurde am 15.06.2004 bei der Technischen Universität München eingereicht und durch die Fakultät für Elektrotechnik und Informationstechnik am 31.08.2004 angenommen.

Abstract

A novel demultiplexer circuit for high bit rate fiber optic receiver applications using Si Schottky diodes has been developed and investigated experimentally. A sampling circuit based demultiplexer circuit theory is presented and simulated for a direct detection optical receiver with optical preamplification. For the experimental demonstration of the demultiplexer, very high-speed Si Schottky diodes are modeled applying the *Root-diode model*. The diode parameters were obtained using a parameter extraction software, and compared with the measurement data for various bias conditions until 40 GHz. The *flip-chip* bonding connections were simulated with a three dimensional electro-magnetic simulator, and an equivalent circuit model was established and used for the simulation of the complete demultiplexer circuit. The Root-diode model including the flip-chip equivalent circuits showed a good agreement with the measurement data up to 50 GHz. The hybrid technology using alumina substrates (Al_2O_3) of 250 μm thickness was used for the implementation. Conductor-backed coplanar waveguides were designed, fabricated and characterized by measurements. A 3 dB cutoff frequency of 72 GHz, and a reflection coefficient (S_{11}) of –20 dB until 70 GHz were obtained.

Using the extracted diode model and the developed flip-chip bonding equivalent circuit, the diode sampling circuit was designed and simulated. For the purpose of reducing deterministic *intersymbol interferences*, an equalizer circuit with zero-forcing algorithm was designed and simulated. The simulation results showed an enhanced eye diagram. The designed sampling circuit was fabricated, and measured using a 43 Gbit/s pseudo random binary sequence (PRBS) input signal. The measurement results displayed the demultiplexed signal output, as expected in the simulation.

The advantage of the demultiplexer concept described in this work is that it does not require high-speed active three-terminal devices (e.g. HBTs, HEMTs). The complete demultiplexer circuit is based on Schottky diodes only. The only active circuit required in this concept is the clock oscillator which needs to provide a clock signal at half the bit rate. If the clock oscillator is realized as a push-push oscillator [13], the transistors need to generate oscillation at a frequency corresponding to only a quarter of the bit rate. Therefore this concept opens the door for future Si-based monolithically integrated demultiplexer for bit rates up to 160 Gbit/s. Using the matured Si technology, the high-speed digital circuit can be constructed by an analog circuit using two-terminal devices, namely Si Schottky diodes. This

method is expected to reduce the bottleneck in the electronic part of optical communication links. Many issues during circuit design and test, such as power consumption, yield, and reliability, can be solved and never-reached high-speed circuits might be implemented in this way.

Table of Contents

Chapter 1 Introduction

1.1. Introduction

A rapid success and development in internet communications increasingly require higher speed signal transmissions and processings. In optical communications, to catch up with those necessities, research activities are evolved into two ways: One is to increase data bit rates in time domain, e.g. by ETDM (*electrical time-division multiplexing*) or OTDM (*optical time-division multiplexing*). The other way is to increase the data rate by WDM (*wavelength domain multiplexing*). An overalll data rate of 3 Tbit/s has been demonstrated in a recent experiment by combining of TDM and WDM [1]. An ultimate limitation behind this arises from the speed of electronic circuitry. It becomes a bottleneck in optical communication links. Up to now, it is the advent of the higher speed devices that determines and overcomes the electronics speed limit. Therefore, many research activities are actually focused on the development of faster three-terminal devices. Reported records for multiplexer and demultiplexer circuits are summarized in Table. I including employed device technologies. The SiGe device technology shows a comparable performance to the InP *high electron mobility transistor* (HEMT) technology in the multiplexer circuit. Recently 350 GHz cutoff frequency of SiGe *heterojunction bipolar transistor* (HBT) is announced [2]. That is expected to play a major role in 80 Gbit/s and 160 Gbit/s digital logic circuit implementations over InP device technology. The potential of Si CMOS devices also grows up rapidly, and it gets much attraction for the alternative due to its high yield, mass production, and high integration density.

Table. I Reported records for multiplexer and demultiplexer

Semiconductor	Technology	f_T/f_{max} (GHz)	Multiplexer	Demultiplexer
SiGe HBT	0.13 μm [3]	210 / 160	108 Gbit/s	·
	0.3 μm [4]	68 / 74	·	60 Gbit/s
	0.18 μm [5]	120 / 100	50 Gbit/s	50 Gbit/s
Si CMOS	0.12 μm [6]	100 / 50	40 Gbit/s	40 Gbit/s
InP HEMT	0.1 μm [7]	160/200	120 Gbit/s	110 Gbit/s
GaAs HEMT	0.1 μm [8]	206 / 203	80 Gbit/s	80 Gbit/s

Most of multiplexer and demultiplexer circuits listed in Table. I are built using transistor *logic* cells, such as a master-slave flip-flop (MS-FF) or an emitter-coupled logic (ECL). For the future development of 160 Gbit/s circuits faster electronic switching devices or concepts are necessarily required in broadband fiber optic transmission links. Improving device speed performance needs smaller gate length in HEMT devices, smaller transit time in HBTs, and much lower parasitic components. Even the modern E-beam technology and photolithography methods suffer from achieving both the gate length reduction and high reproducibility, simultaneously. A scaling of the device dimension does not directly lead to the switching speed improvement any more. Therefore, in order to overcome those deficiencies new design concept is mandated in high-speed digital logic circuit implementation.

Si Schottky diodes already reach THz cutoff frequency band [9][10]. They are also commercially available. Constructing digital circuits using Si Schottky diodes in an analog way is a very challenging and promising issue due to the above viewpoint. One of possible ways to consider is to design a digital circuit using Si Schottky diodes as switching elements, namely using *a sampling technique*.

1.2. Motivations

One principle motivation is to demonstrate a demultiplexing functionality using Si Schottky diodes in an analog way. Because Si Schottky diodes have cutoff frequencies greater than 1 THz, it is certain that a proper analog signal processing method and circuit topology will perform the high-speed demultiplexing function. A sampling circuit built with Si Schottky diodes is a good candidate for the realization of the demultiplexing function. A sampling technology is generally employed in high-speed measurement instruments as high as 60 GHz [12]. In order to overcome a frequency limitation of electronics, the sampling circuit controlled by short time pulses was developed. The sampling circuits' application area will be broadened in future [10][11], and the its application to the demultiplexer circuit is a good example to consider.

Si technology is emerging for microwave and millimeter-wave integrated circuits. Silicon monolithic millimeter-wave integrated circuits (SIMMWICs) have been found in many applications such as sensorics and communications [9]. From active devices to passive circuits they have been integrated on a semi-insulating Si substrates. A Si Schottky diode based sampling circuit also can be integrated with other receiver circuit parts. A push-push oscillator circuit is a good example to consider [13]. It generates two oscillating signals

simultaneously, and one output frequency is one half of another output. If the sampling circuit based demultiplexer circuit is combined with the push-push oscillator circuit, a demultiplexing function can be extended from 1:2 to 1:4. In this way, over 43 Gbit/s ETDM optical receiver circuit will be constructed and integrated using the Si technology. This is a significant aspect of the SIMMWIC for optical communication link applications. This concept would be strongly anticipated to work soon.

In this work, we focus on a function of 43 Gbit/s demultiplexing using a flip-chip bonding technology. However, in principle this sampling circuit concept is feasible in 80 Gbit/s and 160 Gbit/s demultiplexer circuit applications. We therefore present simulation results for an 80 Gbit/s demultiplexer circuit in Chapter 3 to show that the sampling circuit shall work for the higher bit rates. However, the circuit for higher bit rates above 80 Gbit/s should be fabricated in MMIC to minimize the parasitics.

Besides this, we should mention the advantage of the analog approach. It provides merits over digital methods. In fact, the logic circuit consists of cascaded logic blocks. However, if we use diodes instead of transistors as the switching device, we can considerably reduce the used number of devices. In consequence, in realizing the demultiplexer the sampling circuit concept shall reduce the complexity of the circuit. It is noted that in the analog approach the post signal processor will be combined with the sampling unit. So the overall system will be complicated. However, it has still advantages over the conventional digital circuits in complexity.

1.3. Structure of the work

In Chapter 2, we describe a theory for the sampling circuit based demultiplexer, first of all. We introduce an optically preamplified direct detection system for the theory description. Essential elements for this system are discussed and introduced. We introduce receiver part components, such as an erbium-doped fiber amplifier (EDFA), an optical band pass filter, and a high-speed and high-power photodiode (PD). Analytical expressions for the sampling circuit based demultiplexer are derived and calculated. Simulation results are presented and algorithm routines are provided in Appendix B We also discuss a linear signal equalizer following the sampling circuit. Two algorithms are explained to calculate equalizer coefficients.

In Chapter 3, the Si Schottky diode modeling process is discussed. A theoretical background for the Root-diode model is provided in detail. Modeling procedures are

described for *IC-CAP* program. The diode DC and AC measurement data are illustrated and summarized. Diode modeling results were compared with the measurement data up to 50 GHz. Then, the flip-chip bonding model simulation was carried out. In order to establish an equivalent circuit model, we find out the discrete component values by interpolating the simulation results. Fabrication processes and simulation environments are explained. A flip-chip bonded Si Schottky diode module was measured and its result was compared with the modeling result. The sampling circuit design and the simulations were performed under both hybrid and MMIC fabrication conditions. The circuit design using the developed Root-diode model is presented. Simulation results are given in each step. A linear equalizer circuit is designed using the algorithm presented in Chapter 2. It is combined with the sampling circuit and the eye waveform is obtained and evaluated. We also propose a 80 Gbit/s *return-to-zero* (RZ) demultiplexer circuit and simulations are provided.

In the following Chapter 4, the measurement results are discussed. The fabricated conductor-backed coplanar waveguide (CPW) with via holes on an alumina substrate were measured, analyzed and compared with analytical results. Then, a resistive power divider circuit was discussed. This is an essential part in designing the hybrid 1:2 demultiplexer circuit. The S-parameter measurement result is presented. We test the power divider circuit using 43 Gbit/s *nonreturn-to-zero* (NRZ) and 86 Gbit/s RZ signals and the measured output waveforms are provided. The sampling circuit was fabricated and measured. The measurement set-up is described in detail. We discussed the measured transient output results.

Finally, in Chapter 5, the summary of the design and the experimental results are presented and the conclusion will be made. The outlook for the analog approach to the higher bit rate digital circuit will be discussed.

Chapter 2 The Principle of the Si Schottky Diode Demultiplexer

2.1. The Optical Receiver with Optical Preamplifier

2.1.1. Background

The transmission distance in a fiber optic transmission link is basically limited by fiber losses and fiber dispersion. In order to increase the maximum transmission distance, methods listed in Table. II are frequently combined or separately employed for system enhancement.

Long distance transmission links are realized by the availability of optical amplifiers. The advent of optical amplifiers in optical communications allows transatlantic and transpacific communications. The power level inside the fiber increases due to optical pumping and the optical signal amplification. Thus, fiber nonlinear characteristics, such as stimulated *Raman* scattering, stimulated *Brillouin* scattering, four-wave mixing, etc., get much attraction for long-haul transmission.

Table. II Systematic approaches to increase transmission distance in optical communications

Method	Examples
Optical amplifier	booster (transmitter), preamplifier(receiver), in-line amplifier
Channel coding	forward-error correction (FEC), enhanced FEC (EFEC)
Signaling	return-to-zero (RZ), carrier-suppressed RZ (CS-RZ), nonreturn-to-zero (NRZ)
Modulation	on-off keying (OOK), differential phase-shift keying (DPSK)
Dispersion management	dispersion-shifted fiber (DSF), positive-dispersion fiber (PDF), negative-dispersion fiber (NDF)

In this section, we will introduce the *optically preamplified direct detection* system (OPDD). Although many linear and nonlinear problems are necessarily explained to describe the OPDD system, we will focus on essential elements to deal with this system.

At first, the fundamental fiber losses will be described. Those losses are intrinsic causes reducing the transmission distance. It is significant to understand inherent reasons of the fiber loss. Secondly, as the transmission speed and distance are increased, the second-order properties, such as chromatic dispersion (CMD) and polarization mode dispersions (PMD) play important roles in determining system performance. Detailed explanation of each phenomenon will be given. Discussions will be made in the system performance viewpoint. The usage of the optical amplifier (OA) will be described. Even if the detailed operation principle of the OA is avoided, their system usages and the encountered problems in the system operation are discussed. Finally, high-speed and high-power photodetectors (PDs) are dealt in the following section. They are classified with their illumination geometries and transporting carrier types. Operation principles are explained and compared with each other. They are discussed with regard to the relation between bandwidth and maximum saturation current.

2.1.2. Fiber Losses and Dispersions

2.1.2.1. Fiber losses

In the fiber, losses occur due to the following reasons : *Rayleigh* scattering, ultraviolet absorption, infrared absorption, and waveguide imperfections [14].

Rayleigh scattering is an intrinsic and fundamental loss in the fiber due to the density fluctuations in silica fibers. These density fluctuations induce refractive index fluctuations in the fiber. Lightwave scattering due to this phenomenon is called *Rayleigh* scattering, and described by the attenuation coefficients,

$$\alpha_{Rayleigh} = \frac{C}{\lambda^4} . \qquad \textbf{(2.1)}$$

where the constant C is in the range of 0.7-0.9 dB/(km·㎛)^4. The α_{Rayleigh} value near λ=1.55 ㎛ is 0.12-0.15 dB/km, which is main contribution to the loss at this wavelength [15].

Silica molecules have electronic resonance in ultraviolet region below 0.4 ㎛ and vibration resonance above 7 ㎛ wavelength (infrared region). These resonances yield absorption depending on wavelength. The absorption extends to our spectral interest region from 1.3 to 1.55 ㎛. The loss due to the ultraviolet resonance and the infrared loss (intrinsic loss) in pure silica is smaller than that due to *Rayleigh* scattering. However, the vibration spectral peak caused by OH ion, forms a detrimental extrinsic loss in the fiber, which has harmonic components at 1.39, 1.24, and 0.95 ㎛ [14]. Reducing the loss due to OH ions is very significantly associated with a low loss fiber.

Waveguide imperfections include core radius fluctuations in cable, macro bending loss, and micro bending loss. In practice, core-cladding layer imperfections in the fiber cable can generate net optical loss. During the fiber fabrication attention should be paid to control uniform core radius. Macro bending loss represents a radiation loss due to a bend. The part of the mode is scattered into the cladding layer. This scattered energy loses its power. The radiation loss coefficient is given by [16]

$$\alpha_{BEND} = c_1 \cdot \exp(-c_2 R) \qquad \textbf{(2.2)}$$

where, c_1 and c_2 are constants which are not dependent on R, and R is bending radius.

Whereas the macro bending satisfies $R \gg$ a (fiber core radius) condition, micro bending loss occurs when $R \sim$ a. That is attributed to the localized defects in the fiber. In a single mode fiber, the micro bending loss can be minimized by confining the energy to the core. It means that a parameter, so-called *normalized frequency parameter* (v) in fiber design, has the value between 2 and 2.405 [14].

$$\mathrm{v} = k_0 a (n_1^{\,2} - n_2^{\,2})^{1/2} \qquad \textbf{(2.3)}$$

where, a is core radius, n_1 and n_2 are a refractive index in the core and cladding layer, respectively.

Power attenuation caused by above reasons in the fiber is governed by

$$dP/dz = -\alpha \cdot P \qquad (2.4)$$

where α is the attenuation coefficient and P is the optical power inside the fiber. When the launched power to the input of the fiber of the length L, then the output power of the fiber is

$$P_{out} = P_{in} \cdot \exp(-\alpha \cdot \mathrm{L}). \qquad (2.5)$$

Expressing the α in units of dB/km, the following relation is obtained [14].

$$\alpha(dB/km) = -10/L \cdot \log 10(P_{out}/P_{in}) = 4.343\alpha \qquad (2.6)$$

In the spectral window of modern optical communications, λ=1.31 ㎛ and 1.55 ㎛, the attenuation coefficients show 0.35 dB/km and 0.2 dB/km, respectively. Recently, efforts to reduce optical attenuation coefficient are exerted using a novel photonic crystal fiber (PCF). The best performances ever reported using the PCF are 0.71 dB/km and 0.37 dB/km for 1.31 ㎛ and 1.55 ㎛, respectively [17]. They reduced the optical attenuation coefficient by avoiding the inclusion of OH ion during fabrication processes. The absorption loss by OH ion was measured and found to contribute the loss of 0.12 dB/km at 1.55 ㎛. They also indicated that by eliminating the loss by OH ions and reducing the surface roughness in PCF, the optical loss of the PCF can be less than that of a conventional fiber. Even if the PCF nowadays does not show better performance than the normal fiber, it is expected that it will replace the current fiber in future.

2.1.2.2. Chromatic dispersion (CMD)

Chromatic dispersion is also called *group velocity dispersion* (GVD). This dispersion phenomenon is attributed to the interaction of the two underlying effects, namely the material dispersion and the waveguide dispersion. The chromatic dispersion parameter, D, is written as a linear sum of each dispersion parameter as

$$D = D_M + D_W \qquad (2.7)$$

where, D_M is a dispersion parameter of the material in the fiber (silica), and D_W is from the waveguide effect of the fiber.

As the dielectric medium has its own resonance frequencies, the refractive index, n, is dependent on the optical angular frequency, ω. This dependency is well suited with the *Sellmeier* equation [15],

$$n^2(\omega) = 1 + \sum_{j=1}^{M} \frac{B_j \omega_j{}^2}{\omega_j{}^2 - \omega^2} \qquad \textbf{(2.8)}$$

where ω_j is the resonance frequency and B_j is the oscillation strength.

This equation describes that spectral components travel different velocities, c/n(ω). Mode propagation constant, β, accounts for the effects of CMD. Expanding β using a *Talyor* series about the center frequency, ω_o, the following equation is obtained as,

$$\beta(\omega) = n(\omega)\frac{\omega}{c} = \beta_0 + \beta_1(\omega - \omega_0) + \frac{1}{2}\beta_2(\omega - \omega_0)^2 + \cdots \qquad \textbf{(2.9)}$$

where, $\beta_m = \left(\frac{d^m \beta}{d\omega_m}\right)_{\omega=\omega_0}$ $(m = 0, 1, 2, \ldots)$.

The parameter β_1 and β_2 are found with the relation of the refractive index and its derivatives with regard to the optical frequency are shown here.

$$\beta_1 = \frac{1}{\upsilon_g} = \frac{n_{1g}}{c} = \frac{1}{c}\left(n_1 + \omega\frac{dn_1}{d\omega}\right) \qquad \textbf{(2.10)}$$

$$\beta_2 = \frac{1}{c}\left(2\frac{dn_1}{d\omega} + \omega\frac{d^2 n_1}{d\omega^2}\right) \qquad \textbf{(2.11)}$$

where, n_{1g} is the group refractive index of the core, and υ_g is the group velocity. The β_1 is responsible for the group velocity whereas the β_2 represents the group velocity dispersion.

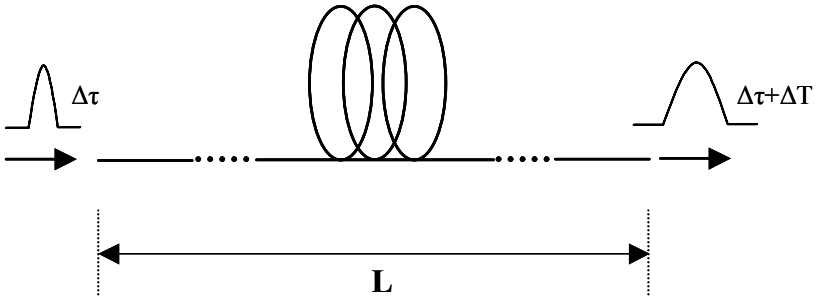

$$\Delta T_{CMD} = D \cdot \mathrm{L} \cdot \Delta\lambda$$

Fig. 2.1 Chromatic dispersion in the fiber broadens the optical pulse.

The material dispersion parameter is expressed as width

$$D_M = \frac{1}{c}\frac{dn_{2g}}{d\lambda} \qquad \textbf{(2.12)}$$

where n_{2g} represents the group index of the cladding material [14].

When the dispersion parameter, D_M, is zero, the corresponding wavelength is called a *zero-dispersion wavelength*, λ_{ZD}. This wavelength can be varied changing the doping materials in the core and cladding layer. Its range is about 1.27 – 1.29 ㎛ for pure silica [14]. It should be noted that the dispersion behavior at λ_{ZD} should include the third-order distortion (TOD) parameter, β_3 . Its inclusion is necessary only when the operating wavelength is a few nanometers different from the λ_{ZD} , for instance.

The contribution of the waveguide effect to the dispersion parameter D is given

$$D_W = -\frac{2\pi\Delta}{\lambda^2}\cdot\left[\frac{n^2{}_{2g}}{n_2\omega}\frac{Vd^2(Vb)}{dV^2} + \frac{dn_{2g}}{d\omega}\frac{d(Vb)}{dV}\right] \qquad \textbf{(2.13)}$$

where, $b = \dfrac{\beta/k_0 - n_2}{n_1 - n_2}$, k_0 is the free space propagation constant, and $\Delta = \dfrac{n_1 - n_2}{n_1}$ [14]. The D_W shows negative value in the wavelength region of our interest (1.1 – 1.7 ㎛). Therefore, the zero dispersion wavelength λ_{ZD} due to material dispersion is shifted into higher wavelength value. Incorporating the waveguide dispersion with the material dispersion

parameter, the λ_{ZD} can be shifted into 1.55 ㎛, at which most of modern optical communications are implemented. For example, using double-clad or quadruple-clad layer dispersion parameter, D, can have very small dispersion value in wide range of wavelength from 1.3 ㎛ to 1.55 ㎛. This is *so-called dispersion-flattened* fiber. This fiber is advantageous in (*dense*) *wavelength-division multiplexing* ((D)WDM) applications because wide rages of wavelengths are employed in the system.

The total dispersion parameter D is given by

$$D = D_M + D_W = \frac{d\beta_1}{d\lambda} = -\frac{2\pi c}{\lambda^2}\beta_2 . \qquad \textbf{(2.14)}$$

By its convention the total dispersion parameter is expressed using D although its sign is reversed compared with β_2. Its dimension is given *ps/(km)(nm)*. In fact, the dispersion has a positive value above λ_{ZD}. In this range the longer wavelength signal travels slower than the shorter wavelength. This anomalous behavior is of great interest in *soliton* communications, which cancel the pulse broadening effect combining with a signal chirping. The chirping is related with the fiber nonlinearities: the refractive index is also dependent on the optical power as well as the optical frequency. This is attributed to the third-order polarization dependence on the optical intensity [14]. Further discussion, however, is beyond of our consideration in this chapter, thus is omitted here.

2.1.2.3. Polarization mode dispersion (PMD)

Fundamental limitations of real fiber characteristics, such as core shape, ideal symmetry along the fiber, and uniform refractive index distribution, etc., cause polarization-dependent *nondegeneracy*. Even if the two orthogonally polarized fundamental modes are injected into the single mode fiber, each field mode experiences different mode index, and couples each other randomly. At the output of the fiber, each polarized mode arrives at a different time yielding the pulse broadening. This phenomenon is called *polarization mode dispersion* (PMD). Analytically, PMD related system performance restriction can be explained with regard to fiber modal birefringence. This property explains that orthogonal modes in x and y direction have a different propagation constant. It is defined as

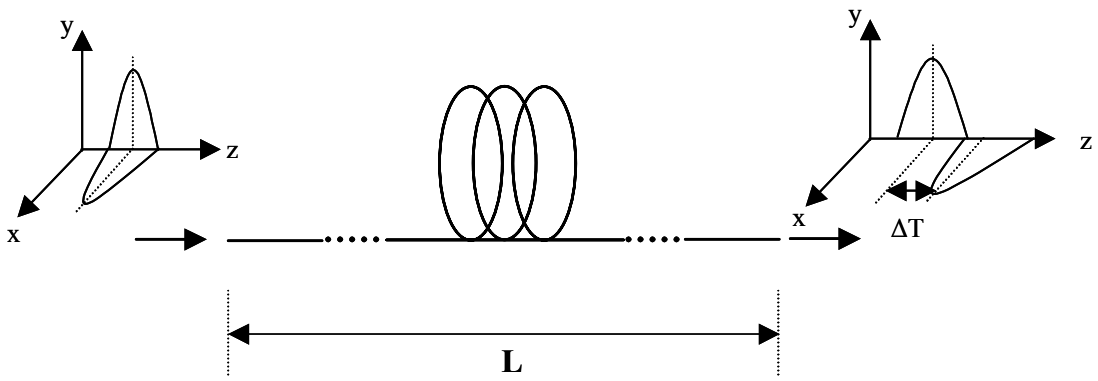

$$\sigma_{PMD}{}^2 = \left\langle (\Delta T)^2 \right\rangle = D_P \sqrt{\mathrm{L}}$$

Fig. 2.2 Each polarization mode has a different group velocity. Thus, after fiber length L each polarized mode arrives at different time.

$$B_m = \frac{\left|\beta_x - \beta_y\right|}{k_0} = \left|n_x - n_y\right| \qquad \textbf{(2.15)}$$

If we assume that B_m is constant along the fiber, the pulse broadening is shown

$$\Delta T = \left|\frac{L}{v_{gx}} - \frac{L}{v_{gy}}\right| = L \cdot \left|\beta_{1x} - \beta_{1y}\right| = L \cdot k_0 \frac{dB_m}{d\omega}. \qquad \textbf{(2.16)}$$

Since B_m is random along the fiber, it is desirable to express using its variance given by

$$\sigma_{PMD}{}^2 = \left\langle (\Delta T)^2 \right\rangle = \frac{1}{2}\Delta \cdot \beta_1{}^2 h^2 \left[\frac{2L}{h} - 1 + \exp\left(-\frac{2L}{h}\right)\right]$$

$$\approx \Delta \cdot \beta_1 \sqrt{hL} \quad (\mathrm{L} > 0.1\,\mathrm{km}) \qquad \textbf{(2.17)}$$

$$= D_p \sqrt{L}$$

where, h is the *de*correlation length and D_p is the PMD parameter [14]. It is noted that the variance of the PMD has a dependence of $L^{1/2}$ and is a limiting factor in long-haul transmission system operated in near $\lambda_{ZD.}$

In the optical receiver design viewpoint, this PMD is of significance because this is actually a random phenomenon in the installed fiber. Ultimately, uncontrolled PMD in the system degrades bit error rate (BER) in the receiver. An adaptive signal processing in the receiver side is an effective technique to mitigate the influence of the PMD. So far this technique is implemented in the two domain: one is optical signal domain, and the other is electrical domain. Further discussion will be done in later chapter.

2.1.3. Optical Amplifiers (OAs)

In early stage of long-haul transmission system development, an electronic regeneration has been used to overcome losses and dispersions. The regenerator converts the optical signal into the electrical signal (OE), then amplifies and regenerates the signal electronically, and finally converts the signal into an optical signal again (EO). These signal conversions (OEO), however, become problematic in multi channel lightwave systems, as the regenerator modules become quite complex and expensive. An emerged candidate instead of the electronic regenerators allowing long-haul transmission is an optical amplifier.

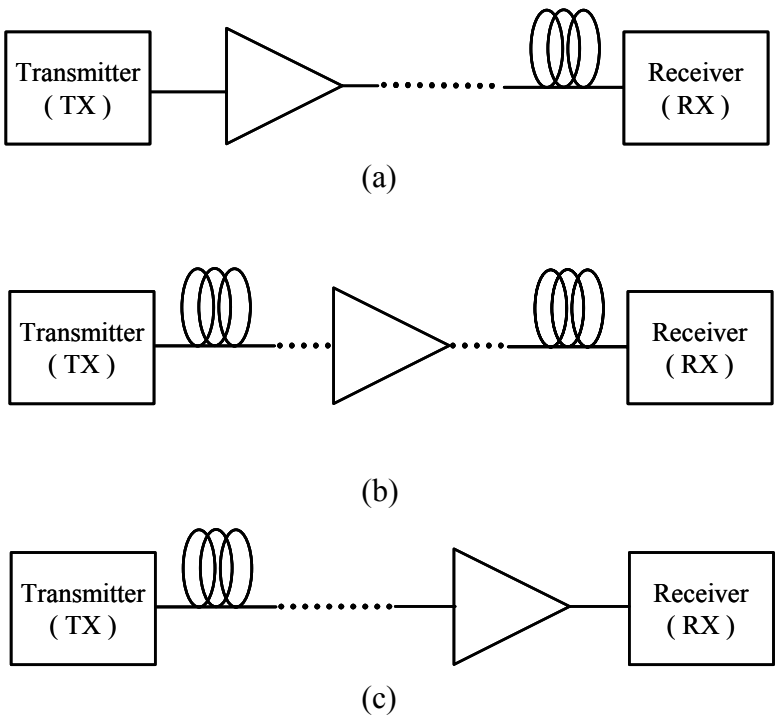

Fig. 2.3 Optical amplifier usages. (a) booster (b) in-line amplifier (c) preamplifier

Until mid-1990s, the development of erbium-doped fiber amplifier (EDFAs) looks more attractive over Raman amplification, because EDFA needs less pump power than the Raman optical amplifier does. After the success of high pump power development for the Raman amplification, the Raman amplifier employment in real transmission experiment has been increased considerably [18].

The usage for the optical amplifier is found as three ways. One is the optical booster in the transmitter part, that enables the system have longer transmission span. But, due to high optical power nonlinear problems occur : such as stimulated Raman scattering (SRS), stimulated Brillouin scattering (SBS), four-wave mixing (FWM), self-phase modulation (SPM), and cross-phase modulation (XPM). In a consequence, reducing the optical power in the transmission fiber and simultaneously satisfying the required optical signal to noise power ratio (OSNR) at the system output is of our concern. That will be accomplished by reducing the loss per span length, and(or) using in-line amplifications (e.g. the Raman amplification).

We find the second usage of the optical amplifier as in-line amplifier in [19]. They jointly used the EDFA and the Raman amplifier for the in-line amplification. After the Raman amplification along the transmission fiber, the C-band (1528 – 1561 nm) and the L-band (1561 – 1620 nm) amplifications are successively done respectively using EDFAs. Optical splitters are inserted for the separate band amplification. They have demonstrated 3.2 Tbit/s capacity transmission using standard single-mode fiber (SSMF) employing those optical amplifiers.

The third usage for the optical amplifier is the preamplification of the optical signal prior to the electronic receiver. By amplifying the optical signal, receiver sensitivity is enhanced and may approach to the limit of the optical heterodyne detection systems [20]. Furthermore, the resultant electrical signal after the optical amplifier is large enough to drive the following demultiplexer circuit and decision circuit without electrical preamplifier and limiting amplifier. Therefore, the receiver system becomes more simple in reality.

2.1.4. High-speed and high-power photodetectors

High-speed and high-power photodetector (PD) is an essential element to realize the OPDD receiver system. The optical amplifier (EDFA) in front the PD increases the optical

power falling upon the PD, and then increases the signal to noise ratio (SNR). The transmission distance is also increased in this way. High-power PDs can considerably reduce RF insertion loss, and increase the spurious-free dynamic range [21]. In the context, high-power photodiodes mean an output voltage of 200 mV_{pp} at 50 Ω.

As optical power incident upon the photodetector increases, the number of generated *electron-hole pairs* (EHPs) is increased. Those carriers in turn decrease the electrical field inside the transit region. The field is formed by reverse bias and accelerates the carriers generated by the incident optical light. The decreased electrical field accounts for the increased transit time through the intrinsic layer for *p-i-n* type PD (*electric field screening effect*). Therefore, the increased optical power in the OPDD system decreases the intrinsic electrical bandwidth of the PD, thus limits the high saturation current in the high-speed PD. The other factors to limit the maximum available saturation current are thermal effects in the PD, and the breakdown as the current density increases [22].

In fact, the PD bandwidth for *p-i-n* type PD is composed of two components, τ_{RC} and τ_{tr}, thus

$$f_{pin} = \frac{1}{2\pi(\tau_{tr} + \tau_{RC})} \qquad \textbf{(2.18)}$$

where, $\tau_{tr} = W / \upsilon_d$, W is a transit layer width, υ_d is a drift velocity corresponding to the

Table. III Photodetectors are classified with respect to the illumination geometry and transporting carriers

Illumination Geometry		
Surface-illumination	Carrier multiplication	Avalanche PDs (InP, Si, super-lattice)
	Carrier nonmultiplication	*p-i-n* PD , MSM PD (metal-semiconductor-metal)
Edge-illumination	Traveling-wave PD (TWPD) Waveguide PD (WGPD) Velocity-matched distributed PD (VMDP)	

Transporting Carriers		
	Single carrier	Uni-traveling carrier PD (UTC-PD)
	Two carriers (electron and hole)	*p-i-n* PD, MSM PD, edge-illuminated PDs
	Multiplied carriers	Avalanche PDs

electrical field, and $\tau_{RC} = (R_L + R_s) \cdot C_p$ is the time constant by the parasitic capacitance (C_p) and the series connection of the series resistance (R_s) and the load resistance (R_L).

For surface illuminated type PDs, the reduced transit time (smaller intrinsic layer length) can increase the electrical bandwidth of the PD. However, quantum efficiency (η) is reduced correspondingly. The quantum efficiency represents the ratio of electron generation rate to photon incidence rate, and can be defined as,

$$\eta = \frac{I_P / q}{P_{in} / h\nu} = \frac{h\nu}{q} \cdot R . \qquad \textbf{(2.19)}$$

where, $R = I_p / P_{in}$ is the responsivity of the PD and has a unit of [A/W].

Therefore, a trade-off between bandwidth and efficiency exists in the *p-i-n* type PD. In order to overcome this problem, a waveguide PD (WGPD) is proposed. Optical illumination is guided perpendicular to the carrier drift field, allowing a long absorption path along dielectric cladding layers. But, it still maintains a small junction area. So, the interdependence between the bandwidth and the internal efficiency is reduced.

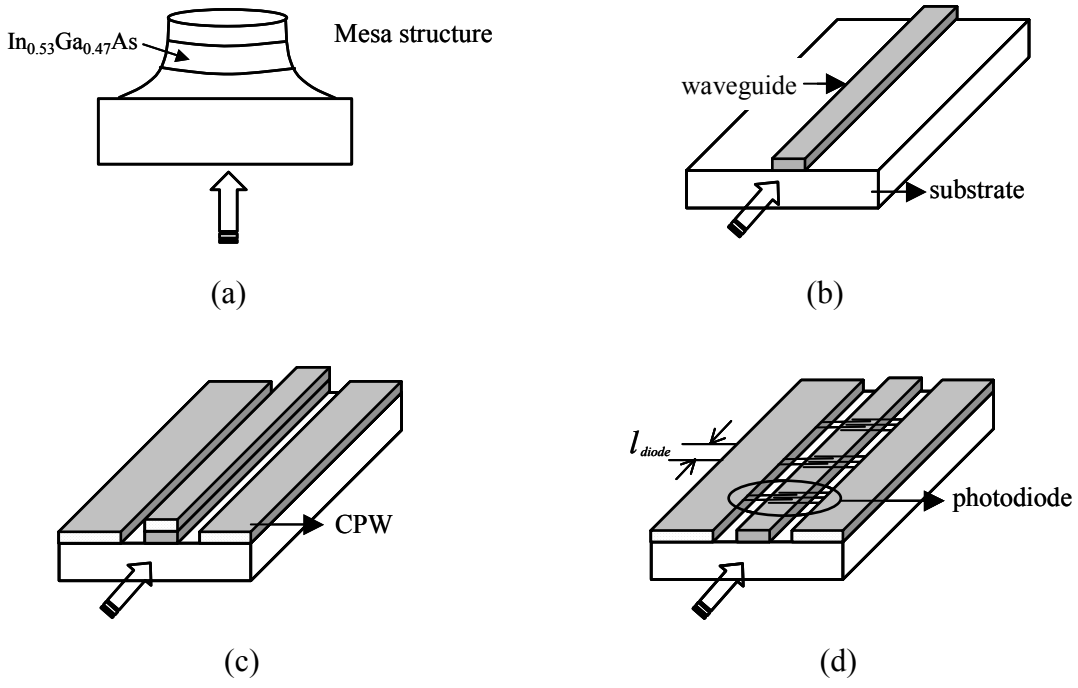

Fig. 2.4 (a) Back-side illuminated *p-i-n* type PD, (b) waveguide PD, (c) traveling-wave PD, and (d) velocity-matched PD

The quantum efficiency of the WGPD is written as

$$\eta_{WGPD} = 1 - e^{-\alpha \Gamma L} \qquad \textbf{(2.20)}$$

where, α is an absorption constant, Γ is a confinement factor of the light, and L is the whole optical dielectric waveguide. In general, the optical light confinement factor is given using the optical field distribution at the PD.

$$\Gamma = \frac{\int_{\substack{absorption \\ layer}} \left|\phi_{yj}(y)\right|^2 dy}{\int_{-\infty}^{\infty} \left|\phi_{yj}(y)\right|^2 dy} \qquad \textbf{(2.21)}$$

where, $\phi_{yj}(y)$ is the optical field in the waveguide, and y is the direction perpendicular to the diode junction layer. Physically, the confinement factor describes how much the incident optical power effectively couples to the absorption layer. In practice, the optical field at the WGPD is much narrower than the transverse extension of the optical field from the fiber. In [23], a multimode WGPD is proposed enlarging the optical field at the PD without sacrificing the bandwidth. High-doped quaternary InGaAsP forms double core around InGaAs absorption layer and confines the optical field in transverse direction. Thus, the increased coupling efficiency was obtained successively.

There is an inherent defect in the WGPD that the electrical signal is reflected if the electrical waveguide is not terminated correctly. This causes pulse broadening. Matching the characteristic impedance of the PD and supporting coplanar waveguide along the dielectric waveguide, a traveling-wave photodetector (TWPD) is designed and implemented [24]. The f_{3dB} in the TWPD can be expressed below

$$f_{3dB} = \frac{f_t}{\sqrt{1 + \left(\frac{f_t}{f_{VM}}\right)^2}} \qquad \textbf{(2.22)}$$

where, f_t is an electrical bandwidth limited by the carrier transit time, and f_{VM} is defined for matched termination at the output using electrical wave velocity (υ_e) and optical wave velocity (υ_o) in the semiconductor [22] as below,

$$f_{VM} = \frac{\Gamma \alpha \upsilon_e}{2\pi\left(1 - \frac{\upsilon_e}{\upsilon_o}\right)} \quad \textbf{(2.23)}$$

Velocity mismatch occurs because the electrical signal along the coplanar waveguide (CPW) travels in different velocity with the guided optical signal along the waveguide. As υ_e is given,

$$\upsilon_e = \frac{1}{\sqrt{L_{tr} \cdot C_{tr}}} = \frac{d}{\varepsilon_r \varepsilon_0 w Z_0} \quad \textbf{(2.24)}$$

where, d is the transit layer thickness, w is the width of the WGPD, and Z_0 is characteristic impedance of the CPW ($= \sqrt{L_{tr}/C_{tr}}$), the electrical velocity can be as close as to the optical light velocity in the waveguide choosing the proper CPW geometry parameters. The quantum efficiency of the TWPD (input matching case) is expressed by

$$\eta_{TWPD} = \frac{1 - e^{-\alpha \Gamma L}}{2}. \quad \textbf{(2.25)}$$

Considering the high power capability of the PD, we should consider saturation current in each type PD. For the TWPD [21],

$$I_{SAT,TWPD} = \frac{1}{2} q \cdot \int_{x=0}^{L} W \frac{d}{\Gamma} P_0 \cdot \alpha \Gamma e^{-\alpha \Gamma x} dx = \frac{W}{\alpha \Gamma} I_s \eta_{TWPD} \quad \textbf{(2.26)}$$

where, I_s is the saturation photocurrent density per unit area, and P_o is the incident photon flux per unit area at the saturation condition ($1/\mu m^2/\sec$). In the same way, for the WGPD [21],

$$I_{SAT,WGPD} = \frac{W}{\alpha\Gamma} I_s \eta_{WGPD} \quad \textbf{(2.27)}$$

As $\alpha\Gamma$ decreases, $I_{SAT,TWPD}$ value increases, which provides improved power handing capability. In contrast to the increased $I_{SAT,TWPD}$, the 3dB bandwidth decreases as the f_{VM} is proportional to $\alpha\Gamma$. Therefore, there exists a trade-off between the bandwidth and the power capability in the TWPD.

The velocity mismatch can be eliminated by periodic capacitance loading effect. In fact, the electrical signal velocity in the CPW structure is around 35 % faster than the optical guided wave [21]. Therefore, distributing the PD in a periodic way, the electrical signal velocity can be slowed, and matches with the optical wave in the semiconductor. The electrical wave velocity is given in the periodic structure as,

$$\upsilon_e = \frac{1}{\sqrt{L_{tr} \cdot \left(C_{tr} + C_0 / l_d\right)}} \quad \textbf{(2.28)}$$

where, C_0 is the capacitance by each PD and l_d is the distance between PDs. These PDs are called *velocity-matched distributed* PDs (VMDPs). The detected electrical signal in each PD is collected in-phase, and high output current can be expected. Distinctive advantages in the VMDP are not only equivalent bandwidth to the transit time limited bandwidth (f_t) of a single PD, but also the separate design optimizations for the PD, the optical waveguide, and the electrical transmission line. The PD can be designed to have maximum allowable bandwidth, and the optical waveguide lines are independently optimized with respect to the single mode operation and the improved coupling efficiency. For the electrical transmission line, the micro strip line shall be used for the electrical signal summation, and be accounted for the characteristic impedance and the velocity matching. The saturation current for the VMDP is calculated as the summation of the each PD given by [21],

$$I_{SAT,VMDP} = q \int_{x=0}^{l_{diode}} W \frac{d}{\Gamma} P_0 \alpha\, \Gamma e^{-\alpha\, \Gamma x} dx \cdot \sum_{m=1}^{N} \kappa^{2(m-1)} \cdot e^{-\alpha\, \Gamma l_{diode}(m-1)} \quad \textbf{(2.29)}$$

where, κ is the coupling efficiency between the optical waveguide line and the individual PD, N is the number of employed diodes, l_{diode} is the length of each PD, and the quantum efficiency of the VMDP is,

$$\eta_{VMDP} = \frac{1-e^{-\alpha\,\Gamma l_{diode}}}{2}\frac{1-((1-\eta_0)\kappa^2)^N}{1-(1-\eta_0)\kappa^2}\,. \qquad \textbf{(2.30)}$$

The relationship between the saturation photocurrent and the 3dB electrical bandwidth is plotted in Fig. 2.5 for various kinds of PDs. The VMDP has the largest saturation photocurrent in magnitude among the other PDs, and shows $I_{SAT} \propto 1/f_{3dB}$ relation as the TWPD. It is due to the velocity-matched characteristic and the current in-phase addition along the optical waveguide. In contrast, the *p-i-n* type and the WGPD show a rapid decrease as the 3 dB bandwidth increases. This can be interpreted that the saturation current in the output is proportional to the effective area, which is square of PD dimensions [21]. For a simulation, the electrical wave velocity in the VMDP was assumed to be 99% of the optical wave in the waveguide. However, in the TWPD case, 80% of the optical velocity was used for the microwave velocity to demonstrate the velocity mismatch. We can see clearly how the velocity mismatch affects the saturation photocurrent in the VMDP and the TWPD in Fig. 2.5.

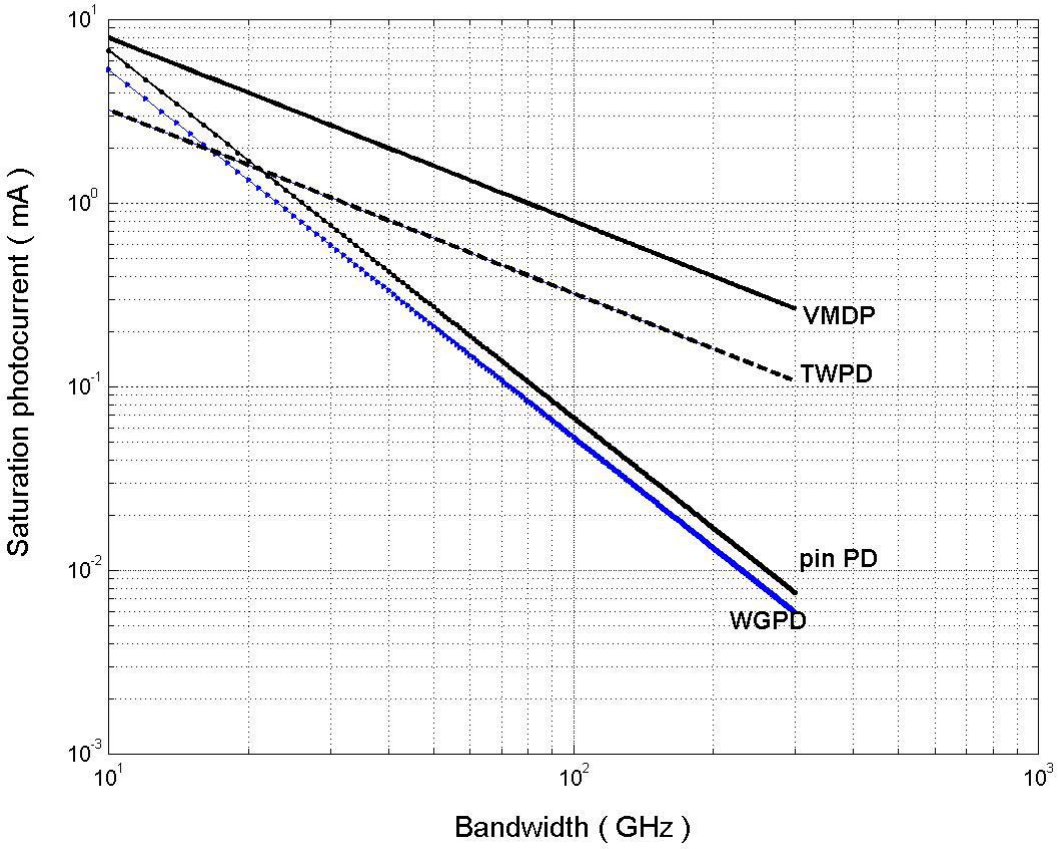

Fig. 2.5 Saturation photocurrent versus bandwidth simulation. Quantum efficiency for TWPD, VMDP, and WGPD is set to 0.4. I_s (saturation phtocurrent per unit area) is 0.025 mA/um^2 [21]. The electric wave velocity Ve=0.8*Vo for TWPD, and Ve=0.99*Vo for VMDP are used, where Vo represents the optical wave velocity in the waveguide. Width = 3um, Vo=8.615E9 cm/sec [21], period=150um, length of each PD in VMDP = 15um, R_L=50 Ω.

2.2. System model for an optically preamplified direct detection receiver system

2.2.1. Introduction

The system block diagram for an *optically preamplified direct detection* (OPDD) receiver is presented in Fig. 2.6. The light intensity is modulated in laser to transmit data stream. In long-haul transmission system, optical amplifiers such as the Raman and(or) the EDFA amplifier are utilized to increase optical signal power. In the OPDD system, the signal is amplified by the EDFA (C-band, L-band) before the optical signal arrives the PD. In most wavelength-division multiplexing (WDM) system, the optical band pass filter is located between the EDFA and the PD. It reduces the *amplified spontaneous emission* (ASE) noise generated in the EDFA. Regarding the ASE noise, it will be discussed in the following section. Then, the PD directly detects the optical signal and converts into an electrical signal. The detected electrical signal is large enough to drive the following demultiplexer circuit. Thus, the sampling circuit based demultiplexer circuit can be directly connected to the photodetector without further electrical amplification. In the conventional 2.5 Gbit/s and 10 Gbit/s optical receivers without optical amplifier, the electrical current after the PD is too low for direct digital processing in the demultiplexer and the decision circuit. Thus, so far a low noise preamplifier and a limiting amplifier circuit have been used. Furthermore, they increase the

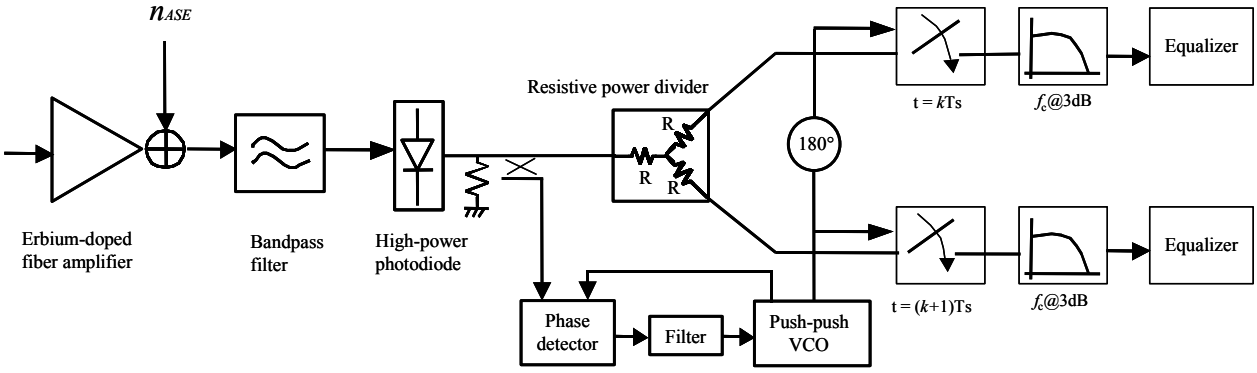

Fig. 2.6 System block diagram for an optically preamplified direct detection receiver with sampling circuit concept.

complexity of the optical receiver system and degrade the system performances (power consumption, bit error rate, etc.). However, in the OPDD receiver system, thanks to the optical preamplifier and the high-power PD, we expect high amplitude voltage (current) at the output of the PD. The signal shall be directly processed in the following demultiplexer circuit. We utilize this concept to construct the sampling circuit based optical receiver circuit and illustrate this configuration in Fig. 2.6.

From the EDFA to the photodetector, it is equivalent to the conventional OPDD receiver system. We describe here only the receiver side including the optical amplifier (EDFA) and the band pass filter. It is an effective way to analyze the receiver performance excluding the transmitter part. In this section, we describe the system model analytically for the OPDD receiver components (the EDFA, the optical band pass filter, and the PD). We provide the system characteristic functions and noise statistics when necessary. Using those analytic descriptions above, we further present the sampling circuit based demultiplexer circuit and the equalizer, in later sections.

2.2.1.1. System model of the EDFA

While the EDFA amplifies the optical signal, it also generates a noise component, the so-called an *amplified spontaneous emission* (ASE) noise. It is a significant noise quantity to be considered in a high sensitivity receiver. The EDFA can be represented equivalently with a frequency-dependent gain ($G(\upsilon)$), and the noise figure, F . The ASE noise after signal amplification in the EDFA is modeled as a *circularly symmetric additive white Gaussian noise process* [31]. The single-sided ASE noise power spectral density is written

$$S_{ASE}(\nu) = n_{sp}^{\ eff}(\nu)(G(\nu)-1)\cdot h\nu \qquad \textbf{(2.31)}$$

where, $n_{sp}^{\ eff}(\nu)$ is spontaneous emission factor, $G(\upsilon)$ is effective gain of the EDFA, h is the *Planck* constant ($6.626\cdot10^{-34}$ J·sec), and ν is the optical frequency. When the influence of the incoherent background light is included in the noise power, the amplifiers' equivalent noise figure, F_{equi}, is expressed as [31]

$$S_{ASE} + G(\nu) \cdot S_b = \frac{1}{2} \cdot h\nu \cdot G(\nu) \cdot F_{equi} \quad \textbf{(2.32)}$$

$$F_{equi} = F + 2(h\nu)^{-1} \cdot S_b = \frac{2n^{eff}{}_{sp}(\nu)(G(\nu)-1)}{G(\nu)} + 2 \cdot \left(\frac{\lambda}{hc}\right) \cdot S_b \quad \textbf{(2.33)}$$

where, F is the noise figure of the EDFA, and S_b is the power spectral density (PSD) of the incoherent background light.

It should be noted that relying on the signal level to be amplified in the EDFA, the dominant noise sources are different. For a logical zero level ('0'), a spontaneous-spontaneous beat noise dominates, whereas a signal-spontaneous beat noise is significant for a logical one level ('1'). Furthermore, the *probability density function* (PDF) for each dominating noise source has been verified theoretically as a non-Gaussian. However, the Gaussian approximation for those noise components shows very little difference, 0.3 dB [32]. Therefore, we will use the Gaussian pdf of the ASE noise without loss of generality.

2.2.1.2. Optical band pass filters

After the broadband amplification, an optical band pass filter follows the EDFA. In the WDM system, optical spectral filters can be classified relying on the physical phenomenon; *interference* and *diffraction*. A typical band pass filter which takes an advantage of the interference is the Fabry-Perot filter (FPF). It consists of two high-reflectance multi layers separated by $\lambda/2$. So, spectral characteristic peaks sharply at wavelength of multiples of $\lambda/2$. Its transfer function is written below under the assumption of *Lorentzian* distribution,

$$H_{FPF}(\nu) = \frac{\alpha}{\alpha + j2\pi\nu} = \frac{1}{1 + j2\nu/\mathrm{FWHM}} \quad \textbf{(2.34)}$$

where the FWHM ($=\alpha/\pi$) stands for *full width at half maximum* or at the 3dB frequency [31][33].

The other band pass filter used in WDM system is fiber Bragg grating (FBG) band pass filter. A Bragg grating is an one dimensional periodic array which has multiple semi-

reflectors (reflectance R) in its structure. Once the strong Bragg reflection condition is satisfied shown below, a specific wavelength channel is totally reflected back to the input port.

$$\lambda_B = 2\bar{n}\Lambda \qquad \textbf{(2.35)}$$

where $\bar{n}$ is the modal index, Λ is the grating period, and λ_B is the Bragg wavelength.

An example of the Bragg grating is illustrated in Fig. 2.7. The periodic structure can be made by exposing the structure (e.g. corrugated quaternary $In_xGa_{1-x}As_yP_{1-y}$ material on InP substrate) to the intense UV light [34]. This optical exposure technique uses a periodic interference pattern of the light. Applying this method to the fiber, equivalently altering the core refractive index of the fiber in a periodic way, the FBG filter can be implemented. This filter should combine with a circulator in order to convert band stop region into band pass filter characteristic. The optical transfer function is written as [14],

$$H_{FBG}(\omega) = \frac{j\kappa \sin\left(\sqrt{\delta^2 - \kappa^2}\cdot L_g\right)}{\sqrt{\delta^2 - \kappa^2}\cdot\cos\left(\sqrt{\delta^2 - \kappa^2}\cdot L_g\right) - j\delta\cdot\sin\left(\sqrt{\delta^2 - \kappa^2}\cdot L_g\right)} \qquad \textbf{(2.36)}$$

where, δ is the detuning from the Bragg wavelength ($= 2\pi/\lambda - 2\pi/\lambda_B$), κ is the coupling coefficient ($= \pi n_g \Gamma_{fiber}/\lambda_B$), and Γ_{fiber} is the confinement factor defined as

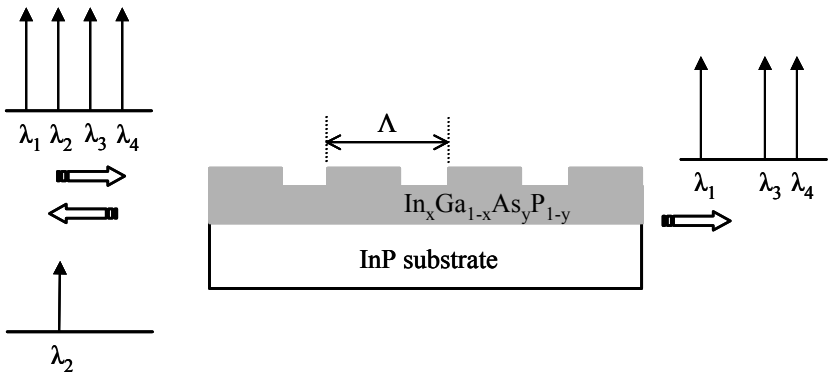

Fig. 2.7 An example of the Bragg grating. Quaternary $In_xGa_{1-x}As_yP_{1-y}$ material on InP substrate is corrugated. Optical band pass filtering is illustrated for various wavelengths.

$$\Gamma_{fiber} = \frac{P_{core}}{P_{total}} = \frac{\int_0^a |E_x|^2 \rho \cdot d\rho}{\int_0^\infty |E_x|^2 \rho \cdot d\rho} \qquad \textbf{(2.37)}$$

It is desirable to note that the bandwidth of the optical band pass filter impacts on the signal and the noise power related with the coding scheme; non return-to-zero (NRZ) and return-to-zero (RZ). It has been shown that (see e.g. [35]) for RZ signal the narrow bandwidth of the optical filter decrease the signal energy whereas it increases the intersymbol interference (ISI) for NRZ. There should be a tradeoff for the NRZ coding between the ISI and the ASE-ASE beat noise in choosing an optimum optical bandwidth of the filter. In contrast, for RZ, the ISI does not play a significant role in determining the optimum optical bandwidth, thus the ASE-ASE beat noise component should be considered to be minimum.

2.2.1.3. Photocurrent and noise

For the coherent electromagnetic field, the detection probability of photons is modeled by a *Poisson* probability distribution. In [37], the photocurrent is considered as a *stochastic* process when the photon falling at the PD is also a stochastic process. It has been shown that the photoelectrons also have the *Poisson* distribution. The photoelectron generation rate is expressed with the product of the photon arrival rate ($\lambda_{ph}(t)$) and the quantum efficiency of the photon detector (η). In this way, we can relate the photon statistics with the generated photoelectron,

$$\lambda(t) = \eta \cdot \lambda_{ph}(t) \qquad \textbf{(2.38)}$$

where $\lambda_{ph}(t)$ has the dimension of [number of photons/sec] and is defined as $P_{opt} / h\nu$. Here P_{opt} stands for the optical power. During incremental time interval Δt, the probability P to find out photoelectrons is [41]

$$P = \lambda(t) \cdot \Delta t \,. \qquad \textbf{(2.39)}$$

When photoelectrons are produced by the arrival of photons with the ratio given in (2.38), we can assume that the electric pulse $h(t)$ with the area of q (unit charge) is stimulated. If this event occurs at $t = k\Delta t$, the pulse is delayed by $k\Delta t$, $h(t - k\Delta t)$. Thus, electric current $i_{PD}(t)$ is given by a linear superposition of the electric pulse $h(t)$ with time interval Δt [38].

$$i_{PD}(t) = \left[\cdots + X(-\Delta t)\cdot h(t+\Delta t) + X(0)\cdot h(t) + X(\Delta t)\cdot h(t-\Delta t) + X(2\Delta t)\cdot h(t-2\Delta t) + \cdots\right]$$

$$= \sum_{k=-\infty}^{\infty} X(k\Delta t)\cdot h(t-k\Delta t) \qquad \textbf{(2.40)}$$

where $X(\cdot) \in \{0,1\}$ is a random variable which takes '1' with probability *P* and '0' with (1-*P*). Ensemble average and variance of the photocurrent, which determine the statistical characteristic of the detected photocurrent, are calculated in the following. Throughout the derivation processes, the $\langle \cdot \rangle$ symbol denotes an ensemble average.

First of all, the ensemble average of the photocurrent is expressed using the above equation as,

$$\langle i_{PD}(t)\rangle = \sum_{k=-\infty}^{\infty} \langle X(k\Delta t)\rangle \cdot h(t-k\Delta t) = \sum_{k=-\infty}^{\infty} P(k\Delta t)\cdot h(t-k\Delta t) \qquad \textbf{(2.41)}$$

Here we should note that equation (2.39) considers only *one realization* of the random process. However, when we treat with the ensemble average, the probability $P(k\Delta t)$ is expressed using the total probability theorem [36],

$$P(k) = \int_{-\infty}^{\infty} P(k|\boldsymbol{\lambda} = \lambda)p(\lambda)d\lambda \qquad \textbf{(2.42)}$$

where $p(\lambda)$ stands for the probability density function (pdf) of the random process $\lambda(t)$. By physical interpretation, $P(k|\boldsymbol{\lambda} = \lambda)$ equals to λ because the number of generated photoelectron during time interval Δt given the condition of photoelectron generation rate $\lambda(t)$ is $\lambda(t)\,\Delta t$. Therefore, the probability equals to

$$P(k|\boldsymbol{\lambda}=\lambda)=\frac{\lambda\cdot\Delta t}{\Delta t}=\lambda\,. \tag{2.43}$$

Inserting (2.43) into (2.42), we express the probability $P(k)$ as,

$$P(k)=\int_{-\infty}^{\infty}P(k|\boldsymbol{\lambda}=\lambda)p(\lambda)d\lambda=\int_{-\infty}^{\infty}\lambda\cdot p(\lambda)d\lambda=\langle\lambda\rangle\,. \tag{2.44}$$

Inserting (2.44) into (2.41) and taking a limit as $\Delta t\to 0$, we obtain the following relation,

$$\begin{aligned}\langle i_{PD}(t)\rangle&=\lim_{\Delta t\to 0}\sum_{k=-\infty}^{\infty}\langle\lambda(k\Delta t)\rangle\cdot h(t-k\Delta t)\\&=\int_{-\infty}^{\infty}\langle\lambda(\tau)\rangle\cdot h(t-\tau)d\tau\\&=\langle\lambda(t)\rangle * h(t)\end{aligned}\quad . \tag{2.45}$$

The * symbol represents a convolution defined below

$$(f*g)(t)=\int_{-\infty}^{\infty}f(\tau)\cdot g(t-\tau)d\tau \tag{2.46}$$

Using the following definition of the sensitivity of the photodetector,

$$\eta=\frac{h\nu}{q}\cdot R \tag{2.47}$$

where R is the responsivity of the photodetector and has the unit of [A/W], the photoelectron generation rate is written by,

$$\begin{aligned}\lambda(t)&=\eta\cdot\lambda_{ph}(t)\\&=\left(\frac{h\nu}{q}\cdot R\right)\cdot\left(\frac{P_{op}}{h\nu}\right)=\frac{R}{q}\cdot P_{opt}\end{aligned}\quad . \tag{2.48}$$

The optical field intensity after the optical band pass filter in the *optically preamplified direct detection* (OPDD) system is modeled as a normalized complex optical field as [47],

$$\mathbf{O_{RX}}(t) = O_{SIG}(t) + \mathbf{O_N}(t) \qquad \textbf{(2.49)}$$

where $O_{SIG}(t)$ means the complex envelope of the deterministic signal, and $\mathbf{O_N}(t)$ stands for the ASE noise of which characteristic is the *stationary, circularly symmetric, complex Gaussian process*. It is noted that we use the bold notation in order to indicate the random noise process. So, the optical power P_{opt} is given by

$$P_{opt} = \left|\mathbf{O_{RX}}(t)\right|^2 = \left|O_{SIG}(t)\right|^2 + \left|\mathbf{O_N}(t)\right|^2 + 2\cdot\Re\left\{O_{SIG}(t)\cdot\mathbf{O_N}^*(t)\right\} \qquad \textbf{(2.50)}$$

where $\Re(\ )$ denotes the real part of a complex number and $(\cdot)^*$ symbol represents a complex conjugate. Substituting equation (2.45) with (2.48) and (2.50),

$$\begin{aligned}\left\langle i_{PD}(t)\right\rangle &= \frac{R}{q}\left(\left\langle\left|\mathbf{O_{RX}}(t)\right|^2\right\rangle * h(t)\right) \qquad \textbf{(2.51)}\\ &= R\left\{\left\langle\left|O_{SIG}(t)\right|^2\right\rangle + \left\langle\left|\mathbf{O_N}(t)\right|^2\right\rangle + 2\cdot\Re\left\{O_{SIG}(t)\cdot\left\langle\mathbf{O_N}^*(t)\right\rangle\right\}\right\} * h_{PD}(t)\end{aligned}$$

where we replace $h(t)/q$ with $h_{PD}(t)$, thus the $h_{PD}(t)$ area is normalized as

$$\frac{1}{q}\int_{-\infty}^{\infty} h(t)dt = \int_{-\infty}^{\infty} h_{PD}(t)dt = 1. \qquad \textbf{(2.52)}$$

Using the fact that the stationary zero mean process of the noise $\mathbf{O_N}(t)$, $P_N = \left\langle\left|\mathbf{O_N}(t)\right|^2\right\rangle$, and $p_{SIG}(t) = \left\langle\left|O_{SIG}(t)\right|^2\right\rangle = \left|O_{SIG}(t)\right|^2$ we can simplify equation (2.51) as

$$\begin{aligned}\left\langle i_{PD}(t)\right\rangle &= R\cdot p_{SIG}(t) * h_{PD}(t) + R\cdot P_N * h_{PD}(t) \qquad \textbf{(2.53)}\\ &= R\cdot p_{SIG}(t) * h_{PD}(t) + R\cdot P_N\end{aligned}$$

Next, the autocovariance of $i_{PD}(t)$ is induced, and the detailed derivation process is presented in Appendix A and [39][40].

$$C_{\Delta i}(t,t') = \langle \Delta i(t) \cdot \Delta i(t') \rangle = \langle i(t) i(t') \rangle - \langle i(t) \rangle \langle i(t') \rangle \tag{2.54}$$

$$= R \cdot q\left(\left\langle \left| \mathbf{O_{RX}}(t) \right|^2 \right\rangle * {h_{PD}}^2(t) \right) + R^2 \int_{-\infty}^{\infty} \int_{-\infty}^{\infty} C_{\mathbf{O_{RX}}}(\tau,\tau') h_{PD}(t-\tau) h_{PD}(t-\tau') d\tau d\tau'$$

where $\Delta i(t) = i(t) - \langle i(t) \rangle$ and $C(\tau,\tau')$ is autocovariance of $\left| \mathbf{O_{RX}}(t) \right|^2$ written as,

$$C_{\mathbf{O_{RX}}}(\tau,\tau') = \left\langle \left| \mathbf{O_{RX}}(\tau) \right|^2 \cdot \left| \mathbf{O_{RX}}(\tau') \right|^2 \right\rangle - \left\langle \left| \mathbf{O_{RX}}(\tau) \right|^2 \right\rangle \left\langle \left| \mathbf{O_{RX}}(\tau') \right|^2 \right\rangle . \tag{2.55}$$

By equating $t = t'$ in (2.54) we can acquire four noise components. After mathematical manipulations using the equations (2.53) and (2.55), noise components can be found as [47],

$$\sigma_i^2(t) = \underbrace{\sigma_{i,signal\ shot}{}^2(t) + \sigma_{i,signal-ASE}{}^2(t)}_{\text{time dependent}} + \underbrace{\sigma_{i,ASE\ shot}{}^2(t) + +\sigma_{i,ASE-ASE}{}^2(t)}_{\text{stationary terms}} \tag{2.56}$$

where $\sigma_{i,signal\ shot}{}^2(t)$ is the signal shot noise, $\sigma_{i,ASE\ shot}{}^2(t)$ is the ASE shot noise, $\sigma_{i,signal-ASE}{}^2(t)$ is the signal-ASE beat noise, and $\sigma_{i,ASE-ASE}{}^2(t)$ is the ASE-ASE beat noise. Each expression is revisited from Appendix A.

$$\sigma_{i,signal\ shot}{}^2(t) = R \cdot q(p_{SIG}(t) * {h_{PD}}^2(t)) \tag{2.57}$$

$$\sigma_{i,ASE\ shot}{}^2(t) = R \cdot q(P_N * {h_{PD}}^2(t)) = 2qB\left(R \cdot P_N\right) \tag{2.58}$$

$$\sigma_{i,signal-ASE}{}^2(t) = 2R^2 \cdot \Re\left\{ \int_{-\infty}^{\infty} \int_{-\infty}^{\infty} O_{SIG}(\tau) O^*{}_{SIG}(\tau') \left\langle \mathbf{O_N}^*(\tau) \mathbf{O_N}(\tau') \right\rangle h_{PD}(t-\tau) h_{PD}(t-\tau') d\tau \cdot d\tau' \right\}$$

$$= 2R^2 P_N \cdot (p_{SIG}(t) * {h_{PD}}^2(t)) \tag{2.59}$$

$$\sigma_{i,ASE-ASE}{}^2(t) = R^2 \cdot \int_{-\infty}^{\infty}\int_{-\infty}^{\infty} \left| \left\langle \mathbf{O_N}^*(\tau)\mathbf{O_N}(\tau') \right\rangle \right|^2 h_{PD}(t-\tau)h_{PD}(t-\tau')d\tau \cdot d\tau' \quad \textbf{(2.60)}$$

In (2.58), the following definition for the bandwidth is used as [37][41],

$$B = \frac{1}{2}\int_{-\infty}^{\infty} h_{PD}{}^2(t)dt \,. \quad \textbf{(2.61)}$$

The noise autocorrelation function $\left\langle \mathbf{O_N}^*(\tau)\mathbf{O_N}(\tau') \right\rangle$ can be approximated using the *Dirac* δ-function as $P_N\delta(\tau-\tau')$. So, we can express $\sigma_{i,signal-ASE}{}^2(t)$ using the instantaneous signal power $p_{SIG}(t)$ and the ASE noise power P_N as shown in (2.59). Including the noise by the receiver electronic circuits, the whole receiver noise is completed as,

$$\sigma_i{}^2(t) = \sigma_{i,signal\,shot}{}^2(t) + \sigma_{i,ASE\,shot}{}^2(t) + \sigma_{i,signal-ASE}{}^2(t) + \sigma_{i,ASE-ASE}{}^2(t) + \sigma_{elec}{}^2(t) \quad \textbf{(2.62)}$$

where $\sigma_{elec}{}^2(t) = R \cdot NEP^2 \cdot B_h$ and the B_h is a receiver system bandwidth. The *NEP* means *noise-equivalent power* having a dimension of [W/Hz$^{1/2}$], and it is defined below.

$$NEP = \sqrt{\frac{4k_BT \cdot F_n}{R_L \cdot R^2}} \quad \textbf{(2.63)}$$

where k_B is the *Boltzmann constant* (1.38066×10^{-23} J/K), R_L is the load resistance, and F_n is an equivalent amplifier noise figure. We derive the photocurrent and the noise statistics. In the OPDD system, the noise components come from the signal amplitude dependent terms and the stationary terms. The source signal dependent noises are composed of the signal shot noise and the signal-ASE beat noise whereas the stationary noises are due to the ASE-ASE beat noise and the ASE shot noise. Finally we include the electronics noise to fulfil the all noise components. This result is summarized in (2.62).

2.3. Theory for the sampling circuit based demultiplexer circuit

2.3.1. Introduction

For the construction of the demultiplexing circuit, the operation principle of the sampling circuit based demultiplexer is analyzed and the simulation is carried out. The demultiplexer consists of a resistive power divider, two Si Schottky diode sampling circuits, and two low-pass filters (pulse shaping filters) and a high-speed signal processor. In order to reduce deterministic intersymbol interferences (ISI), a high-speed signal processor is connected after each low-pass filter. In the system model, a clock oscillator signal is assumed to be synchronous with the incoming input signal.

The amplified optical signal is incident on a waveguide-integrated high-power and high-speed photodiode, and the measured output voltage is 200 mV_{pp}. The electrical characteristics of the high-speed photodiode used in the experiment are found in [25], and summarized in Table. IV. The resistive power divider has a 6 dB insertion loss and divides the input signal into two ways. Then, the following Si Schottky diode sampling circuit samples the dividened signal. A sampling instant in each sampling circuit depends on the oscillator signal amplitudes. They are out-of-phase each other, so that the sampling action takes place sequentially. The high-speed electrical signal processor is attached to the low-pass filter following the sampling circuit. Two algorithms for the equalizer circuit are presented; the zero-forcing algorithm and the *Wiener-Kolmogorov* algorithm.

Table. IV Electrical characteristics of the high-speed photodiode used in the experiment [25]

Terms	Value
3 dB bandwidth	> 50 GHz
Pulse width (typ.)	9 ps
Wavelength range	1480~1620 nm
Polarization dependent loss (dB)	0.5 (typ)
Dark current	5 nA
Max. optical input power	13 dBm
S_{22} (0.05~50 GHz)	-13 dB

2.3.2. Theory description

For the purpose of the description about the sampling circuit based demultiplexer circuit, we will use a time-limited signal, $O_{RX}(t)$ and generalize the analytic pulse expression for both the NRZ and the RZ signal. We temporarily consider only optical signal field excluding the random noise component for circuit's functional explanation. Thus, we would use scalar notation for the signal after the optical band pass filter, i.e. $O_{RX}(t) = O_{SIG}(t)$. Let the optical field be defined within the time interval [0, (1+α)T_p],

$$O_{RX}(t) = \begin{cases} \dfrac{E_1}{T_p} & \text{for } \alpha \cdot T_p \le t \le T_p \\ \dfrac{E_1}{2 \cdot T_p} \cdot \left(1 - \sin \dfrac{\pi}{\alpha \cdot T_p} \left(\left| t - (1+\alpha)\dfrac{T_p}{2} \right| - \dfrac{T_p}{2} \right) \right) & \text{for } 0 \le t \le \alpha \cdot T_p \text{ or } T_p \le t \le (1+\alpha)T_p \\ 0 & \text{otherwise} \end{cases} \quad \textbf{(2.64)}$$

where, E_1 denotes the optical energy for a '1' bit, and T_p is the effective pulse duration shown below [31].

$$T_p = \frac{\int_{-\infty}^{\infty} O_{RX}(t)\,dt}{\max_t \left(O_{RX}(t) \right)} = \frac{E_1}{\max_t \left(O_{RX}(t) \right)} \quad \textbf{(2.65)}$$

Varying the pulse width with α and T_p, the NRZ and RZ pulse shape can be acquired. For example,

$$T_p = \begin{cases} T_{bit} & for\ NRZ\ signal \\ d \cdot T_{bit} & for\ RZ\ signal \end{cases} \quad \textbf{(2.66)}$$

where, T_{bit} is a bit duration, and d is the duty cycle, 33% [31]. Using the above equation, the optical pulse of 86 Gbit/s RZ optical signal is depicted in Fig. 2.8(a). Representing the frequency response of the photodiode and the electrical connector as a 5th order Bessel filter, its transfer function can be written as,

$$H(s) = \frac{K \cdot b_0}{B_n(s)}\bigg|_{5th} = \frac{945}{s^5 + 15s^4 + 105s^3 + 420s^2 + 945s + 945} \qquad \textbf{(2.67)}$$

where, K is the gain, and $B_n(s) = s^n + b_{n-1}s^{n-1} + \cdots + b_1 s + b_0$. For $k = 0,1,2,\ldots,n$, $b_k = \frac{(2n-k)!}{k!(n-k)!}\left(\frac{\omega_c}{2}\right)^{n-k}$ [49].

Using the ideal photodiode responsivity and normalizing the Bessel transfer function with respect to the load impedance, the electrical signal waveform can be obtained in Fig. 2.8(b). The simulated eye diagram shows a NRZ-like waveform due to the frequency response. Compared with the actual measured signal for the 86 Gbit/s RZ signal in Fig. 2.9, it emulates the real signal with a good agreement.

The sampling process can be regarded as the multiplication of the input signal waveform with the train of the impulse response of the sampling circuit in time domain. Let the sampling circuit impulse response be an ideal rectangular pulse with a pulse width τ, $rect(t/\tau)$.

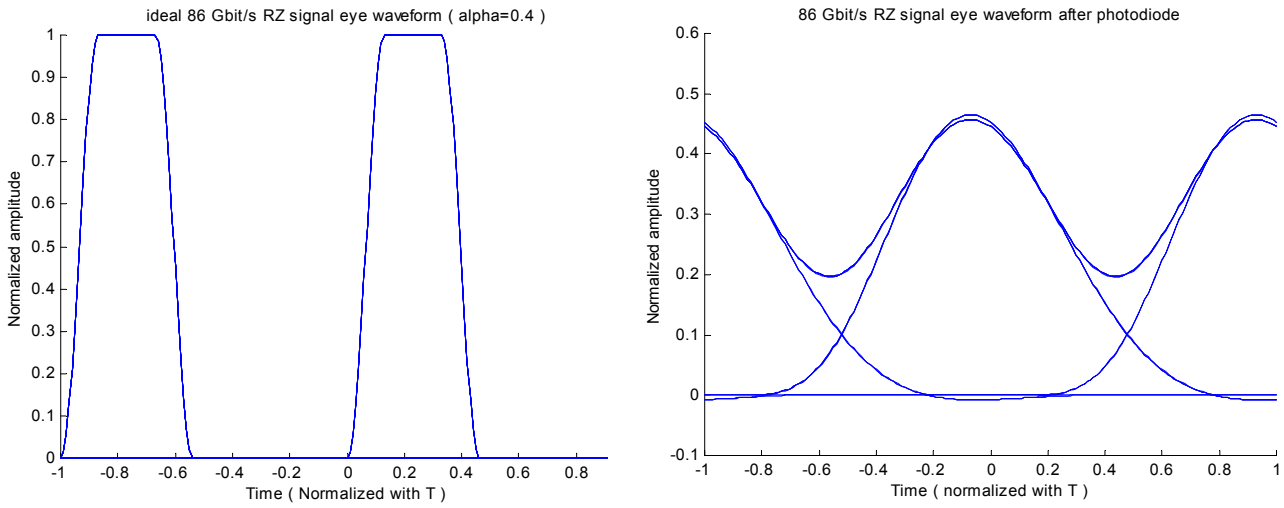

(a) (b)

Fig. 2.8 (a) 86 Gbit/s optical signal incident on photodiode, which has a bandwidth of 55 GHz. (b) 86 Gbit/s electrical signal waveform after the photodiode. Due to the bandwidth constraint of the photodiode(55 GHz) for 86 Gbit/s application, the resultant output shows NRZ-like signal having less signal harmonic components at the high frequency area.

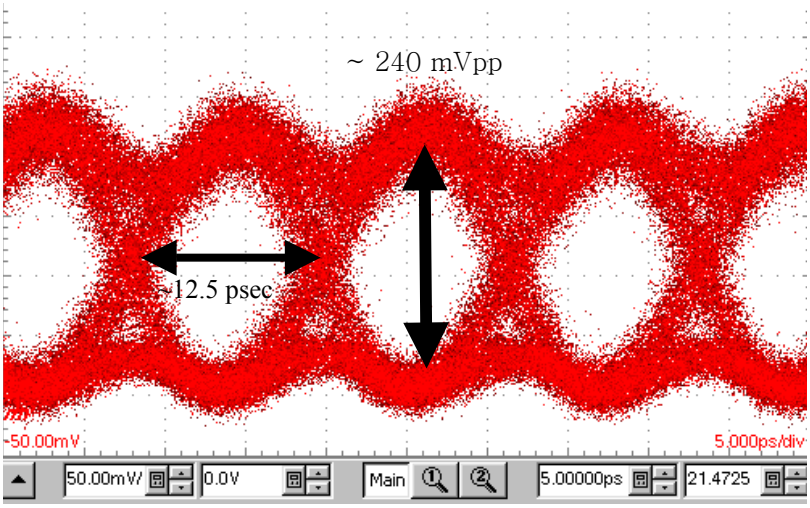

Fig. 2.9 Measured 86 Gbit/s RZ signal. It looks like a NRZ-like waveform.

The input signal to the demultiplexer can be expressed as

$$d(t,\cdot) = \sum_{n=0}^{\infty} r_n(\cdot) g(t - nT_{bit}) \qquad \textbf{(2.68)}$$

where, $r_n(\cdot)$ represents all possible ensembles of a random variable $\left\{\sqrt{\gamma_{ex}}, 1\right\}$ with a extinction ratio γ_{ex}. The extinction ratio is defined as

$$0 \le \gamma_{ex} = \frac{P_0}{P_1} \le 1 \qquad \textbf{(2.69)}$$

where P_0 is the power emitted during logical level '0', and P_1 is for the level '1'. Here, we use the normalized P_1 value. And, $g(t)$ can be expressed as a convolution of $O_{RX}(t)$ and $h(t)$ of the inverse *Laplace* transform of the 5th order Bessel filter.

Thus,

$$g(t) = Z_L \cdot R \cdot \left|O_{RX}(t)\right|^2 * h(t) = Z_L \cdot R \cdot \int_{\tau=-\infty}^{\infty} \left|O_{RX}(\tau)\right|^2 \cdot h(t-\tau) d\tau \qquad \textbf{(2.70)}$$

where $h(t) = L^{-1}\{H(s)\}$, R, and Z_L are the responsivity and a load impedance of the PD. Using a pulse shaping function, $g(t)$, a code length of $2^8 - 1$ PRBS data waveform is generated shown in Fig. 2.10(a) and depicts a logical value, '1', or '0' on each signal.

The sampling circuit output signals, channel 1 and channel 2, can be expresses as,

$$S_{sampler}(t)\big|_{Ch.1} = \tfrac{1}{2} \cdot h_{train}(t - 2nT) \cdot d(t, \cdot) = \tfrac{1}{2} \cdot \sum_{n=0}^{\infty} r_n(\cdot) \cdot g(t - nT) \cdot rect\left(\frac{t - 2nT}{T}\right)$$

$$S_{sampler}(t)\big|_{Ch.2} = \tfrac{1}{2} \cdot h_{train}(t - (2n+1)T) \cdot d(t, \cdot) = \tfrac{1}{2} \cdot \sum_{n=0}^{\infty} r_n(\cdot) \cdot g(t - nT) \cdot rect\left(\frac{t - (2n+1)T}{T}\right)$$

(2.71)

where, $h_{train}(t) = \sum_{n=0}^{\infty} h(t - nT) = \sum_{n=0}^{\infty} rect\left(\frac{t - nT}{T}\right)$ is the impulse train of the sampling circuit, illustrated in Fig. 2.10(b). Fig. 2.10(c) depicts its sampled signal waveform, and they are ideally similar to the rectangular pulses. Comparing with the input signal waveform in Fig. 2.10(a), the output waveform clearly explains that every second bits in the input data stream are detected. The sampled signal should be processed with the low-pass filter to make a demultiplexed waveform. It is simulated using the 5th order Bessel filter, which has a bandwidth of 20 GHz. Therefore, the demultiplexed output signal is written as a convolution of the $S_{sampler}(t)$ with a low-pass filter .

$$S_{DEM}(t)\big|_{Ch.1,2} = S_{sampler}(t)\big|_{Ch.1,2} * h_{LPF}(t) = \int S_{sampler}(\tau)\big|_{Ch.1,2} \cdot h_{LPF}(t - \tau) d\tau \qquad \textbf{(2.72)}$$

where $h_{LPF}(t)$ is the low-pass filter transfer function with 20 GHz bandwidth. Simulation result is presented in Fig. 2.11. It illustrates a demultiplexed pulse width (~20psec, 40 Gbit/s) and NRZ-like waveform. A *MATLAB* program is presented in Appendix B.

So far, we explain the sampling circuit based receiver circuit theory in detail using the ideal sampling circuit impulse response (rectangular function in time domain). We successfully acquire the demultiplexed digital eye waveform. It should be noted that the sampling in the sampling circuit does mean literally detecting the electrical signal periodically for demultiplexing purpose. It differs from the sampling in Nyquist theorem which defines the minimum sampling frequency to reconstruct the original signal without *aliasing effect*.

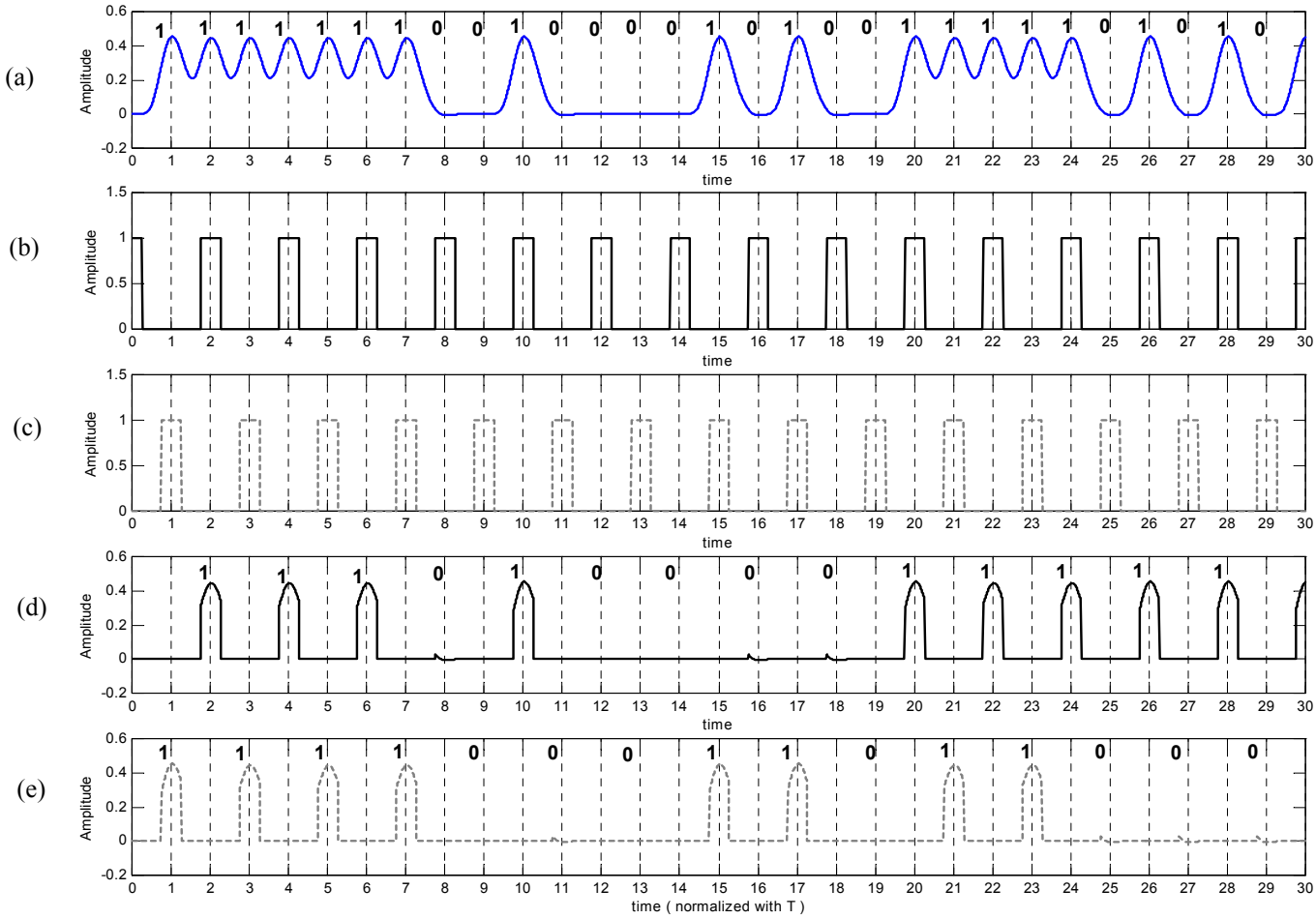

Fig. 2.10 (a) A code length of 2^8-1 data is presented in time domain. (b), (c) Impulse train of the sampling circuit for channel 1 and 2, respectively, which is synchronized with the input signal. The sampling process is regarded as the product of the input signal with the impulse train. (d), (e) The resultant output signals are shown indicating the corresponding data value, "1", and "0" for channel 1 and 2, respectively.

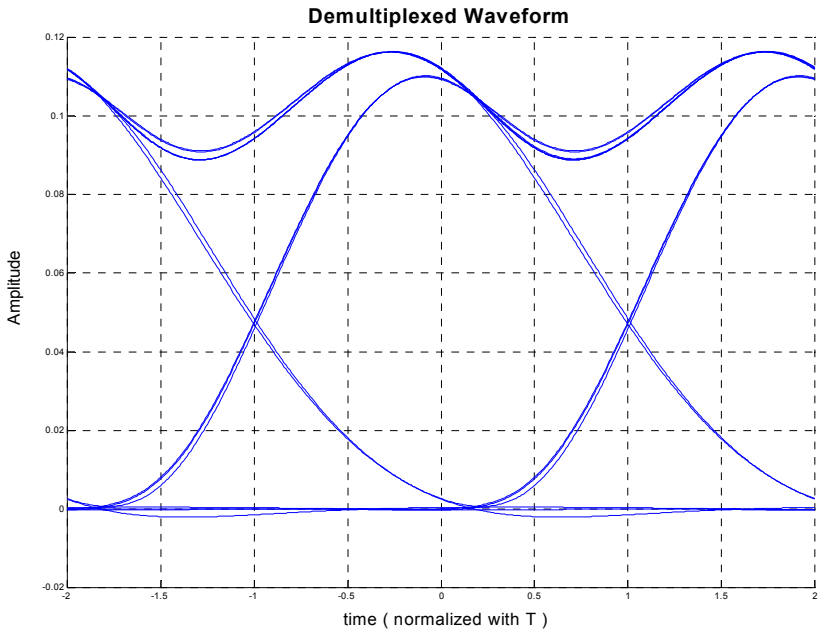

Fig. 2.11 A sampled waveform after the sampling circuit is passed through the low-pass filter. A demultiplexed eye diagram is simulated successfully.

2.4. Electrical equalizer circuit

2.4.1. Introduction

In the optical fiber transmission the optical signal experiences dispersions (CMD and PMD) and many impairments. As a result, the optical signal suffers from the ISI phenomena and corrupted by noise. As the bit rate-transmission distance product increases in the long-haul system transmission, the ISI mitigation is mandatory to enhance the bit-error-rate (BER). Transmission impairments can be largely classified into five ways, and summarized in Table. V [50]. So far, compensation techniques have been implemented in two ways: in the optical signal domain and in the electrical domain.

Optical signal compensation has an advantage over the electrical processing method in that it is independent of the signal bit rate because the bandwidth of the optical signal is much wider than that of the electrical signal. Furthermore, in case of the CMD, it is better than the electrical way because the CMD is linear phenomenon before electrical conversion. It is generally accepted that the optical mitigation outperforms the counterpart, i.e., the electrical way when the signal distortions are from the CMD, the PMD, fiber nonlinearities, and laser nonlinearities.

Many electrical signal processing methods are also developed and implemented in the transmission experiments. Electrical methods to reduce signal distortions include a *linear equalization*, *nonlinear cancellation* (*decision-feedback equalization*), *maximum likelihood sequence detection* (MLSD), coding and multi-level signaling. The ultimate performance of the electrical equalization can be acquired using the MLSD. It performs the *Viterbi* algorithm to detect the most probable information sequences after receiving distorted signal sequences. This method provides a criterion to evaluate other electrical methods. On the other hand, it increases the complexity of the receiver circuit. Therefore, the suboptimal equalization methods are nowadays employed: linear transversal filter or decision-feedback equalizer.

In general, the distortions are pattern-dependent, i.e. the distortion behavior is deterministic. Therefore, observing the signal distortion we can calculate the ISI directly. If optical transmission channels are time-varying, the adaptation algorithm could be utilized. For example, the PMD is a time-varying random phenomenon, so its characteristic is expressed using the root-mean-square (RMS) value. In this case, we effectively employ the adaptive

equalization method to keep track of the channel distortions. So far, the adaptive method is widely used in mobile phone and smart antenna system applications. Currently, adaptation methods are not implemented yet for 40 Gbit/s system applications in electrical domain. Chip complexity and speed hinder this method from being implemented in monolithic microwave IC (MMIC). But, it is expected that the adaptation technique would be widely used to enhance the system performance, and will appear in the market.

In this section, we will discuss linear equalization method. It is desirable to optimize the linear filter coefficient minimizing the BER in digital fiber optic systems. However, the BER is a nonlinear function of the filter coefficient. Thus, it is less effective to use the BER criterion [51].

Three methods are frequently used depending on the channel environment. A *zero-forcing* algorithm focuses on the removal of the ISI assuming the noise quantity could be negligible. On the other hand, a *matched filter* is for the minimization of the noise under the condition of the negligible ISI. Therefore, a careful observation should be carried out to choose a proper calculation algorithm. Minimizing the minimum square error between the real signal and the estimated signal vector, we obtain the well-known *Wiener-Kolmogorov* filter condition. In this section, we formalize the zero-forcing filter algorithm and the *Wiener-Kolmogorov* filter condition using the proposed system model for the sampling circuit employed OPDD receiver system in Fig. 2.12.

Table. V Equalization techniques in the long-haul direct detection receiver system after [50]

Impairment	Compensation technique
Chromatic dispersion	Dispersion compensated fiber Maximum likelihood detection Electrical transversal filter Nonlinear cancellation
Polarization dispersion	Adaptive polarization control Adaptive electrical transversal filter
Receiver electronics frequency response	Electrical transversal filter (Adaptive) Nonlinear cancellation (e.g. decision-feedback equalizer)
Laser nonlinearities	Laser bias adjustment Maximum likelihood detection
Fiber nonlinearities	Soliton Maximum likelihood detection

2.4.2. Model description

2.4.2.1. Zero-forcing algorithm

A system model of the sampling circuit based receiver circuit is presented in Fig. 2.12. If we express the incident optical power using the optical intensity as

$$\left\langle \left| \mathbf{O}_{\mathbf{RX}}(t) \right|^2 \right\rangle_e = p_{sig}(t) + P_N , \tag{2.73}$$

then a demultiplexer output is written below

$$\begin{aligned} S_{DEM}(t) &= (R \cdot p_{sig}(t) + R \cdot P_N) * h(t) \\ &= (s(t) + n(t)) * h(t) \end{aligned} \tag{2.74}$$

Here we assume that the photodiode, the sampling circuit, and the low-pass filter are *linear time-invariant* systems (LTI). Thus, the combined transfer function of three is given as

$$h(t) = h_{PD}(t) * h_{SAM}(t) * h_{LPF}(t) . \tag{2.75}$$

To express the output signal in discrete-time domain, we sample the output signal in time interval kT , and gather M samples. So, the demultiplexer output is written as,

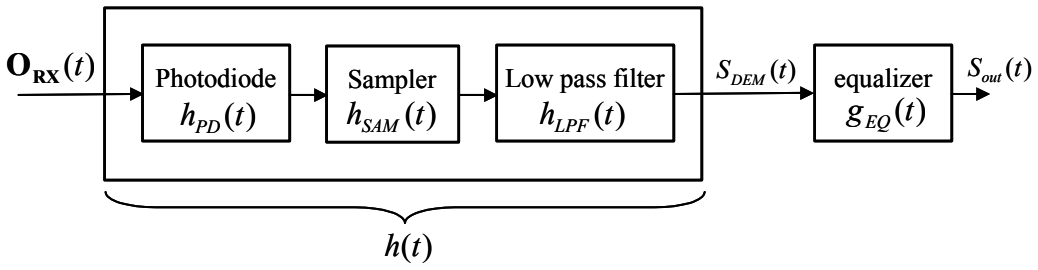

Fig. 2.12 A system model for the sampling circuit based OPDD receiver system

$$\begin{aligned}\underline{\mathbf{s_{DEM}}} &= \left[S_{DEM}(0),\, S_{DEM}(1),\ldots,\, S_{DEM}(M-1)\right]^{\mathrm{T}} \\ &= \left[S_{DEM,0},\, S_{DEM,1},\ldots,\, S_{DEM,M-1}\right]^{\mathrm{T}}\end{aligned} \tag{2.76}$$

And, we can also write the above equation using the transfer function ($h(t)$) in matrix form,

$$\begin{aligned}\underline{\mathbf{s_{DEM}}} &= \underline{\underline{\mathbf{H}}} \cdot \underline{\mathbf{s}} + \underline{\underline{\mathbf{H}}} \cdot \underline{\mathbf{n}} \\ &= \underline{\underline{\mathbf{H}}} \cdot \underline{\mathbf{s}} + \underline{\boldsymbol{\eta}}\end{aligned} \tag{2.77}$$

where, $\underline{\mathbf{s_{DEM}}} \in \mathbf{C}^{M\times 1}$, $\underline{\mathbf{s}} = [s_1\ s_2\ \cdots\ s_k \cdots s_N]^{\mathrm{T}}$, $\underline{\mathbf{n}} \in \mathbf{C}^{N\times 1}$, $\underline{\underline{\mathbf{H}}} \in \mathbf{C}^{M\times N}$, and we assume $E\{\underline{\mathbf{n}}\} = \underline{\mathbf{0}}$

After the equalizer, the output signal is given as

$$\begin{aligned}\underline{\mathbf{s_{out}}} &= \underline{\underline{\mathbf{G}}}^{\mathbf{H}} \cdot (\underline{\underline{\mathbf{H}}} \cdot \underline{\mathbf{s}} + \underline{\boldsymbol{\eta}}) \\ &= \underline{\underline{\mathbf{G}}}^{\mathbf{H}} \cdot \underline{\underline{\mathbf{H}}} \cdot \underline{\mathbf{s}} + \underline{\underline{\mathbf{G}}}^{\mathbf{H}} \cdot \underline{\boldsymbol{\eta}}\end{aligned}, \tag{2.78}$$

where $\underline{\underline{\mathbf{G}}}$ is the transfer function of the equalizer circuit, and $\underline{\underline{\mathbf{G}}} \in \mathbf{C}^{M\times N}$. The symbol $(\cdot)^H$ means the *Hermitian* matrix, a combined operation of transpose and complex conjugation. The *k*th element of $\underline{\mathbf{s_{out}}}$ is given by

$$\hat{s}_{out,k} = \underbrace{\underline{\mathbf{G_k}}^{\mathbf{H}} \cdot \underline{\mathbf{h_k}} \cdot s_k}_{\substack{\text{desired}\\ \text{signal}}} + \underbrace{\underline{\mathbf{G_k}}^{\mathbf{H}} \cdot \sum_{\substack{i=1\\ i\neq k}}^{N} \underline{\mathbf{h_i}} \cdot s_i}_{\text{ISI}} + \underbrace{\underline{\mathbf{G_k}}^{\mathbf{H}} \cdot \underline{\boldsymbol{\eta}}}_{\text{noise}} \tag{2.79}$$

where $\underline{\underline{\mathbf{G}}} = \left\{\underline{\mathbf{G_1}}, \underline{\mathbf{G_2}}, \ldots, \underline{\mathbf{G_k}}, \ldots \underline{\mathbf{G_N}}\right\}$, $\underline{\mathbf{G_k}} = \left[g_{-L,k}, g_{-L+1,k}, \ldots, g_{L,k}\right]^{\mathrm{T}}$, $\underline{\underline{\mathbf{H}}} = \left\{\underline{\mathbf{h_1}}, \underline{\mathbf{h_2}}, \ldots, \underline{\mathbf{h_k}}, \ldots, \underline{\mathbf{h_N}}\right\}$, $\underline{\mathbf{h_k}} = \left[h_{0,k}, h_{1,k}, \ldots, h_{M-1,k}\right]^{\mathrm{T}}$, and $M = 2L+1$.

The zero-forcing filter is defined as an equalizer to eliminate the ISI component. It is also called as the *peak distortion criterion*, because it minimize the peak distortion defined by the ISI. Assuming the infinite number of filter coefficients, the *k*th output signal is acquired as

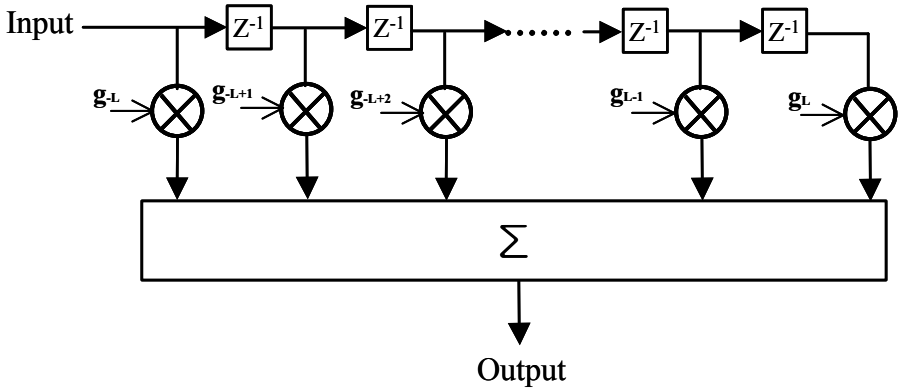

Fig. 2.13 Linear equalizer. Coefficients are calculated using the Zero-forcing algorithm.

$$\hat{s}_{out,k} = s_k + \underline{\mathbf{G}_k}^{\mathrm{H}} \cdot \underline{\boldsymbol{\eta}} \qquad \textbf{(2.80)}$$

Therefore, if the following condition is satisfied

$$\underline{\underline{\mathbf{G}}}^{\mathrm{H}} \cdot \underline{\underline{\mathbf{H}}} = \underline{\underline{\mathbf{I}}}_{\mathrm{N}} \qquad \textbf{(2.81)}$$

where, $\underline{\underline{\mathbf{I}}}_{\mathrm{N}} = \begin{bmatrix} 1 & & \mathbf{0} \\ & 1 & \\ & \ddots & \\ \mathbf{0} & & 1 \end{bmatrix}$,

we can obtain the ISI-free signal after the equalizer. Fig. 2.13 illustrates a filter based on the *zero-forcing* algorithm with order of (2N+1). It consists of periodic delay lines and coefficient multipliers. At this moment filter coefficients are fixed to a certain value, however if we apply the adaptive signal processing technique to the filter, coefficients are adaptively changed.

The zero-forcing filter coefficients are decided by the following argument.

$$\arg\min_{\underline{\underline{\mathbf{G}}}} tr(\underline{\underline{\mathbf{G}}}^{\mathrm{H}} \cdot \underline{\underline{\mathbf{R}}}_{\boldsymbol{\eta}} \cdot \underline{\underline{\mathbf{G}}}) \text{ subject to } \underline{\underline{\mathbf{G}}}^{\mathrm{H}} \cdot \underline{\underline{\mathbf{H}}} = \underline{\underline{\mathbf{I}}}_{\mathrm{N}} \qquad \textbf{(2.82)}$$

where, $\underline{\underline{\mathbf{R}}}_{\boldsymbol{\eta}} = \mathrm{E}\left\{ \underline{\underline{\mathbf{H}}} \cdot \underline{\mathbf{n}}\underline{\mathbf{n}}^{\mathrm{H}} \cdot \underline{\underline{\mathbf{H}}}^{\mathrm{H}} \right\} = \underline{\underline{\mathbf{H}}} \cdot \underline{\underline{\mathbf{R}}}_{\mathbf{n}} \cdot \underline{\underline{\mathbf{H}}}^{\mathrm{H}}$, and $\underline{\underline{\mathbf{R}}}_{\mathbf{n}} = \mathrm{E}\left\{ \underline{\mathbf{n}}\underline{\mathbf{n}}^{\mathrm{H}} \right\}$ is a noise correlation vector.

The $tr(\cdot)$ symbol represents a *trace* of a matrix.

Minimizing the noise power, $tr(\underline{\underline{\mathbf{G}}}^{\mathrm{H}} \cdot \underline{\underline{\mathbf{R}}}_{\boldsymbol{\eta}} \cdot \underline{\underline{\mathbf{G}}})$ at the output of the equalizer circuit, we calculate filter coefficients. This is a constrained minimization problem, which can be solved using the *Lagrange multipliers* method. The *Lagrangian* equation is

$$\mathscr{L}(\underline{\underline{\mathbf{G}}}, \underline{\underline{\boldsymbol{\lambda}}}) = tr(\underline{\underline{\mathbf{G}}}^{\mathrm{H}} \cdot \underline{\underline{\mathbf{R}}}_{\boldsymbol{\eta}} \cdot \underline{\underline{\mathbf{G}}}) + \underline{\underline{\boldsymbol{\lambda}}}^{\mathrm{H}} \cdot (\underline{\underline{\mathbf{H}}}^{\mathrm{H}} \cdot \underline{\underline{\mathbf{G}}} - \underline{\underline{\mathbf{I}}}_{\mathrm{N}}) + (\underline{\underline{\mathbf{G}}}^{\mathrm{H}} \cdot \underline{\underline{\mathbf{H}}} - \underline{\underline{\mathbf{I}}}_{\mathrm{N}}) \cdot \underline{\underline{\boldsymbol{\lambda}}}, \quad \textbf{(2.83)}$$

where $\underline{\underline{\boldsymbol{\lambda}}}$ is a *Lagrange multiplier* in vector form.

Finding out the conditions for $\frac{d\mathscr{L}(\underline{\underline{\mathbf{G}}}, \underline{\underline{\boldsymbol{\lambda}}})}{d\underline{\underline{\mathbf{G}}}^{*}} = 0$ and $\frac{d\mathscr{L}(\underline{\underline{\mathbf{G}}}, \underline{\underline{\boldsymbol{\lambda}}})}{d\underline{\underline{\boldsymbol{\lambda}}}^{*}} = 0$, the following result can be derived,

$$\underline{\underline{\mathbf{G}}}_{\mathrm{ZF}} = \underline{\underline{\mathbf{R}}}_{\boldsymbol{\eta}}^{-1} \cdot \underline{\underline{\mathbf{H}}} \cdot (\underline{\underline{\mathbf{H}}}^{\mathrm{H}} \underline{\underline{\mathbf{R}}}_{\boldsymbol{\eta}}^{-1} \underline{\underline{\mathbf{H}}})^{-1}. \quad \textbf{(2.84)}$$

If $\underline{\underline{\mathbf{R}}}_{\boldsymbol{\eta}} = \sigma_n^{\,2} \underline{\underline{\mathbf{I}}}_{\mathrm{N}}$, the zero-forcing filter coefficient vector is found as $\underline{\underline{\mathbf{G}}}_{\mathrm{ZF}} = (\underline{\underline{\mathbf{H}}}^{\mathrm{H}})^{+}$. Here, the $(\cdot)^{+}$ symbol represents the *pseudo-inverse* matrix.

Using the above result, we can calculate the SNR at the output of the filter. We will derive the expressions for the signal power and the noise power, respectively. First of all, the signal power after the equalization

$$\mathrm{P}_{\mathrm{s,EQ}} = \mathrm{E}\left\{ \|\underline{\mathbf{s}}\|_2^{\,2} \right\} = tr\,\mathrm{E}\left\{ \underline{\mathbf{s}}\underline{\mathbf{s}}^{\mathrm{H}} \right\} = N. \quad \textbf{(2.85)}$$

Here we normalize the signal power and assume the infinite number of filter coefficients.

And, the noise power is given

$$\begin{aligned} \mathrm{P}_{\mathrm{N,EQ}} &= tr\left(\underline{\underline{\mathbf{G}}}^{\mathrm{H}} \cdot \underline{\underline{\mathbf{R}}}_{\boldsymbol{\eta}} \cdot \underline{\underline{\mathbf{G}}} \right) = tr\left\{ \left(\underline{\underline{\mathbf{H}}}^{\mathrm{H}} \cdot \underline{\underline{\mathbf{H}}} \right)^{-1} \underline{\underline{\mathbf{H}}}^{\mathrm{H}} \cdot \underline{\underline{\mathbf{H}}} \cdot \left(\underline{\underline{\mathbf{H}}}^{\mathrm{H}} \cdot \underline{\underline{\mathbf{H}}} \right)^{-1} \right\} \\ &= tr\left\{ \left(\underline{\underline{\mathbf{H}}}^{\mathrm{H}} \cdot \underline{\underline{\mathbf{H}}} \right)^{-1} \right\} \end{aligned} \quad \textbf{(2.86)}$$

Let us decompose $\left(\underline{\underline{\mathbf{H}}}^{\mathrm{H}} \cdot \underline{\underline{\mathbf{H}}} \right)^{-1}$ using the singular value decomposition (SVD). It is shown that if $\underline{\underline{\mathbf{H}}}^{\mathrm{H}} \cdot \underline{\underline{\mathbf{H}}} = \underline{\underline{\mathbf{U}}} \cdot \underline{\underline{\boldsymbol{\Lambda}}} \cdot \underline{\underline{\mathbf{U}}}^{\mathbf{H}}$ where $\underline{\underline{\boldsymbol{\Lambda}}}$ is given by,

$$\underline{\underline{\mathbf{\Lambda}}} = \begin{bmatrix} \lambda_1 & & \mathbf{0} \\ & \lambda_2 & \\ & & \ddots \\ \mathbf{0} & & \lambda_N \end{bmatrix} \quad \textbf{(2.87)}$$

with *eigenvalues* of the matrix $(\lambda_1, \lambda_2, \ldots, \lambda_N)$, then

$$\left(\underline{\underline{\mathbf{H}}}^{\mathrm{H}} \cdot \underline{\underline{\mathbf{H}}}\right)^{-1} = \underline{\underline{\mathbf{U}}} \cdot \underline{\underline{\mathbf{\Lambda}}}^{-1} \cdot \underline{\underline{\mathbf{U}}}^{\mathbf{H}}. \quad \textbf{(2.88)}$$

Thus, the noise power is calculated as

$$\mathrm{P}_{\mathrm{N,EQ}} = \sum_{k=1}^{N} \frac{1}{\lambda_k}. \quad \textbf{(2.89)}$$

We therefore obtain the SNR as

$$\mathrm{SNR} = \frac{P_{s,EQ}}{P_{N,EQ}} = \frac{N}{\sum_{k=1}^{N} \frac{1}{\lambda_k}}. \quad \textbf{(2.90)}$$

If $\lambda_1 = \lambda_2 = \cdots = \lambda_N = \lambda_C$, then the SNR simply equals to λ_c.

2.4.2.2. Wiener-Kolmogorov filter

A *Wiener-Kolmogorov* filter is called as a minimum mean square error (MMSE) filter. It measures the distance between the real signal vector and the estimated signal vector, and then minimizes the distance with regard to the filter coefficients. Here, we describe the MMSE filter argument as

$$\underline{\underline{\mathbf{G}}}_{\mathrm{WF}} = \arg\min_{\underline{\underline{\mathbf{G}}}} \mathrm{E}\left\{ \left\| \underline{\mathbf{s}_{\mathbf{out}}} - \underline{\mathbf{s}} \right\|_2^{\,2} \right\}. \quad \textbf{(2.91)}$$

The solution for the above argument can be obtained when the first differentiation

$$d\mathrm{E}\left\{\left\|\underline{\mathbf{s}}_{\mathbf{out}}-\underline{\mathbf{s}}\right\|_2^{\,2}\right\}\Big/ d\underline{\underline{\mathbf{G}}}^{*}=\underline{\underline{\mathbf{0}}}. \tag{2.92}$$

A function for the vector norm is given by

$$\begin{aligned}\mathrm{K}(\underline{\underline{\mathbf{G}}}) &= tr\,\mathrm{E}\left\{\left(\underline{\mathbf{s}}_{\mathbf{out}}-\underline{\mathbf{s}}\right)\cdot\left(\underline{\mathbf{s}}_{\mathbf{out}}-\underline{\mathbf{s}}\right)^{\mathrm{H}}\right\}\\ &= tr\,\mathrm{E}\left\{\underline{\mathbf{s}}_{\mathbf{out}}\cdot\underline{\mathbf{s}}_{\mathbf{out}}{}^{\mathrm{H}}\right\}-tr\,\mathrm{E}\left\{\underline{\mathbf{s}}_{\mathbf{out}}\cdot\underline{\mathbf{s}}^{\mathrm{H}}\right\}-tr\,\mathrm{E}\left\{\underline{\mathbf{s}}\cdot\underline{\mathbf{s}}_{\mathbf{out}}{}^{\mathrm{H}}\right\}-tr\,\mathrm{E}\left\{\underline{\mathbf{s}}\cdot\underline{\mathbf{s}}^{\mathrm{H}}\right\}\end{aligned} \tag{2.93}$$

If we assume that the signal and the noise is uncorrelated each other, and using facts below,

$$\begin{aligned}\underline{\mathbf{s}}_{\mathbf{out}} &= \underline{\underline{\mathbf{G}}}^{\mathrm{H}}\cdot\underline{\underline{\mathbf{H}}}\cdot\underline{\mathbf{s}}+\underline{\underline{\mathbf{G}}}^{\mathrm{H}}\cdot\underline{\boldsymbol{\eta}}\\ tr\,\mathrm{E}\left\{\underline{\mathbf{s}}\underline{\mathbf{s}}^{\mathrm{H}}\right\} &= tr\,\underline{\underline{\mathbf{I}}}_{\mathrm{N}}=N\end{aligned} \tag{2.94}$$

we express the vector norm function as

$$\mathrm{K}(\underline{\underline{\mathbf{G}}})=tr\left\{\underline{\underline{\mathbf{G}}}^{\mathrm{H}}\left(\underline{\underline{\mathbf{H}}}\,\underline{\underline{\mathbf{H}}}^{\mathrm{H}}+\underline{\underline{\mathbf{R}}}_{\boldsymbol{\eta}}\right)\underline{\underline{\mathbf{G}}}\right\}-tr\left(\underline{\underline{\mathbf{G}}}^{\mathrm{H}}\cdot\underline{\underline{\mathbf{H}}}\right)-tr\left(\underline{\underline{\mathbf{H}}}^{\mathrm{H}}\cdot\underline{\underline{\mathbf{G}}}\right)+N \tag{2.95}$$

Solving $d\mathrm{K}(\underline{\underline{\mathbf{G}}})\big/ d\underline{\underline{\mathbf{G}}}^{*}=\underline{\underline{\mathbf{0}}}$, the MMSE filter condition is calculated as shown below,

$$\underline{\underline{\mathbf{G}}}_{\mathrm{WF}}=\left(\underline{\underline{\mathbf{H}}}\,\underline{\underline{\mathbf{H}}}^{\mathrm{H}}\right)^{-1}\cdot\left(\underline{\underline{\mathbf{H}}}+\underline{\underline{\mathbf{R}}}_{\boldsymbol{\eta}}\right). \tag{2.96}$$

To compare this solution with the zero-forcing algorithm solution, let us use the matrix identity below.

$$\left(\underline{\underline{\mathbf{A}}}\,\underline{\underline{\mathbf{B}}}\,\underline{\underline{\mathbf{A}}}^{\mathrm{H}}+\underline{\underline{\mathbf{C}}}\right)^{-1}\underline{\underline{\mathbf{A}}}\,\underline{\underline{\mathbf{B}}}\equiv\underline{\underline{\mathbf{C}}}^{-1}\,\underline{\underline{\mathbf{A}}}\left(\underline{\underline{\mathbf{A}}}^{\mathrm{H}}\,\underline{\underline{\mathbf{C}}}^{-1}\,\underline{\underline{\mathbf{A}}}+\underline{\underline{\mathbf{B}}}^{-1}\right)^{-1} \tag{2.97}$$

Setting $\underline{\underline{\mathbf{A}}}=\underline{\underline{\mathbf{H}}}$, $\underline{\underline{\mathbf{B}}}=\underline{\underline{\mathbf{I}}}_{\mathrm{N}}$, and $\underline{\underline{\mathbf{C}}}=\underline{\underline{\mathbf{R}}}_{\boldsymbol{\eta}}$, and inserting to the above equation, the final result is

straightforward.

$$\underline{\underline{\mathbf{G}}}_{\mathrm{WF}} = \underline{\underline{\mathbf{R}}}_{\boldsymbol{\eta}}^{-1}\underline{\underline{\mathbf{H}}}\left(\underline{\underline{\mathbf{H}}}^{\mathrm{H}}\underline{\underline{\mathbf{R}}}_{\boldsymbol{\eta}}^{-1}\underline{\underline{\mathbf{H}}} + \underline{\underline{\mathbf{I}}}_{\mathrm{N}}\right)^{-1} \qquad \textbf{(2.98)}$$

In general, when the transmit power increases, the MMSE filter solution approaches to the zero-forcing solution while the decreased signal power causes the MMSE filter coefficients converging to the matched filter coefficients.

For the sampling circuit based demultiplexer circuit, two algorithm for the equalizer circuit are presented. Using a finite number of taps the equalizer circuit for the demultiplexer circuit will be proposed and simulated. That is discussed in section 3.4.2.

Chapter 3 Circuit Design and Simulation

3.1. Si Schottky diode modeling

Schottky diodes are majority carrier devices, and as a consequence a storage time due to minority carriers is quite small, i.e., resulting in little diffusion capacitance. A junction capacitance dominates in forward bias condition. Hence, the diode shows ultra-fast switching speed compared to other junction diodes. This is an attractive advantage for millimeter-wave circuit design. Very high-speed Schottky diodes having cutoff frequencies in THz regime are reported in [9] and [10] using Si and III-V compound semiconductor materials.

Concerning the Schottky diode model, a *large-signal nonquasi-static* model should be considered in high frequency regime. *Nonquasi-static* device modeling is desirable when the operating frequency approaches the upper limit of validity for quasi-static models.

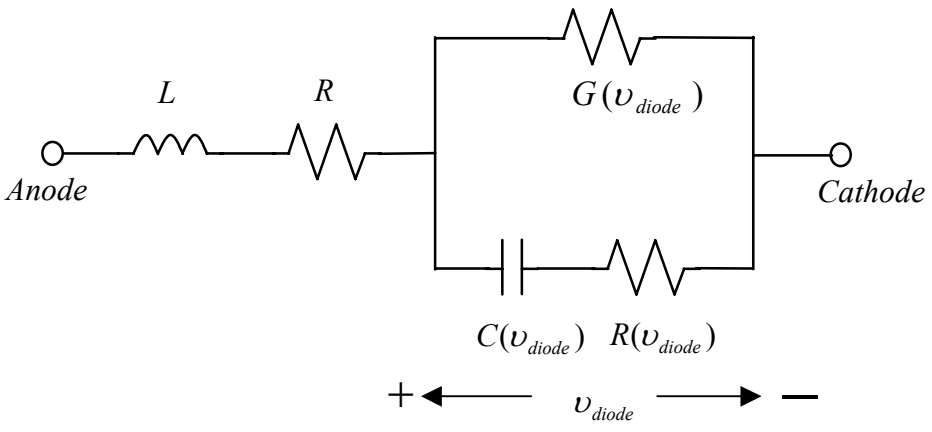

Fig. 3.1 Equivalent circuit of a diode. It is composed of extrinsic components (L, R) and the intrinsic components $C(\upsilon_{diode})$, $R(\upsilon_{diode})$, and $G(\upsilon_{diode})$, which are bias-dependent and specified independently.

Fig. 3.1 depicts the equivalent circuit model for a Si Schottky diode. Each parameter value is linearized depending on the bias voltage, and independent of each other. The model is composed of two series parasitic components (inductance and resistance) and the intrinsic three parts; intrinsic capacitance ($C(\upsilon_{diode})$), bias-dependent resistance ($R(\upsilon_{diode})$), and bias-dependent current source ($G(\upsilon_{diode})$). In order to construct a large-signal diode model in this work, three constitutive relations shown below are employed so as to express the instantaneous current at each node under large-signal conditions. They are *bias-dependent* and have a *charge-conservative* relation.

$$Q(\upsilon) = \int C(\upsilon) d\upsilon \qquad \textbf{(3.1)}$$

$$I_{DC}(\upsilon) = G_{DC}(\upsilon) \cdot \upsilon \qquad \textbf{(3.2)}$$

$$\tau(\upsilon) = C(\upsilon) \cdot R(\upsilon) \qquad \textbf{(3.3)}$$

Strictly speaking, as discussed below, a charge-relaxation-time equation is associated for the purpose of describing *instantaneous* node currents using the above equations. In this work, for the Si Schottky diode modeling, the Root-diode model is chosen. This diode model is fundamentally a *nonquasi-static* and a *charge-conservative* model [26], and widely used for three-terminal devices (HEMT, FET) modeling. The Root-diode model was originally proposed by David Root in [28]. Due to its superior characteristics, i.e., fabrication-independent modeling, less time consumption compared to other device models, and very precise device description regardless of its operating frequency, this model is frequently preferred in very high-speed device modeling.

When a terminal voltage changes slowly, terminal charges can catch up with its steady-state charge value, $Q_s^{ss}(v_{diode}(t))$. But, for higher operating frequency regime, the terminal charge shows a delay, not responding to the voltage change simultaneously. This nonquasi-static phenomenon can be described using a first-order differential equation, or a charge-relaxation-time approach method. In general, the total current at each node is the summation of conduction current and displacement current [27] written by

$$I_{total}(t) = I_{cond}(t) + I_{disp}(t) \quad (3.4)$$

where $I_{cond}(t) = I_o(v_{diode}(t))$, $I_{disp}(t) = dQ(t)/dt$, and $Q(t)$ is the node charge.

Using a charge-relaxation-time approach, $I_{disp}(t)$ can be expressed using the following equation.

$$I_{disp}(t) = \frac{dQ(t)}{dt} = -\frac{Q(t) - Q_s^{ss}(v_{diode}(t))}{\tau(C(v_{diode}(t), R(v_{diode}(t)))} \quad (3.5)$$

Note that the applied bias to the diode neglects voltage drops at the parasitic resistance for simplicity. Equation (3.5) describes the large-signal behavior of the displacement current, and also enables to determine the nonquasi-static characteristic of the diode. This Root-diode model can be used for transient analysis in time domain, harmonic balance simulation in frequency domain, and small-signal analysis in frequency domain [28].

3.1.1. The Root-diode model generation

Using *Agilent*'s parameter extraction software, IC-CAP, the intrinsic Si Schottky diode elements are modeled, excluding parasitic resistances and de-embedding open and short patterns. The parasitic resistance comes from the RF probes and cable losses. Fig. 3.2 displays the procedure how to generate the Root-diode model using the IC-CAP program.

First of all, it measures RF port series resistances using short pattern on an impedance standard substrate (ISS). For a two-port configuration, it will measure series resistances at each port varying the current. Extracted resistance values are removed from the measurement data. Also, the procedure includes the extraction of the parasitic series resistance and inductance, which are shown in Fig. 3.1. In addition, open pad parasitics are de-embedded from the measurement data, hence the intrinsic Root-diode model can be acquired. After iterating the comparison with the measurement data until discrepancy satisfies the user-defined criterion, the program produces the Root-diode model.

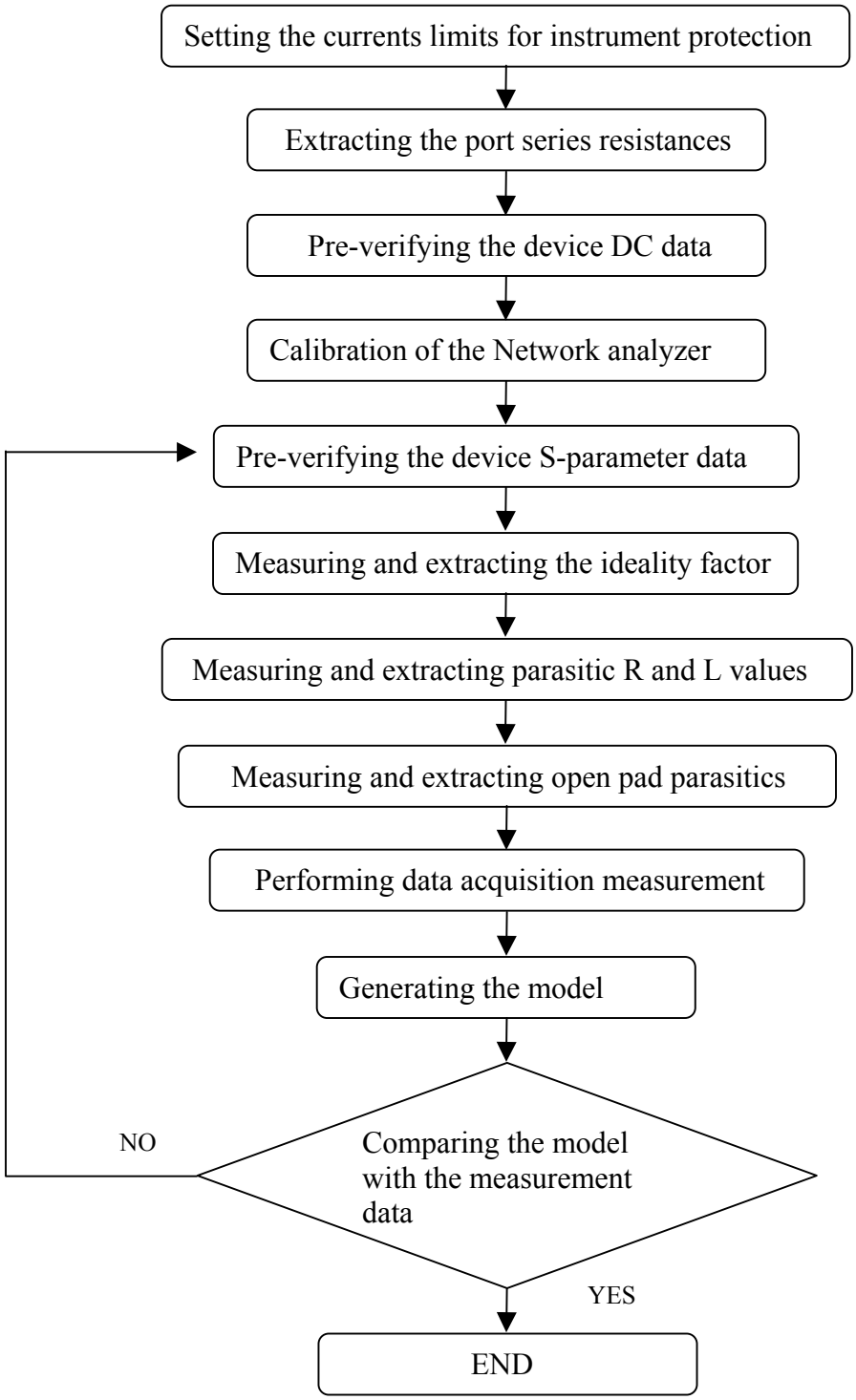

Fig. 3.2 Procedures to generate the Root-diode model using Agilent IC-CAP program

When measuring the diode ideality factor, the following equation is used for its calculation, and measured for various bias condition.

$$n = \frac{\log e}{V_T} \cdot \frac{\upsilon_2 - \upsilon_1}{\log i_2 - \log i_1} \qquad \textbf{(3.6)}$$

where, V_T is the thermal voltage, kT/q (25.8 mV), υ_2, υ_1 are closely adjacent measurement voltages, and i_2, i_1 are corresponding currents, respectively.

The measurement result is depicted in Fig. 3.3. The ideality factor calculation using the above equation is only valid in the range of $\upsilon_{diode} > 0$ and its relevant current region is where recombination current is not dominant (typically > 0.2 V) [60]. As shown in Fig. 3.3, the ideality factor starts to increase from υ_{diode} = 0 V to υ_{diode} = 0.35 V, and then it decreases until υ_{diode} = 0.46 V. Above this voltage high-current effects, such as high level injection and ohmic effects occur. Averaging the calculated ideality factor for $\upsilon_{diode} < 0.4$ V, we obtain the diode ideality factor of 1.51.

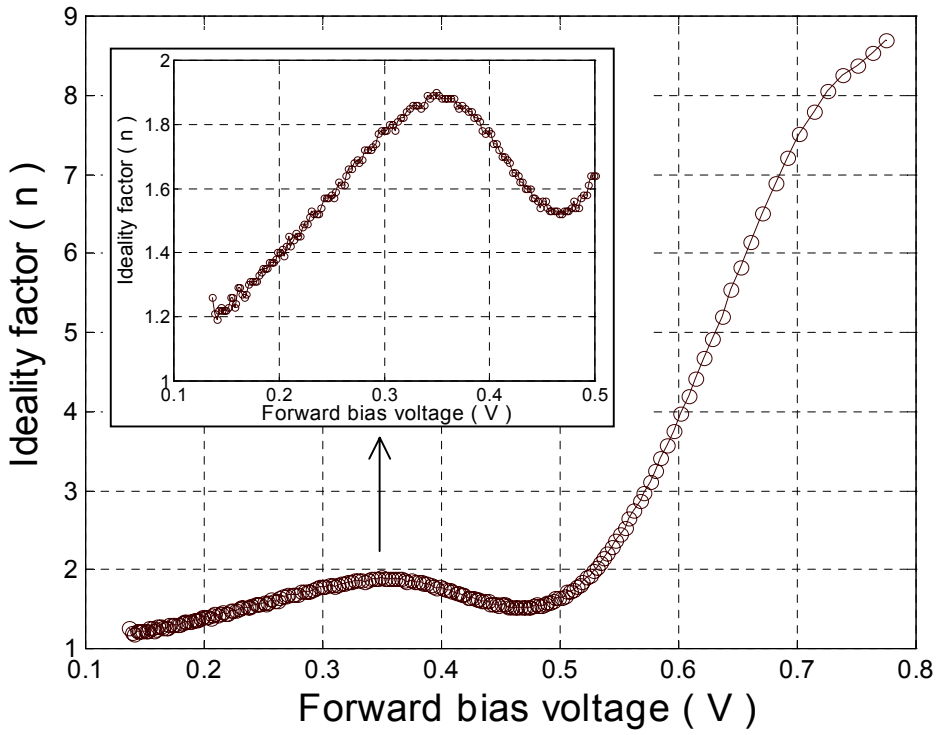

Fig. 3.3 Measured diode ideality factor

Fig. 3.4(a) shows the I-V curve comparing measurement results with the modeling data. They show excellent agreement in the whole measurement range. And, the C-V characteristic curve is shown in Fig. 3.4(b). We compare the Root-diode model, the measurement data, and an analytic modeling equation. In order to determine parameters in the analytical expression, we fit the equation (3.7) to the measurement data,

$$C(V) = \frac{C(0)}{\left(1 - V \diagup \Phi_{bi}\right)^{\gamma}} \qquad \textbf{(3.7)}$$

where the zero voltage capacitance $C(0)$ is 47 fF, the built-in potential Φ_{bi} is 0.63 V, and the junction grading coefficient γ is 0.5 [61].

The comparison between the Root-diode model, the measurement data, and the analytical modeling data looks quite good below the forward bias of 0.2 V. In general as the forward bias increases, the diffusion capacitance increases while the junction capacitance dominates in the reverse bias condition. The slight deviation from the Root-diode model is attributed to the parasitic voltage drop due to the parasitic resistance in probes and the extrinsic device series resistance. Thus, the diffusion capacitance is lower than the Root-diode model data.

Effective barrier height calculation is straightforward using a Schottky barrier diode I-V relation,

$$J_s = A^{**} \cdot T^2 \cdot \exp\left(-\frac{\phi_B - \Delta\Phi}{nkT}\right) \cdot \left\{\exp\left(\frac{qV}{nkT}\right) - 1\right\} \qquad \textbf{(3.8)}$$

where ϕ_B is the barrier height of a Schottky junction, $\Delta\Phi$ is an effective barrier lowering due to the *image force effect*, and A^{**} is an effective Richardson constant, which is assumed to be unaffected by the tunneling process (112 $A/cm^2 \cdot T^2$). We obtain the effective barrier height ($\phi_B - \Delta\Phi$) of 0.53 eV using the measured DC I-V relation.

The parasitic intrinsic series resistance and inductances are also measured varying the frequency up to 50 GHz. When performing data acquisition measurement in the Root-diode model generation, as described in Fig. 3.5, the average values are used to accommodate error tolerances in the actual model.

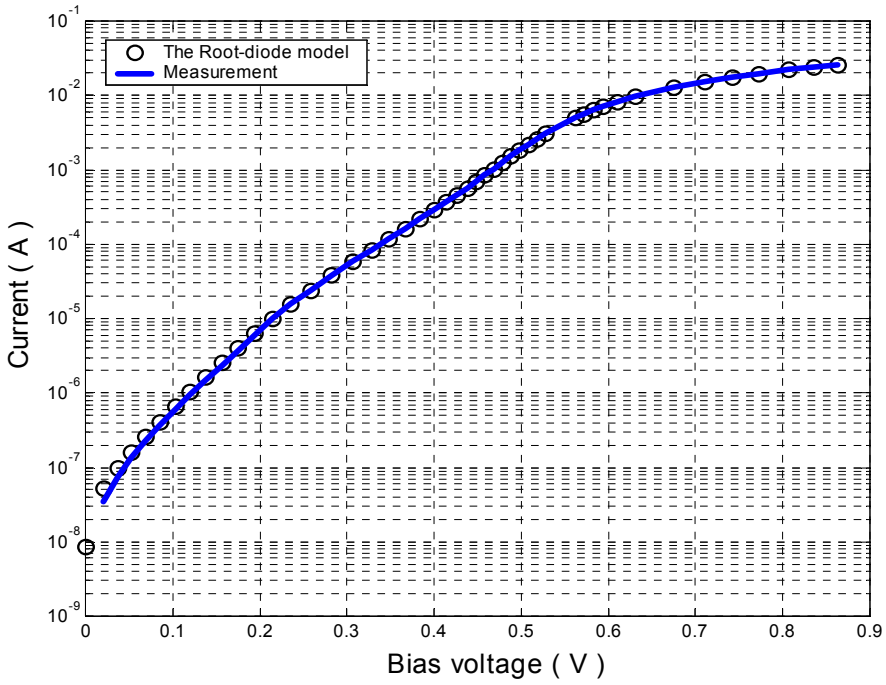

(a)

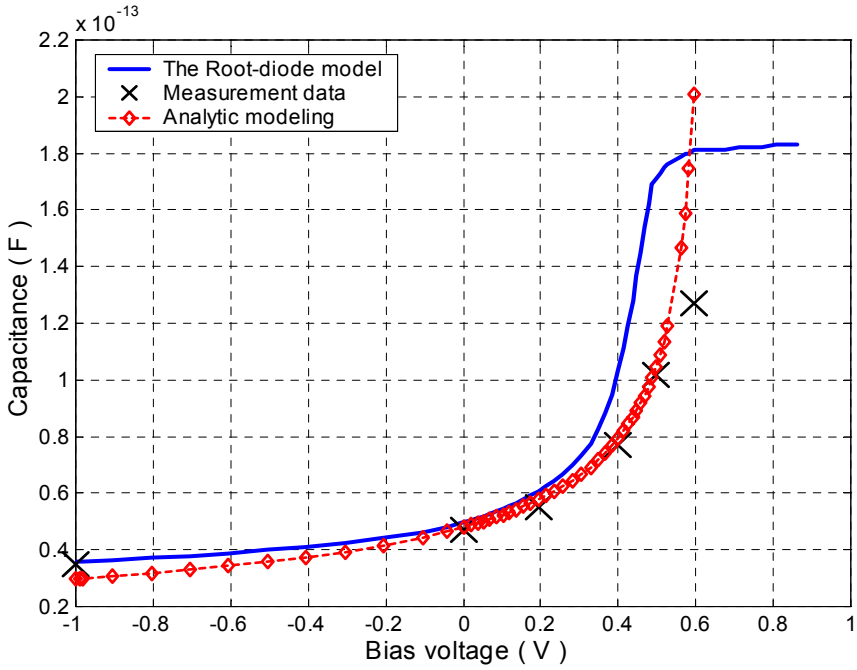

(b)

Fig. 3.4 (a) DC and (b) capacitance-voltage characteristic comparison between the Root-diode model of Si Schottky diode, the measurement data, and the analytical model

The average value of the series resistance is 12.71 Ω. However, in the data acquisition step this value is reduced to 10.5 Ω in order to satisfy model tolerance in the whole measurement range. And, the series inductance shown in Fig. 3.1, the average value of 58.56 pH is calculated from the measurement data and this value is employed in the generation step. The measured and calculated diode parameters are summarized in Table. VI.

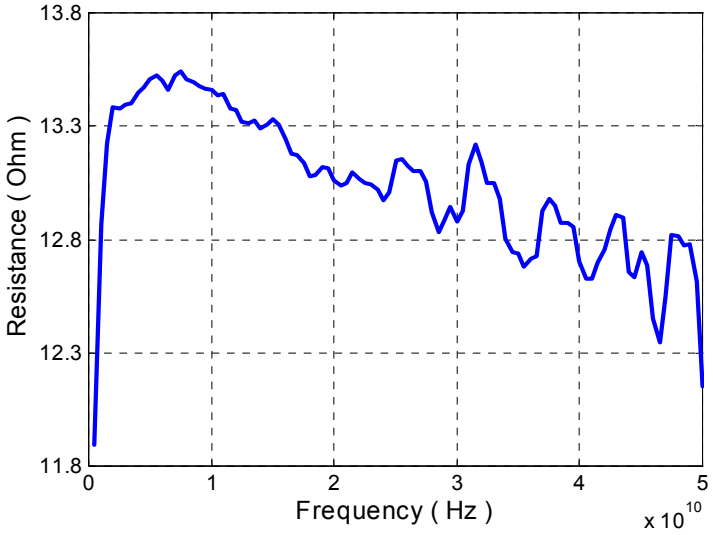

(a)

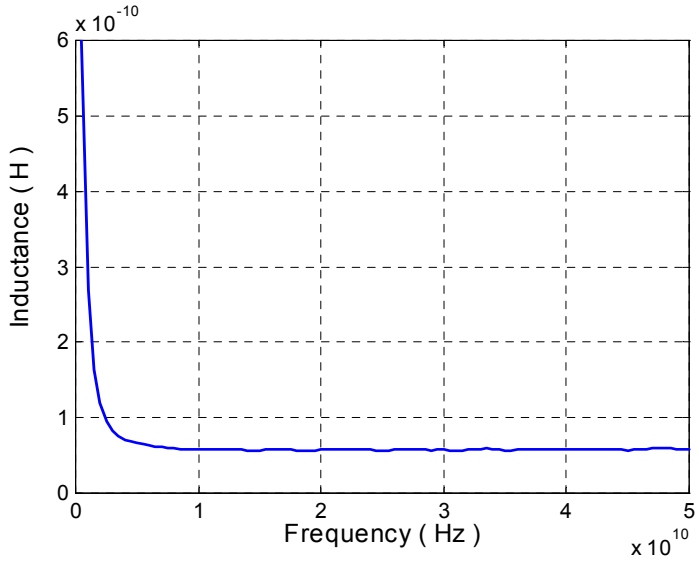

(b)

Fig. 3.5 (a) Measured intrinsic parasitic resistance, and (b) inductance.

Table. VI. Measured diode model parameters (diode area : 4.5 μm x 4.5 μm)

Terms	Value
Ideality factor	1.51
Effective barrier height	0.63 eV
Contact metal	Ni silicide
Capacitance at zero bias	48 fF
Grading coefficient	0.5
Reverse saturation current, I_s	2.7 nA
Series resistance	10.5 Ω
Series inductance	58.6 pH
Cutoff frequency	320 GHz

3.2. Flip-chip equivalent circuit modeling

In the thin-film fabrication technology, a flip-chip bonding is an important method to mount passive and active components on the same substrate. This mounting technique also allows to increase system performance, and simultaneously reduce cost compared to monolithic implementations. However, for the microwave and millimeter wave applications, the flip-chip bonding interconnect causes parasitic components due to its inherent bonding nature, namely, dielectric chip overloading on motherboard substrate, and bonding bump transition from the chip to the substrate [44]. Even though flip-chip bonding parasitics are not sufficiently large enough to deteriorate signal integrity in the low frequency or at some specific frequency area, they are to be extensively studied in case of broad and baseband signal case. They have frequency dependent behavior, therefore causing signal distortion depending on frequency, and also producing resonance phenomenon in the frequency region of interest.

In order to set up the flip-chip bonding model, a 3-dimensional electromagnetic simulator, Ansoft HFSS, is utilized for equivalent circuit modeling. In [43], an equivalent circuit model of the flip-chip bump is described for the numerical analysis (Fig. 3.6). It is composed of two capacitances, one inductance, and three conductances in parallel with each component.

The parallel capacitances are due to the dielectric overlapping of the chip and the motherboard substrate. The series inductance is attributed to the change of current density distribution and direction [44]. Conductances represent loss phenomena in the bonding structure, which include substrate and radiation losses. Substrate loss is generally caused by

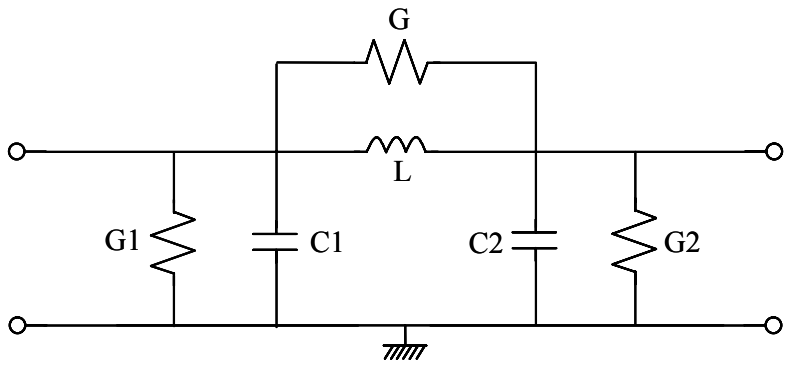

Fig. 3.6 Flip-chip equivalent circuit model.

the excitation of surface waves in the substrate. Radiation loss stems from the energy loss of radiated electromagnetic waves from the bump [43]. In this work, those losses are neglected, hence only two capacitances and one inductance are considered in the equivalent circuit modeling of the flip-chip bonding connection.

Since there are one inductance and two capacitances in the circuit model, two resonance frequencies are analytically found. If one port is terminated with Z_0, the first resonance frequency is $f_{res} = 0\,\text{Hz}$ and the second is

$$f_{res} = \frac{1}{2\pi}\left(\frac{C_2 - C_1}{2C_1C_2Z_o} + \frac{C_2 + C_1}{2C_1C_2Z_o}\sqrt{\left|1 - \frac{4C_1C_2Z_o^{\,2}}{L(C_2 + C_1)}\right|} \right). \quad \textbf{(3.9)}$$

In the transverse direction of the bump transition, Z_0 approaches ∞ [30]. In this case a transverse resonance frequency is located at

$$f_{res,transverse} = \frac{1}{2\pi}\sqrt{\frac{C_1 + C_2}{C_1C_2L}} = \frac{1}{2\pi}\sqrt{\frac{1}{L\left(C_1 \,||\, C_2\right)}}. \quad \textbf{(3.10)}$$

Various methods to reduce return loss due to the flip-chip bump transition have been developed. For example, a staggered bump method and an insertion of a hi-impedance line in order to compensate capacitive behavior of the flip-chip [46]. Those geometrical approaches are fundamentally intended to change the resonance frequency or to add (or reduce) the discrete component. It is reported that the return loss can remain below –20 dB until 82 GHz using the compensation method [46].

3.2.1. Simulation of the flip-chip bonding connection

A three-dimensional simulation structure is shown in Fig. 3.7(a). We illustrate a cross sectional view of the actual flip-chip bonded structure in Fig. 3.7(b) in order to show the origin of equivalent circuit components. It is noted that this diagram does not account for an unwanted substrate mode, i.e., parallel plate mode. An equivalent circuit model fully characterizing the

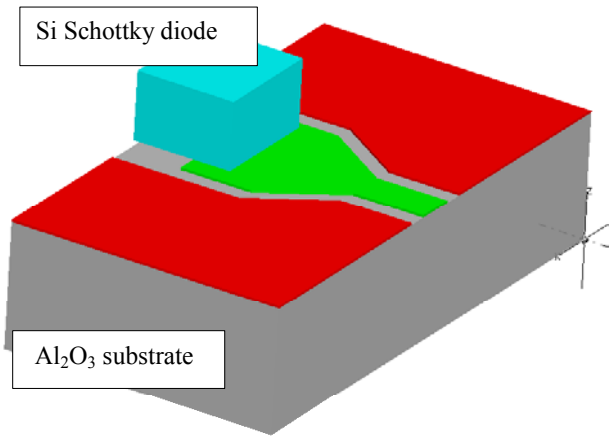

(a)

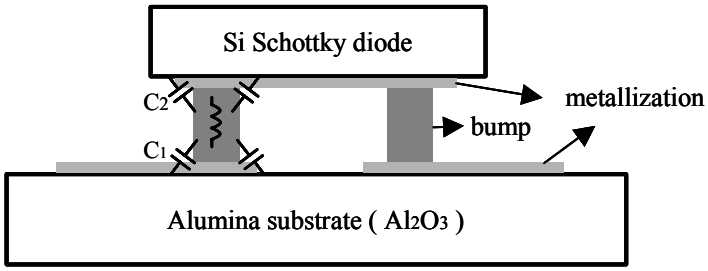

(b)

Fig. 3.7 (a) A three-dimensional simulation structure in Ansoft HFSS. Si Schottky diode is up-side down, emulating flip-chip bonding structure. (b) Cross sectional view of the flip-chip bonding.

flip-chip bonding *including* higher order modes is under research. However, the flip-chip employed circuit generally operates within a certain frequency range where higher order electromagnetic modes start to occur. Thus, it is still useful to use discrete equivalent circuit model for circuit design purposes.

The Si Schottky diode was flip-chip bonded at 300˚C to the backside grounded alumina substrate, which has a thickness of 250 μm. Bump height after bonding was measured about 5 μm on average. Mechanical bonding force 3.5 N is applied for 5~6 seconds. The used chip has two Schottky diodes connected in series, and has six pads with one bump each as shown in Fig. 3.8(a). The chip size is 500 μm x 230 μm, and each bump is made up of AuSn, and has a height of about 35 μm, as plotted in Fig. 3.8(b). Coplanar waveguides (CPWs) with tapering structures were patterned on the substrate intentionally in order to evaluate the diode and the flip-chip connection.

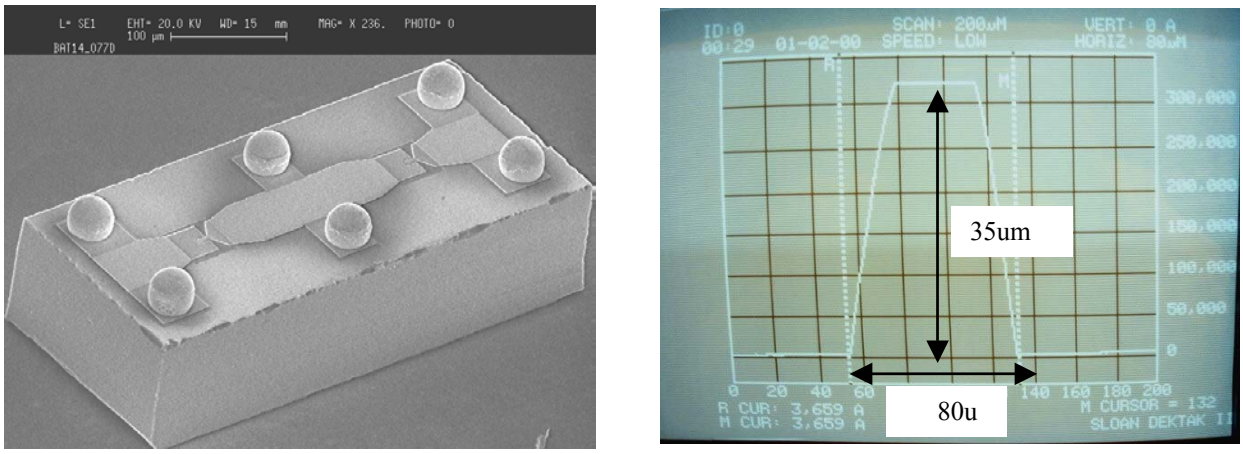

(a) (b)

Fig. 3.8 (a) A Si Schottky diode SEM photograph (b) bump height (35 µm) is measured using DekTak (*sub*micron measurement unit).

We carry out a S-parameter simulation of the structure in Fig. 3.7(a), and de-embedding the CPW line length. This CPW line is intended for the measurement purpose. Then, we obtain the de-embedded S-parameter and convert it into a Y-parameter. The Y-parameter matrix is established using the equivalent circuit model shown in Fig. 3.9.

$$\mathbf{Y} = \begin{bmatrix} y_{11} & y_{12} \\ y_{21} & y_{22} \end{bmatrix} = \begin{bmatrix} j\omega C_1 + \dfrac{1}{j\omega L} & \dfrac{-1}{j\omega L} \\ \dfrac{-1}{j\omega L} & j\omega C_2 + \dfrac{1}{j\omega L} \end{bmatrix} \quad \textbf{(3.11)}$$

Therefore,

$$C_1 = \frac{\mathrm{Im}(y_{11} + y_{12})}{\omega}, \quad \textbf{(3.12)}$$

$$C_2 = \frac{\mathrm{Im}(y_{22} + y_{12})}{\omega}, \quad \textbf{(3.13)}$$

and,

$$L_1 = \frac{1}{\omega \cdot \mathrm{Im}(y_{12})}. \quad \textbf{(3.14)}$$

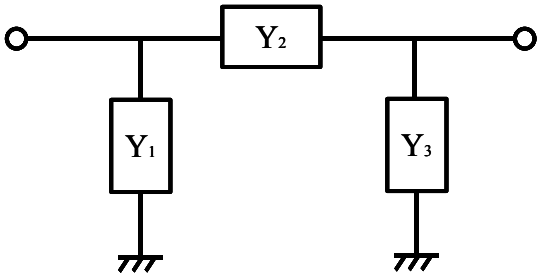

$$\mathbf{Y} = \begin{bmatrix} Y_1 + Y_2 & -Y_2 \\ -Y_2 & Y_2 + Y_3 \end{bmatrix}$$

Fig. 3.9 Y-parameter matrix of the flip-chip equivalent circuit model

In Fig. 3.10, simulation results are given varying the simulation frequency from 5 GHz to 40 GHz. As the frequency increases, C_2 value gets larger. This phenomenon can be explained as the overlapping between the dielectric chip and motherboard substrate. However, C_1 decreases because this value includes the effect of the bonding pad on the substrate which is dominant at low frequencies compared to the overlapping effect. Moreover, the summation of C_1 and C_2 is almost constant, approximately 90 fF. This means that in the low frequency region (e.g. up to 10 GHz) the overlapping effect (C_2) can be neglected compared to C_1. As the frequency increases, these effects are evenly divided showing the similar capacitance value at 40 GHz.

For a circuit design purpose, the flip-chip bonding simulation results are averaged up to 40 GHz. Those values are summarized in Table. VII.

Table. VII. Simulation result for the flip-chip bonding equivalent circuit model

Terms	Values
C_1	49 fF
C_2	42 fF
L	103 pH

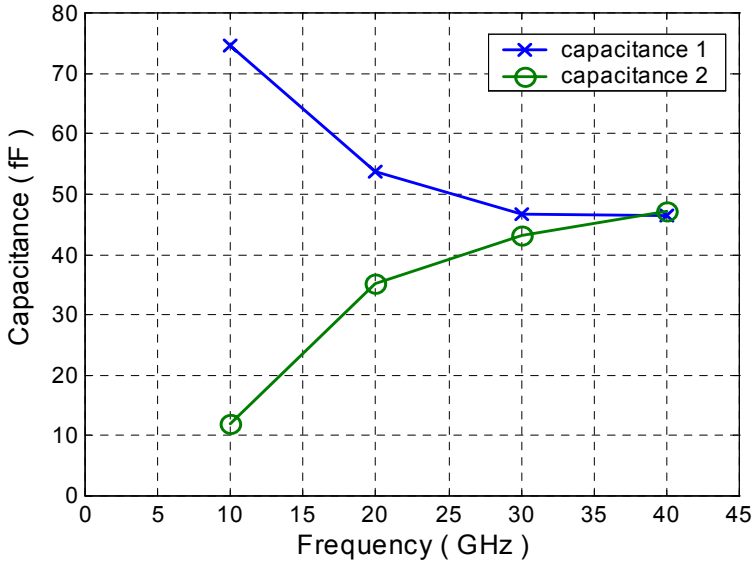

(a)

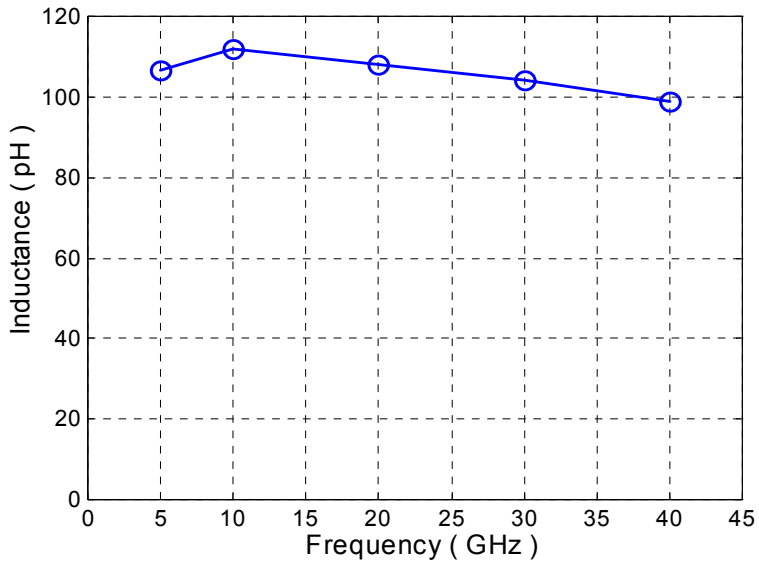

(b)

Fig. 3.10 Flip-chip simulation results for (a) capacitance and (b) inductance varying the frequency until 40 GHz for a bump height of 5 µm.

3.3. The Root-diode model and the flip-chip simulation verification

Fig. 3.11 illustrates the ADS simulation schematic, in which the Root-diode model is employed combined with the flip-chip interconnection model. Then conductor-backed coplanar waveguides (CPWs) are added to emulate the feed lines of the test circuit. For verification purpose, the comparison of measurement with simulation results is performed, shown in Fig. 3.12. For two forward bias conditions (0.3 V, 0.5 V) we carry out the simulation. A good agreement between the measured data and the simulation result assures the exact modeling of the Si Schottky diodes and the flip-chip interconnection up to 40 GHz.

In Fig. 3.13(a) and (b), the S-parameter simulation results are shown with and without flip-chip interconnection for a diode up to 50 GHz. A forward bias 0.2 V is used for the simulation. Input reflection coefficient (S_{11}) at 50 GHz shows 5 dB difference in magnitude, and forward transmission (S_{21}) shows 2.3 dB maximum difference in magnitude at 30 GHz.

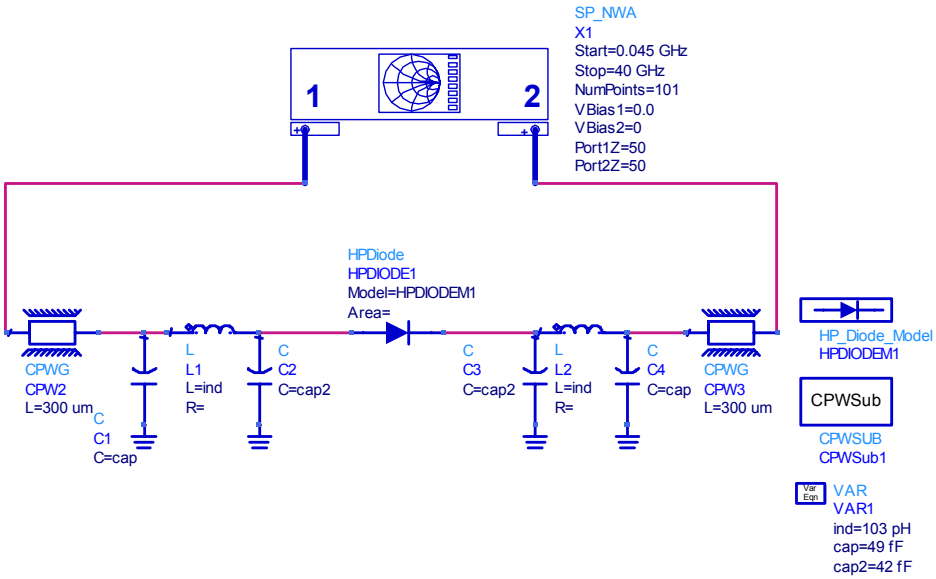

Fig. 3.11 The Root-diode model and the flip-chip interconnection model verification. Schematic in ADS simulation environment

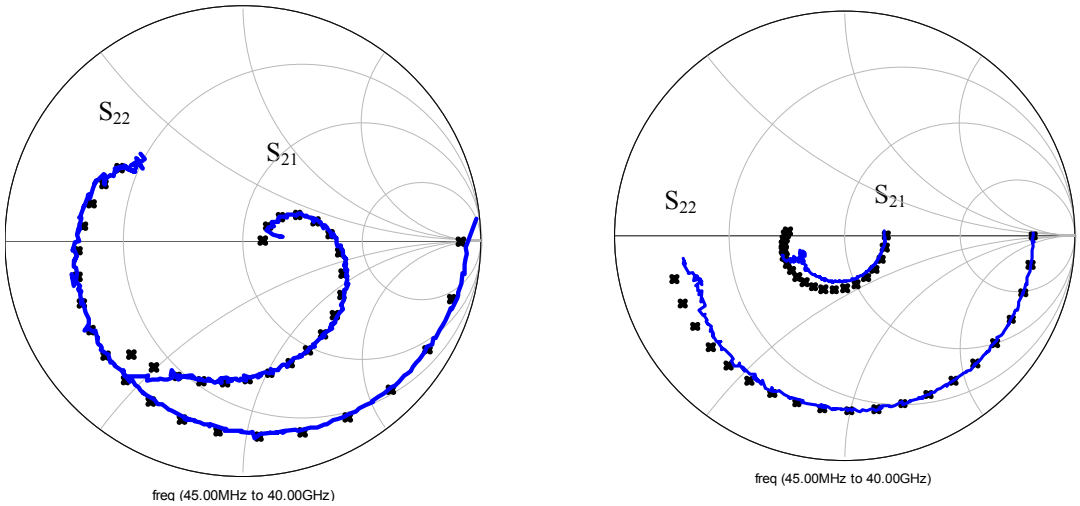

(a) $V_{forward}$ = 0.3 V (b) $V_{forward}$ = 0.5 V

Fig. 3.12 Measured (—) and simulated (x) S-parameters for flip-chip bonded Si Schottky diodes up to 40 GHz.

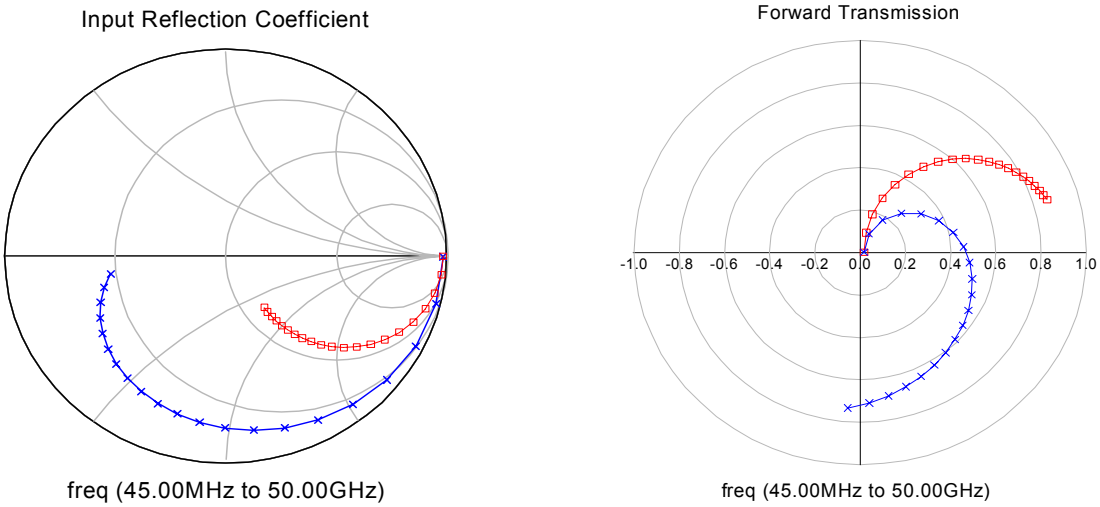

(a) (b)

Fig. 3.13 Diode performance changes after the flip-chip bonding. The simulation result for the intrinsic diode (rectangle, □) and the flip-chip effect included diode characteristic (cross, x) for (a) S_{11}, and (b) S_{21}, are shown, respectively, when $V_{forward}$=0.2 V

3.4. Design of the 43 Gbit/s demultiplexer circuit

As discussed in section 2.3, we pursue constructing a high-speed demultiplexer circuit using the Si Schottky diode instead of transistors. To do that, we need a diode sampling circuit. The 43 Gbit/s 1:2 demultiplexer circuits are designed and simulated considering both hybrid and monolithic implementations. First of all, we present sampling circuit design and simulation results. Then, a tapped delay line filter is examined and designed in the following section. When the circuit is designed under the hybrid fabrication condition, the flip-chip equivalent circuit model is attached to each diode pair. Thus, we can acknowledge how the flip-chip bonding parasitic affects circuit performances compared with the monolithic IC case.

3.4.1. A sampling circuit for the 43 Gbit/s MMIC demultiplexer circuit

3.4.1.1. A sampling circuit schematic and simulation

Fig. 3.14 shows a sampling circuit under the condition of monolithic implementation. Neglecting the flip-chip bonding connection effect, the intrinsic Root-diode model is incorporated with the circuit simulator. Three 50 Ω resistances are used in the design: one is at the input port for matching when the diode pairs are turned off (non-sampling instant). With this resistance, the input signal is completely absorbed, not being reflected back.

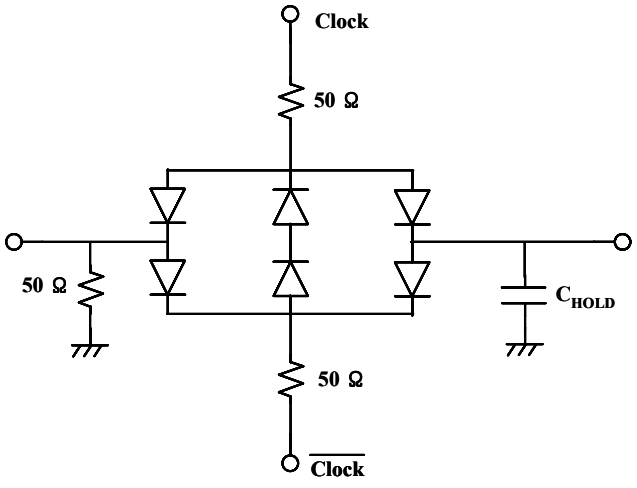

Fig. 3.14 A Si Schottky diode MMIC sampling circuit.

The other two resistances are for the oscillator signal matching. One capacitor at the output port of the sampling circuit is to hold the transferred charge from the input port. Series connected Si Schottky diodes are used in the sampling bridge circuit design. An illustrative figure of the operation mode is depicted in Fig. 3.15. Four pairs of diodes (D1, D2, D3, and D4) are aligned in the same direction, forming a signal conducting path from input to output when the sampling event occurs. One pair of diodes (D5 and D6) counteracts with the others when the oscillator signals are out of phase compared to the previous state. The oscillation signals are not reflected back due to this diode pair. A virtual ground is formed in the mid of D5 and D6 when these two diodes conduct. Thus, to match the oscillator signals, 50 Ω resistors are connected in series along the oscillator paths.

The diode switching operation is mainly dependent on the external oscillator large-signal. Once the diodes are turned on, the input signal (small-signal) can go through the circuit toward the output port. Therefore, diode small-signal current can be described by two components: One is the product of the diode junction voltage with the diode conductance, and the other is small-signal charge stored in the diode's junction capacitance [44].

$$i_{\mathrm{DIODE}}(t) = g(t) \cdot \upsilon_j(t) + \frac{d}{dt} Q(t) \qquad \textbf{(3.15)}$$

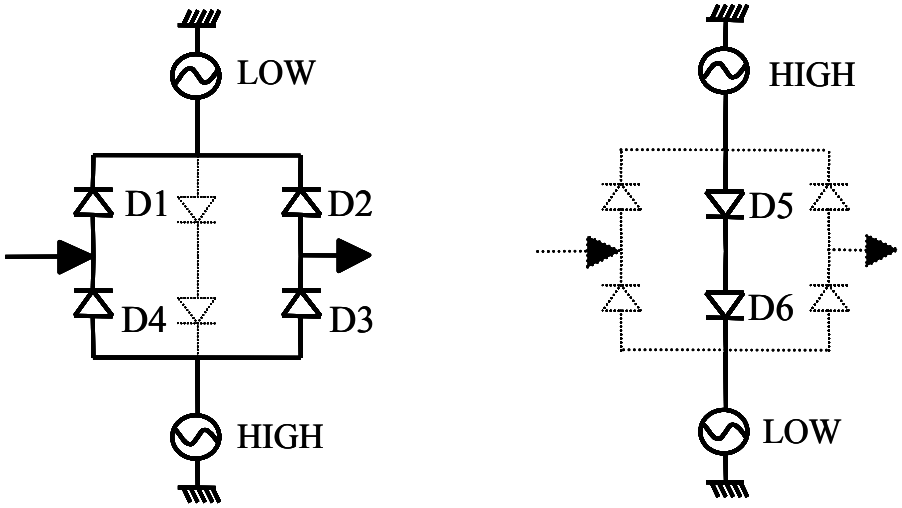

Fig. 3.15 The simplified operation modes of the bridge circuit. In the left picture, D1, D2, D3, and D4 are conducting (solid line), whereas D5 and D6 are turned off (dotted line). In the right picture, vice versa.

where, $\upsilon_j(t)$ is diode junction voltage, $g(t) = d\, i_{\mathrm{DIODE}}(t) / d\upsilon_j(t)$ is the diode *small-signal* conductance, and $Q(t) = \upsilon_j(t) \cdot C(t)$.

Because the diode capacitance is strongly dependent on the external clock signal rather than the input signal, it relies on the *large-signal*, *time-varying voltage* across the diode's junction, and is given by

$$C(t) = \frac{C_{j0}}{\left(1 - \frac{V(t)}{\Phi_0}\right)^{\gamma}} \qquad \textbf{(3.16)}$$

where, C_{j0} is the zero-voltage junction capacitance, Φ_0 is the junction built-in voltage, γ is the grading coefficient , and $V(t)$ is the *time-varying large-signal* voltage while $\upsilon_j(t)$ in the equation (3.15) is small-signal voltage across the p-n junction. Therefore, the small-signal diode current when the diodes are conducting can be expressed as follows.

$$i_{\mathrm{DIODE}}(t) = g(t) \cdot \upsilon_j(t) + C(t) \cdot \frac{d}{dt}\upsilon_j(t) + \upsilon_j(t) \cdot \frac{d}{dt}C(t) \qquad \textbf{(3.17)}$$

This formula can be interpreted that the diode current comes from three factors: the contribution of the *large-signal excitation* of a clock signal, *the time-varying small-signal input*, and *its time derivative quantity*. The transferred charge to the output hold capacitance is calculated using the following equation,

$$q_{\mathrm{HOLD}}(t) = \int_{kT}^{(k+1)T} i_{\mathrm{DIODE}}(t) \cdot dt \,. \qquad \textbf{(3.18)}$$

The instantaneous current and the charge in time domain are simulated using *Agilent* ADS. The results are depicted in Fig. 3.16. The output current is calculated using the *Kirchhoff* current law at the output port. In Fig. 3.16(a), the negative peaking is obviously shown due to the two derivative terms in equation (3.17). When either small-signal voltage across the diode junction is steeply decreased or the oscillator amplitude decreases, $i_{DIODE}(t)$ shall be below zero. We also calculated the transferred charge using the current simulation result. The time period for the calculation was 46.5 psec.

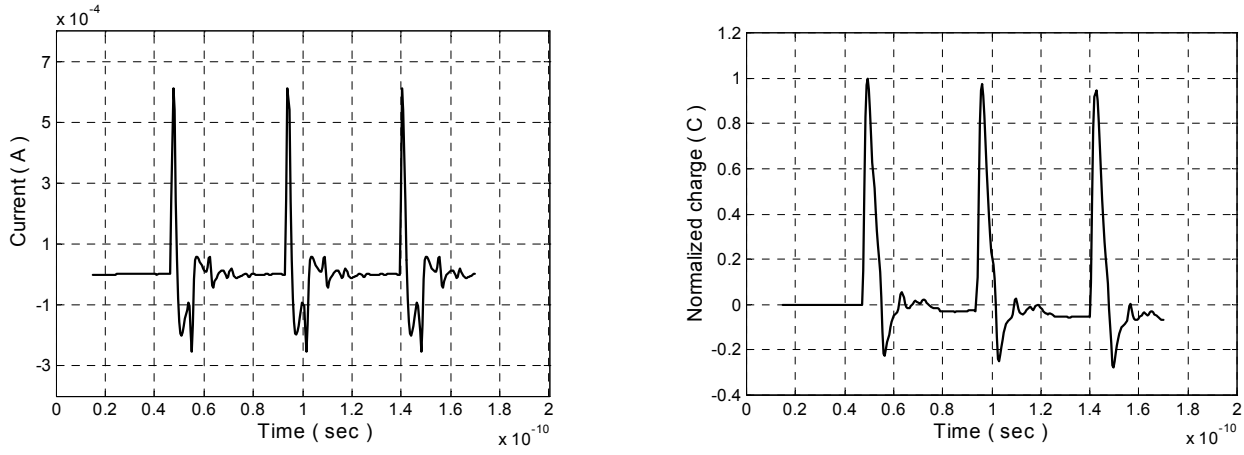

(a) (b)

Fig. 3.16 (a) Output current simulation result in the sampling circuit. (b) The transferred charge at the output port is calculated integrating the output current pulses. The charge is normalized and calculated for unity capacitor.

In fact, the small-signal diode current calculation needs both a large-signal and small-signal analysis in the sampling circuit, because the diode current is also dependent on the time drivative of the capacitance, which is changed by the large-signal of the oscillator. Analytic analysis thus needs complicated numerical analysis for our circuit simulation.

In high-speed digital applications, a linear phase characteristic is of great significance. The input signal has an ultra broadband frequency spectrum, for example 21.5 GHz fundamental frequency for 43 Gbit/s NRZ signal. A nonlinear phase response of the system will distort a signal eye waveform degrading system performance. Thus, we investigate S_{21} parameter phase characteristic and also its magnitude response. For simulations, we consider a sampling instant at which the external oscillator signal is the highest amplitude, and the diode pairs are fully conducting. The oscillator signal amplitude is set to a constant DC value, 800 mV. The hold capacitance is 0.2 pF. Even if the fixed oscillator signal amplitude does not emulate the time-varying sampling actions perfectly, it is still worth while to making use of a simple situation in order to predict circuit performance at a specific time instant. The same conditions are used for impulse response simulation in Fig. 3.18. We obtain a very broadband S_{21} characteristic over 50 GHz. Insertion loss shows 10.2 dB on average until 50 GHz. This is due to series connected parasitic component of the diode in the current conducting path and voltage dividing by 50 Ω. In Fig. 3.17(b), a S_{21} phase simulation result is illustrated with an interpolated linear phase line. The sampling circuit shows a good linear phase characteristic. The maximum discrepancy with its linear line is 4.6 ˚ at 500 MHz.

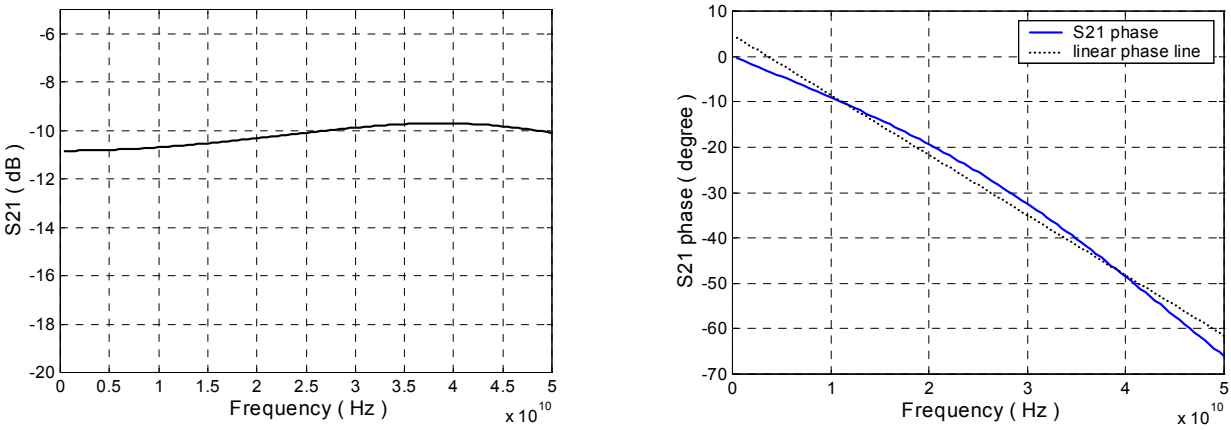

(a) (b)

Fig. 3.17 S_{21} simulation results for (a) magnitude and (b) phase.

We have simulated the impulse response varying the hold capacitances. If the pulse width of the output result is concerned, the hold capacitance value should be in the range of 0.2 pF to 0.6 pF. Here it should be noted that the output of the sampling circuit is expressed as a convolution of the impulse response and an input signal. Strictly speaking the sampling circuit is neither linear nor linear time-invariant. However, it is proved that the output is the same with the convolution sum [44][45]. And, the exact sampling circuit impulse response has been measured using the nose-to-nose method. It uses a two sampling circuits which are connected together. One generates a kick-out pulse and another measures this output pulse which are convolution sum of the kick-out pulse and its impulse response. By *de*convolving this output signal the exact impulse response is acquired [44][45][59].

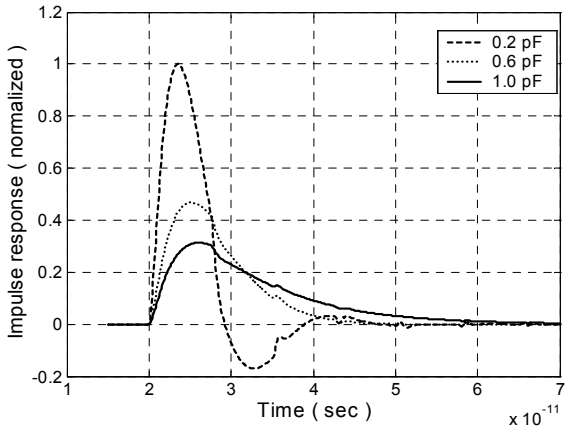

Fig. 3.18 Impulse response of the sampling circuit.

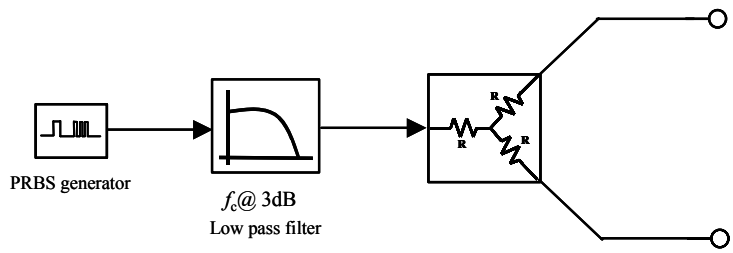

(a)

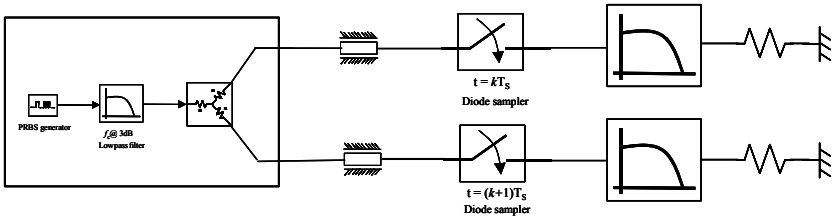

(b)

Fig. 3.19 (a) The 43 Gbit/s PRBS signal (200 mVpp) is filtered out using a Butterworth low-pass filter, and divided by the resistive power divider. (b) a 1:2 demultiplexer circuit block diagram using the sampling circuit. After the sampling circuit, the pulse shape filter (low-pass filter) is attached.

A simulation block diagram for the 43 Gbit/s 1:2 demultiplexer simulation is shown in Fig. 3.19. The ideal 43 Gbit/s pseudo random binary sequence (PRBS) of a code length of 2^7-1 is generated. Then it is filtered out using a *Butterworth* low-pass filter, which has a 3 dB bandwidth of 50 GHz, and the order of 3. The signal is divided into two signals by the resistive power divider. Due to the 6 dB insertion loss characteristic, each signal amplitude (100 mV_{pp}) is one half of the original signal (200 mV_{pp}). These signals are shown in Fig. 3.20(a) and (b) with their FFT transforms, respectively. The ideal 43 Gbit/s NRZ signal clearly shows spectral distribution with multiple dips at integer times of 43 GHz. After filtering, amount of signal power below 43 GHz is still remained, thus the simulated eye waveform does not show a critical distortion. In general, the power spectral density of the NRZ signal shows a $sinc^2$ distribution. This fact is obvious from Fig. 3.20(a).

The divided signals are incident on the sampling circuit. The oscillator power for each sampling circuit is 2 dBm (~800 mV_{pp}). The required oscillator power shall be determined as the following. The minimum power at least should turn on the diodes while the maximum power in the diodes should be lower than the thermal breakdown and the reverse breakdown (22.5 dBm).

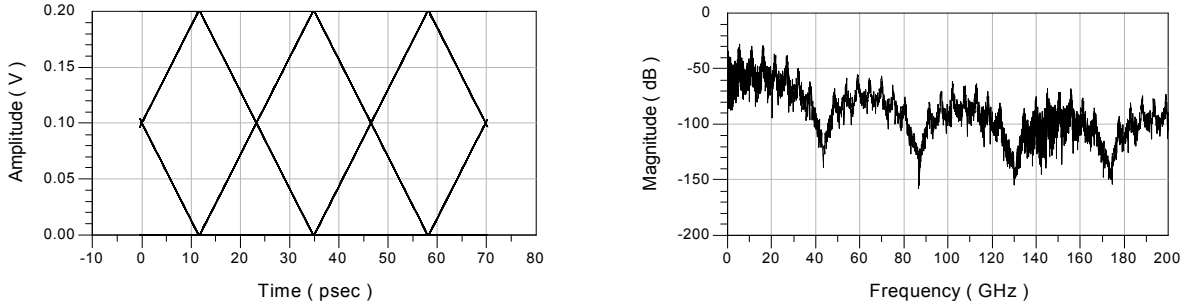

(a)

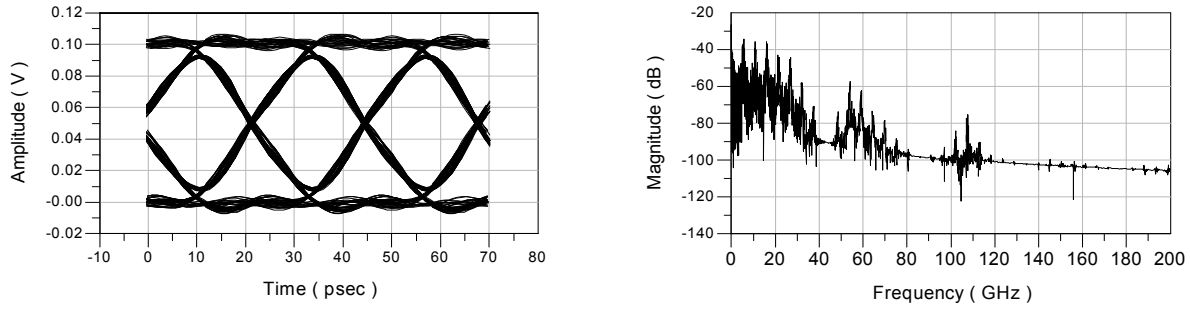

(b)

Fig. 3.20 (a) Ideal 43 Gbit/s eye diagram, and its FFT result. 43 Gbit/s NRZ signal has a period of fundamental frequency component of signal, 43 GHz. (b) Filtered 43 Gbit/s NRZ signal. High frequency component is considerably reduced.

A pulse shaping low-pass filter (Bessel-Thompson filter having a bandwidth of 10.75 GHz and the order of 5) is added to obtain the demultiplexed signal waveform. In addition, we employ one commercial amplifier to increase signal amplitude [52]. The amplifier has a gain of 15 dB up to 42 GHz. The measured S-parameters for the amplifier is added to the circuit schematic for the demultiplexer circuit simulation. The delay of the oscillator signal is tuned observing the output eye waveform. The simulated output waveforms for two channels are shown in Fig. 3.21. We use a hold capacitance of 0.2 pF at the output of the sampling circuit. Compared with Fig. 2.11, which is an ideal demultiplexed waveform, the simulation results using the actual diode model show a good agreement. The waveform is still NRZ-like waveform. However, we note that the eye waveform is distorted due to the intersymbol interference. This is caused by the pattern dependent *deterministic* behavior of the circuit. Furthermore, the distorted bit and the adjacent bit differ from the channel number. Therefore, we shall model these distorted channel results as two coupled channels. Each channel generates a *crosstalk* depending on the bit pattern. The amount of crosstalk quantity will be calculated using the aforementioned zero-forcing algorithm.

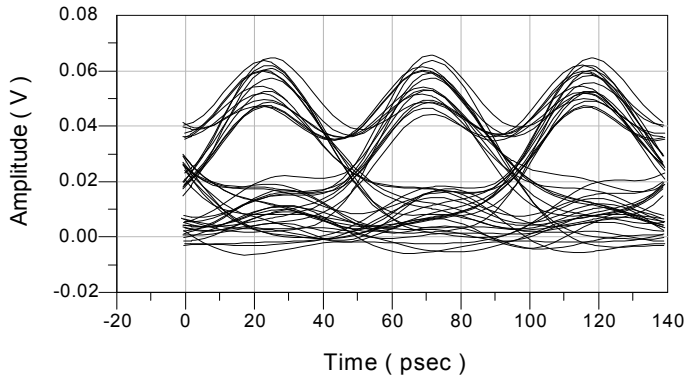

(a)

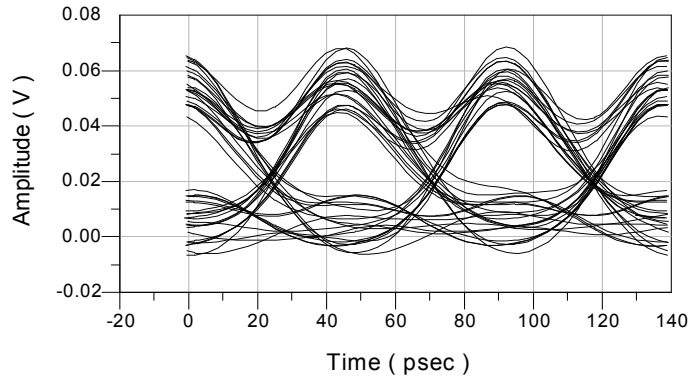

(b)

Fig. 3.21 Eye diagrams of demultiplexed (a) channel 1 and (b) 2, respectively. (C_{HOLD}=0.2 pF)

3.4.2. The transversal tapped delay line filter

A tapped delay line filter is designed for the purpose of reducing the ISI phenomenon. We consider that the finite number of symbols, 2M+1, will affect the ISI. Thus, the *k*th output symbol, $\hat{s}_{out,k}$, is a function of 2M+1 elements given by

$$\hat{s}_{out,k} = f(s_{k-M}, s_{k-M+1}, \ldots, s_k, s_{k+1,} \ldots, s_{k+M-1}, s_{k+M})$$

$$= \sum_{j=-M}^{M} p_j s_{k+j} \qquad (3.19)$$

$$= p_0 s_k + \sum_{\substack{j=-M \\ j\neq 0}}^{M} p_j s_{k+j}$$

where, using equation (2.76) p_k is expressed as,

$$p_k = \underline{\mathbf{G_k}}^{\mathbf{H}} \cdot \underline{\mathbf{h_k}} = \sum_{i=-L}^{L} g_{i,k} h_{k-i} \,. \qquad (3.20)$$

The condition to satisfy the zero-forcing algorithm can be alternatively described using parameter p_k given by,

$$p_k = \begin{cases} 1 & \text{if } k = 0 \\ 0 & \text{otherwise} \end{cases}. \qquad (3.21)$$

Here we use the normalized parameter p_k. In order to apply this algorithm to the transversal equalizer circuit design, we consider the simple case for M=1. It means that the output is assumed to be affected by one past and one future bit.

$$\hat{s}_{out,k} = \alpha \cdot s_{k-1} + s_k + \beta \cdot s_{k+1} \qquad (3.22)$$

Expressing the above equation in *z*-domain, the transfer function is given by

$$H(z) = \alpha \cdot z^{-1} + 1 + \beta \cdot z \qquad \textbf{(3.23)}$$

Applying (3.23) into (3.20), we obtain the transversal tapped delay line filter coefficients as,

$$g_{-1} = \frac{-\beta}{1-2\alpha\beta},\ g_0 = \frac{1}{1-2\alpha\beta},\ \text{and}\ g_1 = \frac{-\alpha}{1-2\alpha\beta}. \qquad \textbf{(3.24)}$$

Therefore, we can conclude that the equalizer transfer function is written by,

$$H_{EQ}(z) = \frac{1}{1-2\alpha\beta}\left(-\beta \cdot z + 1 - \alpha \cdot z^{-1}\right) \qquad \textbf{(3.25)}$$

Comparing the equalizer transfer function with Fig. 3.22, and assuming the symmetry between two channels, the coefficients can be chosen as,

$$C_0 = D_0 = \frac{-\beta}{1-2\alpha\beta} \approx -\beta,\ \text{and}\ C_1 = D_1 = \frac{-\alpha}{1-2\alpha\beta} \approx -\alpha\ . \qquad \textbf{(3.26)}$$

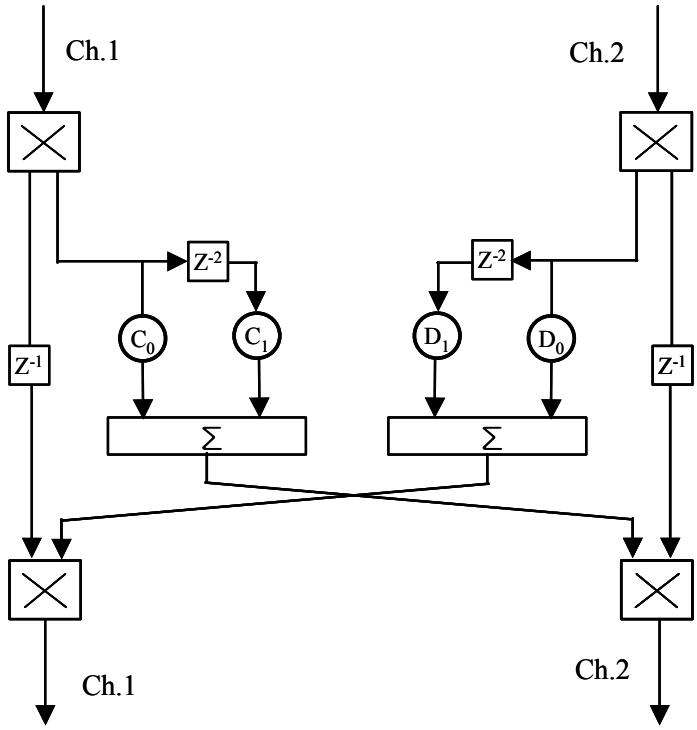

Fig. 3.22 Proposed transversal filter to equalize ISI phenomena.

In determining the coefficients α and β, first of all the ISI quantity should be considered. We employ (……0001000……) symbols to see how much ISI affect the adjacent bit. A single '1' bit is applied to a sampling circuit for channel 1, then we observe the ISI-affected waveform of the adjacent bits in channel 2. The following equation is used to decide the coefficients,

$$\rho\big|_{ISI} = \left| \frac{\max\left\{ \sum_{m=-K}^{K} S_{sampler}(t)\big|_{Ch.2} * h_{LPF}(t)\big|_{t=mT_s} \right\}}{\max\left\{ S_{sampler}(t)\big|_{Ch.1} * h_{LPF}(t)\big|_{t=T_{MAX}} \right\}} \right| \qquad \textbf{(3.27)}$$

where K represents the number of significance bits, T_s is an optimum sampling instant for channel 2, and T_{max} is for channel 1. By circuit simulation, we find out the coefficients. $\alpha = \beta = 0.167$ ($-15.56\,\text{dB}$). A simulation result is given in Fig. 3.23.

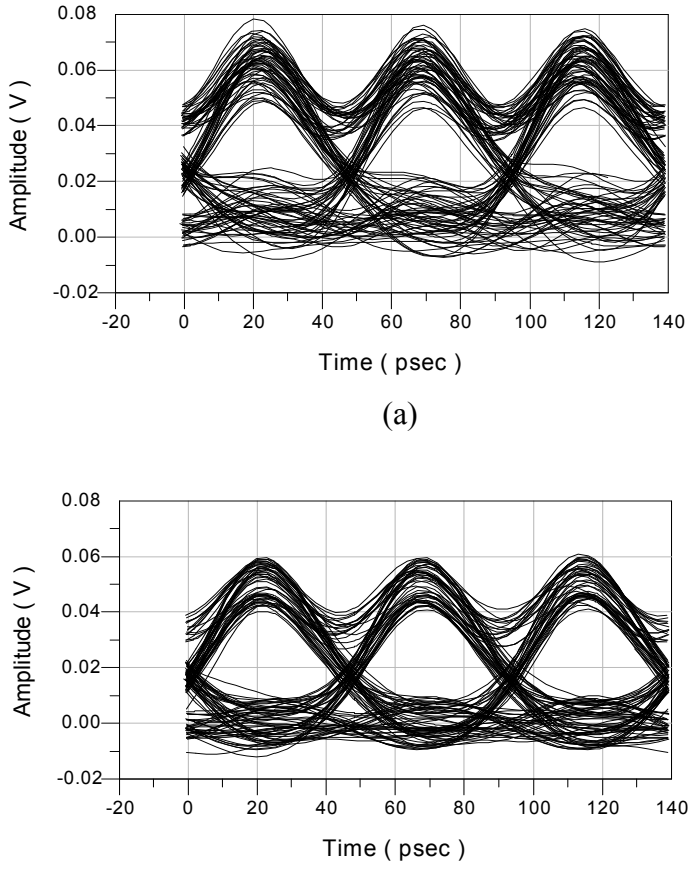

Fig. 3.23 Eye waveform (a) before equalization, and (b) after equalization

To evaluate the equalizer circuit performance we calculate eye opening using the following equation [55],

$$\text{Eye opening} = \frac{\min_k(\hat{s}_{k,out}|s_k = 1) - \max_k(\hat{s}_{k,out}|s_k = 0)}{Y} \cdot 100 \quad (\%) \qquad \textbf{(3.28)}$$

where Y means the ISI free case. In Table. VIII, the eye opening calculation is summarized.

Table. VIII Eye opening calculation *before* and *after* equalization.

	before equalization	after equalization
Eye opening (%)	45.3 %	57.6 %

It is noted that the *adaptive* signal processing to track the impairments from the imperfect receiver response is preferred to enhance the signal integrity. However, recognizing the operability of commercial devices up to multi gigabit-per second data rates (for instance, power amplifier, power divider, delay lines, and filters), the constraint exists in case of 80 Gbit/s and 160 Gbit/s for equalizer realization. So far, electronic equalization has been reported in [53]-[57] using adaptive and non-adaptive ways, which include linear, non-linear and maximum-likelihood methods. Even though the proposed transversal filter equalization method is adaptable to many types of distortion, this technique has also disadvantages [57]. Among them, one peculiar characteristic of this type equalizer is the amplification of the noise at specific frequency, therefore it requires many taps to compensate. The other is the disability for non-linear distortions.

3.4.3. 43 Gbit/s hybrid demultiplexer circuit

A hybrid sampling circuit is designed considering the flip-chip bonding technology. The flip-chip equivalent circuit in Fig. 3.6 is applied to the circuit design. An alumina substrate and the conductor-backed coplanar waveguide (CPW) with via holes are also employed. The circuit schematic is fundamentally the same as in Fig. 3.14. We investigate the circuit performance comparing with the MMIC circuit simulation results. Also, the tapped delay line filter simulation is carried out. First of all, Fig. 3.24 shows impulse responses of the hybrid sampling circuit for various hold capacitors.

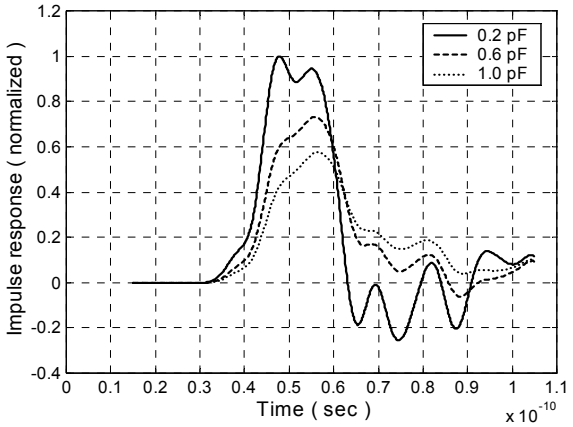

Fig. 3.24 Impulse response simulation results including flip-chip parasitics for various hold capacitances.

The simulation condition is the same with that of the MMIC sampling circuit. It is obvious from Fig. 3.24 that flip-chip parasitics change its intrinsic impulse response considerably. Rise and fall time increase in the hybrid circuit, and a trailing edge is more irregularly oscillating and seldomly die out completely as simulation sweeping time increases. The *full width at half maximum* (FWHM) value is measured. It increases from 6 psec to 18 psec in the hybrid circuit when the hold capacitance is 0.2 pF. The S_{21} parameter simulation results are shown in Fig. 3.25. They are compared with MMIC circuit simulation results. The simulated 3 dB cutoff frequency is 26 GHz while in the MMIC circuit above 50 GHz cutoff freqeucny is estimated. The phase changes more rapidly in the hybrid circuit. Above 43 GHz the nonlinear phase characteristic starts to show up. We investigate the group delay characteristic. Until 37 GHz, it deviates ±13 psec from the average value, 31.5 psec. Around 50 GHz spectral components begin to be lagged down.

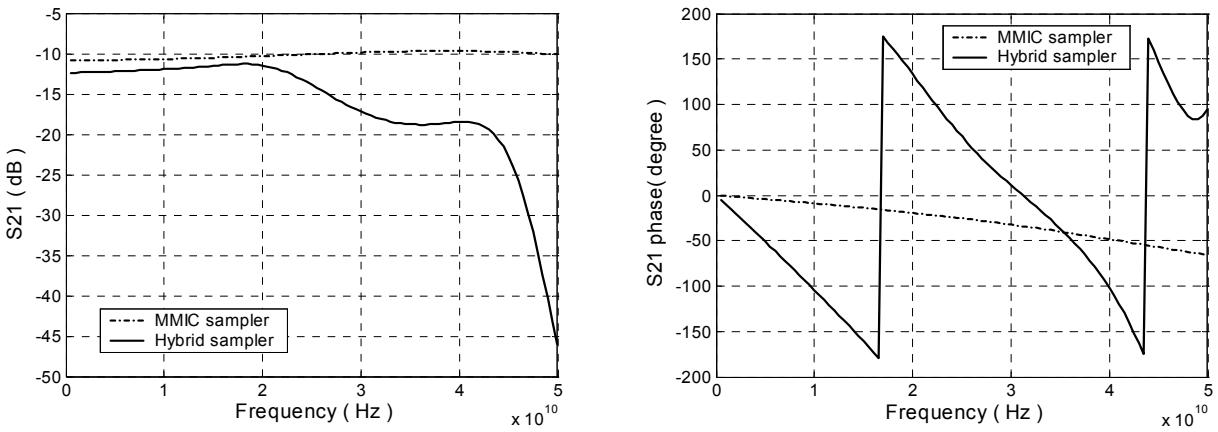

Fig. 3.25 S_{21} of the hybrid circuit is compared with those of the MMIC sampling circuit for (a) magnitude and (b) phase.

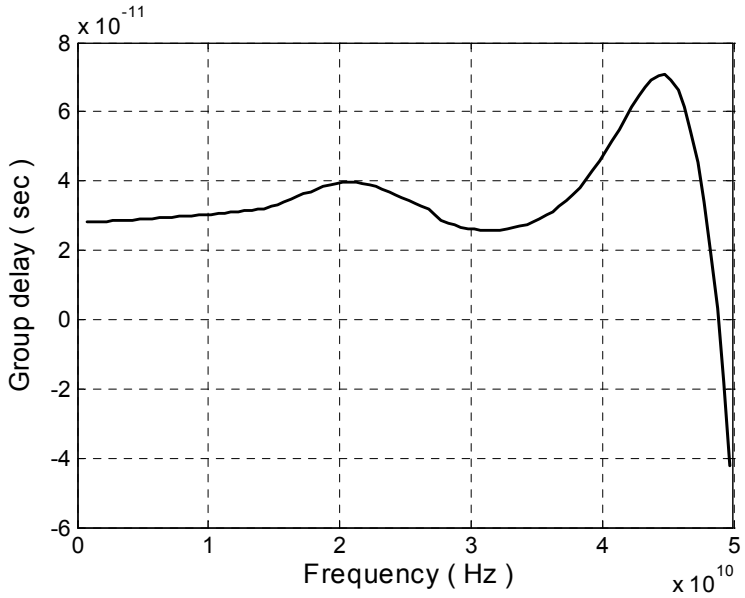

Fig. 3.26 Group delay of the hybrid sampling circuit.

The hybrid sampling circuit simulations for the demultiplexer are done with the equalizer. Their results are given in Fig. 3.27. Simulation conditions are all the same with the MMIC case. The hold capacitance value is 0.2 pF, and the equalizer coefficients are 15 dB. In contrast to the MMIC circuit simulation results, the equalizer enhances the eye opening by 5 %.

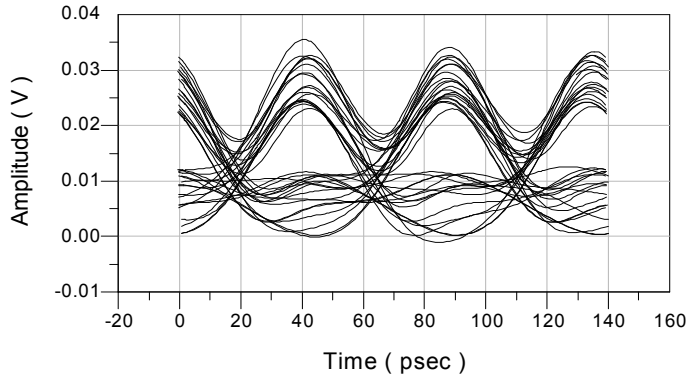

(a)

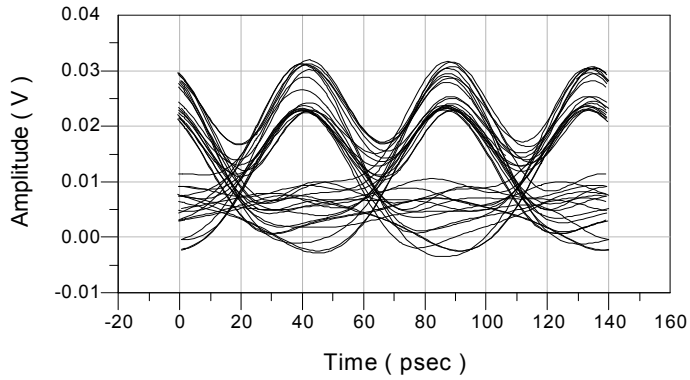

(b)

Fig. 3.27 The hybrid circuit simulation result (a*) before* and (b) *after* equalization

This small enhancement can be explained with regard to the irregular trailing edge in the impulse response. The edge affects several adjacent bits, thus the equalizer circuit needs more than three taps. And, it is sophisticated to determine the filter coefficients because the ISI depends on both bit patterns and the *irregular* trailing edges by each pattern. So, we use the averaged coefficient value for the equalizer circuit simulation. Those constant should be verified with the experimental result. It is noted that the output amplitude is reduced by half compared with the MMIC simulation result. The main loss comes from the flip-chip parasitics.

For the equalizer in the hybrid sampling circuit, the adaptive algorithm is another choice to consider. Keeping track of the eye waveform variation, the filter coefficients can be adaptively changed and the clean eye waveform is obtained. However, the complexity of the receiver structure and the high-speed adaptive signal processor implementations are also considered.

3.5. 86 Gbit/s MMIC 1:2 demultiplexer circuit

3.5.1. 86 Gbit/s MMIC 1:2 demultiplexer

In this section we show that the sampling concept using Si Schottky diodes for the demultiplexer circuit is feasible for an 86 Gbit/s 1:2 demultiplexer or higher speed circuit implementation. We propose a circuit schematic and present simulation results for an 86 Gbit/s demultiplexer. It is of significance to show that the Si Schottky diode sampling circuit would be expanded into a higher bit rate communication circuit. Circuit simulation results are provided supporting this fact. A linear equalizer circuit is also utilized to obtain a demultiplexed signal waveform. As discussed in chapter 1, this work is motivated by the fact that high-speed digital circuits can be implemented by analog ways using Si Schottky diodes. Challenging to the 86 Gbit/s demultiplexer circuit, we present the Si Schottky diode sampling circuit based demultiplexer circuit and simulation results.

3.5.1.1. Operation principle and simulation results

The circuit topology is different from the 43 Gbit/s 1:2 demultiplexer circuit. In order to achieve higher bit rate using Si Schottky diodes, the structure itself is minimized. The same diode model in the previous section is used for 86 Gbit/s MMIC 1:2 demultiplexer circuit simulation.

Eliminating the requirement of the broadband resistive power divider, an integrated 1:2 demultiplexer is developed (see Fig. 3.28). It is composed of two sampling circuits. Both of them are equivalent and connected in parallel sharing the same oscillator signal. The distinct difference is the direction of the diode pair. The diodes are anti-parallel, but each sampling circuit is fundamentally identical. Compared with the sampling circuit for the 43 Gbit/s 1:2 demultiplexer, a 50 Ω matching resistance is removed and the number of used diodes is smaller than that of the 43 Gbit/s sampling circuit. It is also beneficial to use the decreased number of oscillator signal, because we do not need to supply high power oscillating signal for the switching operation. The illustrative figure is illustrated in Fig. 3.28. Depending on the clock signal amplitude, diode pairs are either conducting or not. Because diode pairs are anti-

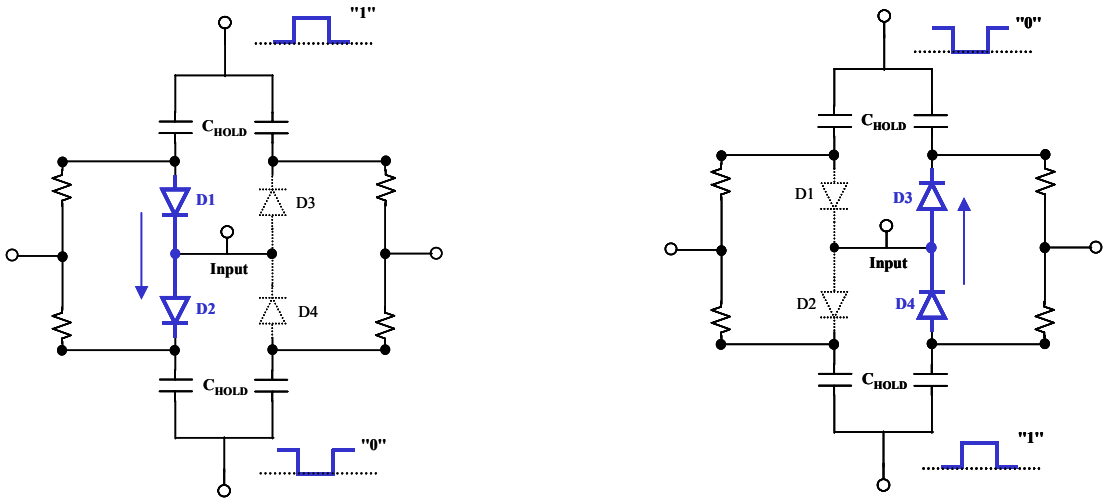

Fig. 3.28 An 86 Gbit/s demultiplexer circuit operation principle is illustrated when (a) only D1, and D2 diodes are conducting, and (b) only D3, and D4 are conducting. In each case, their clock signal amplitude is presented.

parallel each other, one diode pair flows current during the other remains off-state, and vice versa. Thus, in either case, the input signal can find the path to flow toward one of the output ports. In this way, the resistive power divider can be removed. When analyzing the circuit operation, time-domain method is performed to characterize time-dependent impedance and current. Small-signal bandwidth analysis also is carried out, and they are presented in [63][64]. The eye diagram simulation results are shown in Fig. 3.29. The hold capacitance is 0.2 pF and oscillator signal power is 0.88 dBm ($700mV_{pp}$).

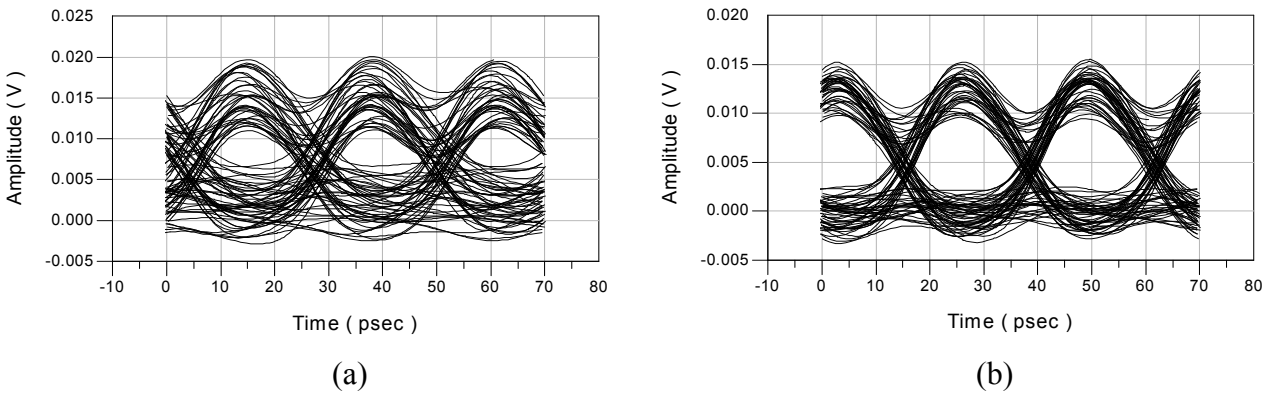

Fig. 3.29 The 86 Gbit/s MMIC 1:2 demultiplexer circuit simulation results using Si Schottky diode sampling circuit. Demultiplexer circuit output signals are presented (a) *before* and (b) *after* equalization

At the end of the output port, a low-pass filter (Bessel filter of order 5 and bandwidth of 21.5 GHz) is connected to form a 43 Gbit/s NRZ waveform. In 86 Gbit/s optical receiver application, we use 86 Gbit/s RZ signal as an input signal to the sampling circuit and generate the signal using the 5^{th} order Bessel filter having a bandwidth of 55 GHz. The filtered signal has a peak amplitude of 200 mV_p. The ideal signal and the filtered RZ signal are shown in Fig. 3.30. As shown in Fig. 3.30(b) and (d), the 86 Gbit/s RZ signal has a spectral peak at odd multiples of 86 GHz, i.e., 86 GHz, 258 GHz. The spectral peak at 86 GHz shall be used to synchronize the data stream with the clock signal in phase-locked loop (PLL) circuit. The circuit output signal is post processed with a linear tapped delay line filter, which is explained in section 3.4.2. We find out the filter coefficients using equation (3.27). The constants, $C_0=D_0=C_1=D_1$= -10 dB, are calculated in the same way as discussed in section 3.4.2. We use equation (3.28) to get eye opening parameter. It is obvious that the eye opening is improved considerably from 33.3 % to 58.3 %. Therefore, we are in success to show that the 86 Gbit/s demultiplexer circuit is feasible using Si Schottky based sampling circuit.

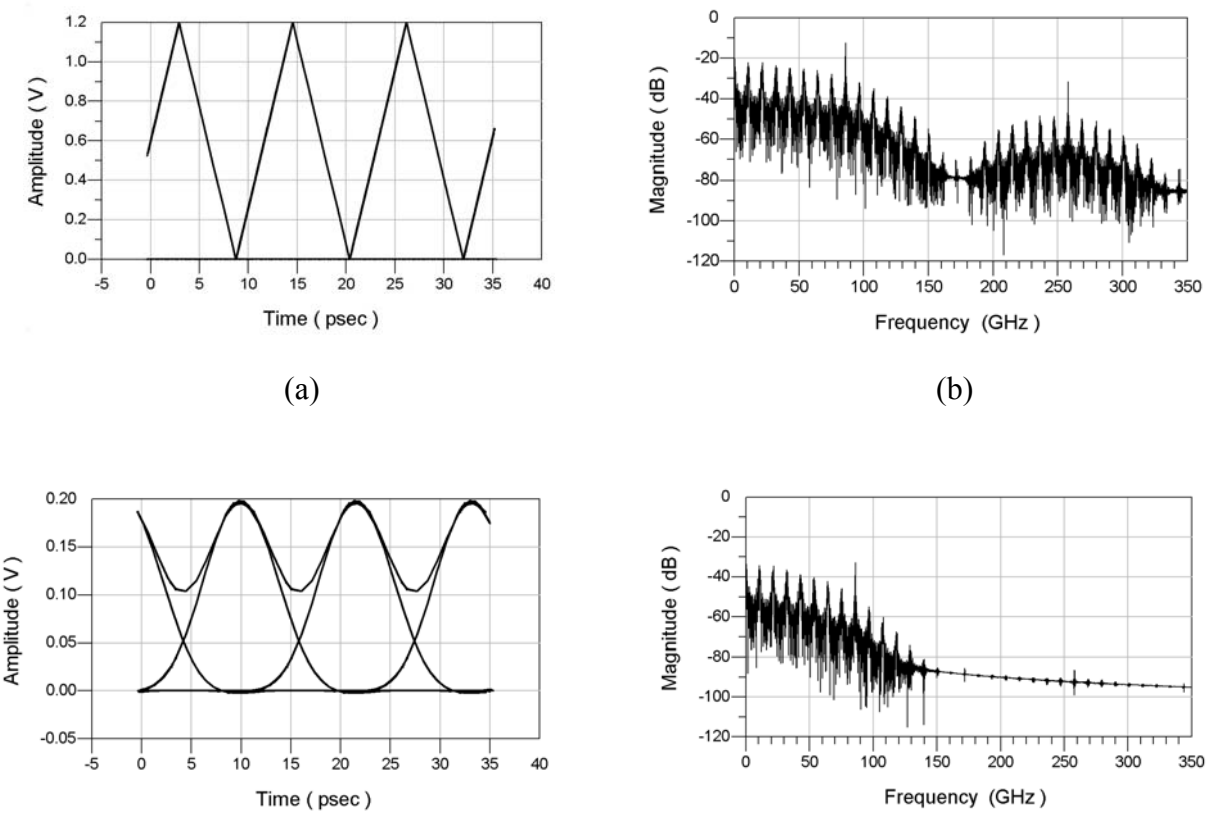

Fig. 3.30 (a) Ideal 86 Gbit/s RZ signal eye diagram, and its FFT result. (b) Filtered 86 Gbit/s RZ signal.

Chapter 4 Fabrication and Measurements

4.1. Coplanar waveguide measurement and analysis

The hybrid technology is employed to fabricate the designed sampling circuit. To do so, first of all, conductor-backed coplanar waveguides (CPWs) with via holes are designed and fabricated using the alumina substrate with 10 mil (254 μm) thickness. The significant electrical parameters of the substrate to consider are summarized in Table. IX.

First of all, in high-speed digital circuit applications the substrate thickness should be decided carefully. As the substrate thickness increases with constant W/S ratio (Fig. 4.1(b)), the higher-mode cutoff frequency decreases. When the cutoff frequency is inside the spectral region of interest, the digital signal waveform suffers from distortion. In a conductor-backed dielectric slab waveguide, the first higher mode (TE_1 mode) cutoff frequency is inversely proportional to dielectric thickness, and it is given by

$$f_{TE1} = \frac{c}{4h\sqrt{\varepsilon_r - 1}} \qquad \textbf{(4.1)}$$

where h means the substrate thickness, c is the light velocity, and ε_r is the relative dielectric constant of the substrate. Thus, the substrate thickness, W, and S should be chosen in order to increase the cutoff frequency of the first higher mode of the slab waveguide and of the CPW.

(a) (b)

Fig. 4.1 (a) Coplanar waveguide mode (b) parallel-plate (PPL) mode.

However, as the dielectric height is reduced in the conductor-backed CPW close enough to affect the coplanar waveguide field distribution, the CPW mode field pattern starts to be altered allowing *so-called* the parallel-plate line (PPL) mode. This mode changes the field profile of the dominant mode in the CPW. Thus, it changes the propagation properties of the CPW and also couples the power to the other parts of the circuit. For example, in the amplifier MMIC circuit, the feedback path due to the resonance phenomena of the PPL mode in the conductor-backed CPW causes the power coupling. It results in the instability and cross talk between the signal lines [68]. Therefore, the substrate thickness in high-speed digital circuit shall be determined considering the higher-order mode cutoff frequency and the CPW mode field profiles of the given CPW structure.

Secondly, the dielectric constant is to be considered. In addition to the effect on the cutoff frequency in equation (4.1), if the dielectric constant is high, the field profile is concentrated into a smaller area. Thus, we realize the high density of components in a motherboard. But, with a lower dielectric constant the field energy is distributed in broader region. It causes the crosstalk between the digital signal lines and higher radiation losses [66]. Thus, the dielectric constant should be chosen after examining the effects on the circuit layout and frequency range of interest.

And, finally metal thickness and its conductivity should be cared. The metal thickness should be larger than the skin depth given by

$$\delta(f) = \sqrt{\frac{1}{\pi \mu f \sigma_{cond}}} \qquad \textbf{(4.2)}$$

where $\mu = \mu_0 \mu_r$ is the permeability of the conductor, and σ_{cond} is the conductivity of the metal.

Table. IX Alumina substrate parameters for simulation

Terms	Value
Substrate thickness	10 mil
Metal thickness	5 μm (Au)
Dielectric constant	9.9

4.1.1. Conductor-backed CPW with via holes

Conductor backed CPWs with via holes are fabricated and measured up to 100 GHz. The placements of the via holes in the conductor-backed CPW could effectively suppress the parallel plate mode [67]. When the finite width ground planes on the CPW have open boundaries, these two ground planes are considered as two patches with a feeding structure along the center of two patches. These patches are coupled with a signal line and have a resonant frequencies written by [67],

$$f_{mn} = \frac{c}{2\sqrt{\varepsilon_r}} \cdot \sqrt{\left(\frac{m}{W_g}\right)^2 + \left(\frac{n}{L_g}\right)^2} \qquad \textbf{(4.3)}$$

where c is the light velocity, ε_r is the dielectric constant of the substrate, m, n is the mode index, W_g and L_g is the width and the length of the ground patch on the CPW, respectively. At resonant frequencies, the field distribution which is normal to the CPW plane (penetrating direction of Fig. 4.2) has a maximum at the periphery of ground planes. Placing the via holes at the E-field maximum points caused by the resonance of the patch and allocating them along the ground edge of the conductor-backed CPW as close as possible to the feeding line, transmission characteristics of the coplanar lines can be improved considerably [67][69].

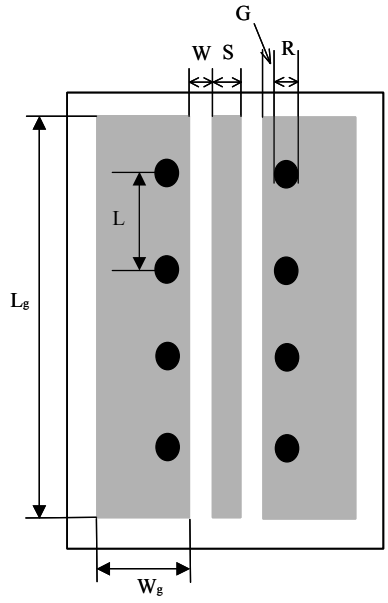

Terms	Symbols	Value
Signal line	S	80 μm
Gap between signal and ground	W	40 μm
Via hole diameter	R	300 μm
Gap between via edge to ground	G	100 μm
Via hole distance	L	800 μm

Fig. 4.2 Fabrication parameters of the conductor-backed coplanar waveguide with via holes.

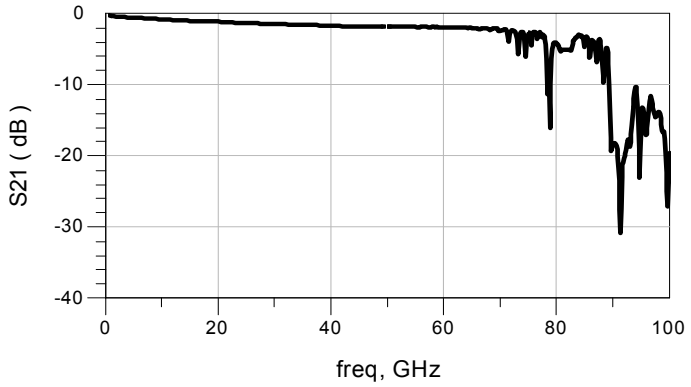

(a)

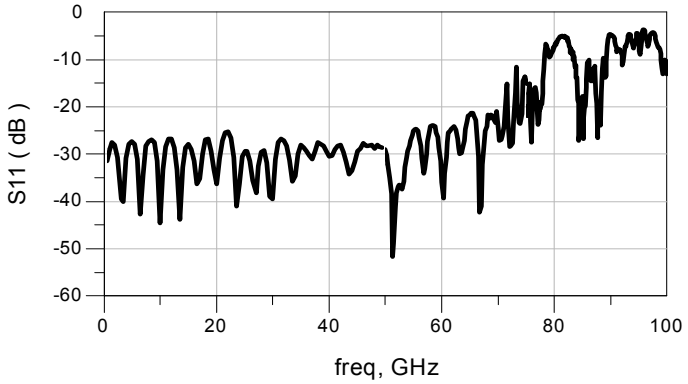

(b)

Fig. 4.3 (a) S_{21} and (b) S_{11} measurement results of the conductor-backed coplanar waveguide with via holes.

The geometrical view of the conductor-backed CPW is shown in Fig. 4.2, and its relevant dimensions are given. On-wafer test is primarily used for its measurement using the network analyzer (HP 8510C). For precise calibration, a SOLT (Short, Open, Load, Thru) method is employed using the impedance standard substrate (ISS). After the calibration, an electrical delay is tuned lifting up the RF probes in the open state. When an exact phase measurement is concerned, the phase delay of the coaxial line and the probes should be excluded. Measurement results are shown in Fig. 4.3. Three separate frequency bands (45 MHz-50 GHz, 50 GHz -75 GHz, and 75 GHz-100 GHz) are measured and their results are depicted altogether. The measurement results show continuous phase and magnitude changes. The fabricated conductor-backed coplanar waveguide shows a 3 dB cutoff frequency of around 72 GHz, and the reflection coefficient is below –20 dB until 71 GHz.

4.1.2. Signal propagation characteristics in the conductor-backed CPW with via holes

In high-speed digital circuit applications, the signal waveform prediction is of significance as the electrical signal propagates a conductor path. As the pulse width of the digital signal reaches the picosecond (or *sub*picosecond) range, the transmission line characteristics such as dispersion and attenuation should be measured with a high precision. In general, they are measured in frequency domain. Therefore, to estimate the signal waveform in time domain we should make a *Fourier* transformation written as,

$$\upsilon(t,z) = \mathscr{F}^{-1}\{V(f,z)\} = \mathscr{F}^{-1}\{V(f,0)\cdot\exp(-(\alpha(f)+\mathrm{j}\beta(f))\cdot z)\} \quad \textbf{(4.4)}$$

where $V(f,z)$ is the Fourier transform of $\upsilon(t,z)$, $\alpha(f)$ is the frequency dependent attenuation coefficient, and $\beta(f)$ is the frequency dependent phase. $\mathscr{F}^{-1}(\cdot)$ denotes an inverse *Fourier* transformation.

The CPW loss is composed of dielectric loss, conductor loss, and radiation loss. Usually, the dielectric loss is much smaller than the conductor loss and negligible [72]. If no leaky wave mode is excited, the conductor loss is dominant source for the attenuation. However, above 200 GHz the radiation loss starts to be dominant [70]. The radiation leakage occurs because of surface waves in the conductor-backed slab waveguide. Therefore, the attenuation coefficients can expressed as the summation of conductor loss and radiation loss by

$$\alpha = \alpha_{cond} + \alpha_{rad} . \quad \textbf{(4.5)}$$

The dispersion problem arises from the frequency-dependent characteristics of the propagation constant associated with physical geometries of the structures, i.e., coplanar waveguides or microstrip lines. The frequency-dependent nature of the signal propagation constants causes signal distortion, in other words, the propagated signal shows the pulse broadening effect. The dispersion characteristic is modeled using the following equation.

$$\beta(f) = \frac{2\pi f}{c}\sqrt{\varepsilon_{eff}} \quad \textbf{(4.6)}$$

where ε_{eff} is the effective dielectric constant and analytic equation is shown below.

$$\varepsilon_{eff}(f)^{1/n} = \sqrt{\varepsilon_q} + \frac{\sqrt{\varepsilon_r} - \sqrt{\varepsilon_q}}{\left(1 + a \cdot \left(\frac{f}{f_{TE1}}\right)^{-1.8}\right)} \tag{4.7}$$

where, $\varepsilon_q = \frac{\varepsilon_r + 1}{2}$, ε_r is the relative dielectric constant of the substrate, n is 2, f_{TE1} is given in (4.1), and a is found using [70],

$$\log(a) = u \cdot \log\left(\frac{W}{S}\right) + \upsilon$$

$$u = 0.54 - 0.69 \cdot \log\left(\frac{W}{h}\right) + 0.015 \cdot \log\left(\frac{W}{h}\right)^2 \tag{4.8}$$

$$\upsilon = 0.43 - 0.86 \cdot \log\left(\frac{W}{h}\right) + 0.540 \cdot \log\left(\frac{W}{h}\right)^2$$

where h is the thickness of the substrate. The calculation for the attenuation and the effective dielectric constant are carried out using the measured S-parameter. The S-parameter response of the *lossy unmatched* transmission line is expressed as [73][74],

$$\begin{bmatrix} S_{11} & S_{12} \\ S_{21} & S_{22} \end{bmatrix} = \frac{1}{D_s} \begin{bmatrix} (Z^2 - Z_o^{\,2}) \sinh \gamma l & 2ZZ_o \\ 2ZZ_o & (Z^2 - Z_o^{\,2}) \sinh \gamma l \end{bmatrix} \tag{4.9}$$

where, $D_s = (Z^2 + Z_o^{\,2}) \sinh \gamma l + 2ZZ_o \cosh \gamma l$. Using the equation (4.9), the following equation can be derived directly,

$$e^{-\gamma l} = \frac{1 - S_{11}^{\,2} + S_{21}^{\,2}}{2S_{21}} \pm \sqrt{\frac{\left(S_{11}^{\,2} - 1 - S_{21}^{\,2}\right)^2 - 4S_{21}^{\,2}}{\left(2S_{21}\right)^2}} \tag{4.10}$$

where $\gamma(f) = \sqrt{(R + j\omega L) \cdot (G + j\omega C)} = \alpha(f) + j\beta(f)$, and we use the symmetry condition for port 1 and port 2, namely, $S_{11} = S_{22}$, and $S_{12} = S_{21}$. The positive sign is used to find the negative direction propagation constant, and the negative sign is for the positive direction.

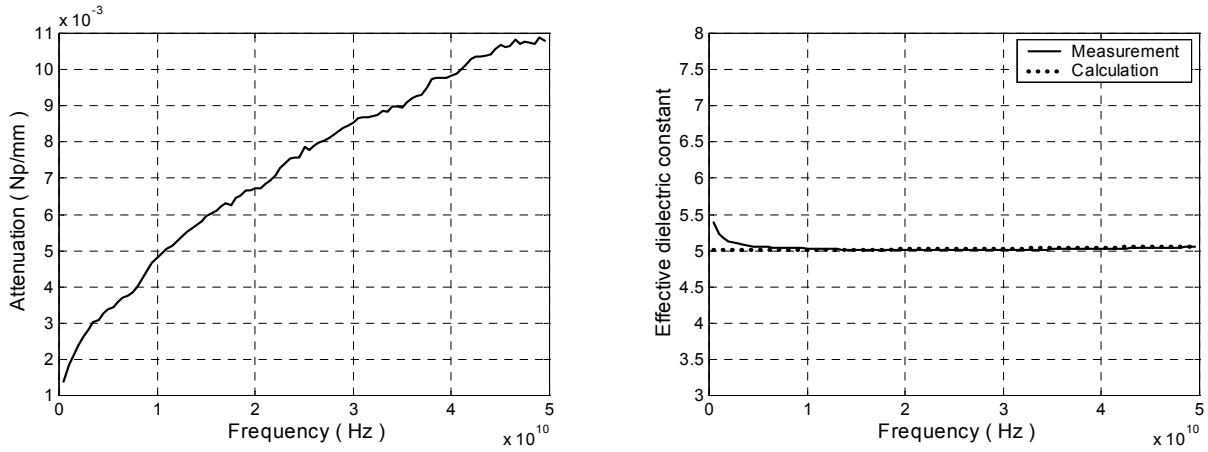

(a) (b)

Fig. 4.4 (a) Measured attenuation constant and (b) Comparison of the measured with the calculated effective dielectric constant, respectively.

The extraction results are shown in Fig. 4.4. The attenuation coefficient is normalized with regard to the length. The length of the CPW we designed is 20 mm. Effective dielectric constant is also extracted and compared with the analytic calculation in (4.7). We change the coefficient *n* into 1.9 in order to fit the extracted data. In fact, the analytic expression is derived for the conductor-backed CPW *without* via holes. Therefore, the *n* value difference is attributed to the discrepancies of the propagation characteristics with via holes. We also investigate the group delay characteristic. The group delay is defined as,

$$T(f) = -\frac{1}{2\pi}\frac{d\Phi(f)}{df}. \qquad \textbf{(4.11)}$$

where $\Phi(f)$ is the phase response of the CPW. The group delay is calculated using the measured S_{21} parameter. We compared the extracted result with the interpolation result as shown in Fig. 4.5. The interpolation is done for the frequency band from 3 GHz to 50 GHz with couples of points. It shows a constant group delay until 23 GHz. At 43 GHz the group velocity deviates from the constant delay line about 6.1 psec. We characterize this relation ship with the following equation,

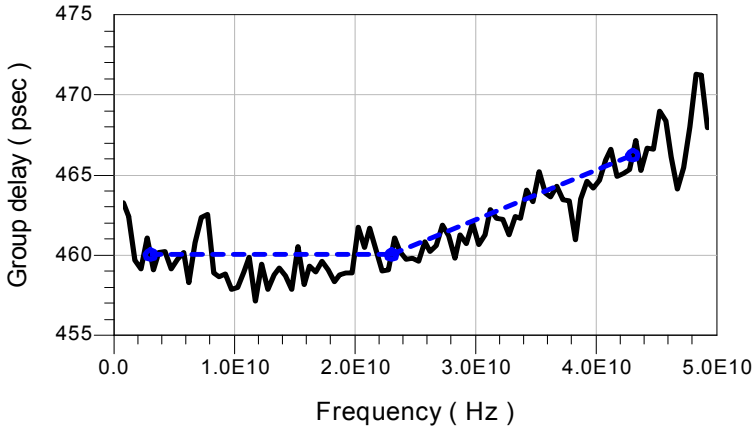

Fig. 4.5 Group delay is extracted from the S_{21} parameter (solid line). Interpolation line is performed for the measurement results (dotted line).

$$\begin{aligned}\Phi(f) &= 2\pi \cdot f \cdot T(f) \\ &\approx 2\pi \cdot f \cdot \left(T_0 + T_1 \cdot \frac{f}{f_0} \right)\end{aligned} \qquad \textbf{(4.12)}$$

where for 43 Gbit/s NRZ signal, $f_0 = 43$ GHz, T_0 is constant value, 460 psec for 20 mm length of the conductor-backed CPW with via holes, and T_1 is 6.1 psec.

Using the above results, i.e., the attenuation coefficient, and the dispersion parameter, we simulate how both of them change the eye waveform for the different propagation lengths. The eye waveform depicts the signal waveforms by overlapping them in limited time window. It clearly shows the signal waveform at specific distance. In Fig. 4.6(a) the input signal to the designed conductor-backed CPW line is shown. This is equivalent to the Fig. 3.20(b). For 4 cm and 8 cm long length, the simulation results are presented in Fig. 4.6(a) and (b), respectively. As the propagation is increased, the distortion and the signal amplitude attenuation are clearly shown.

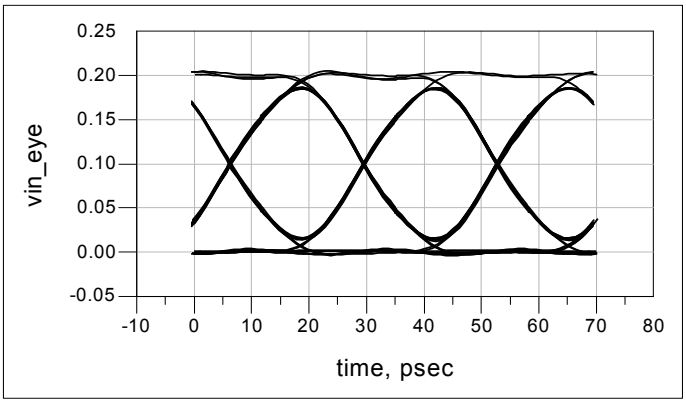

(a)

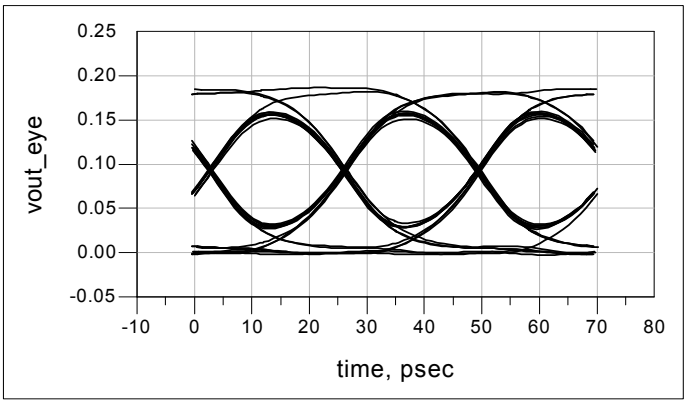

(b)

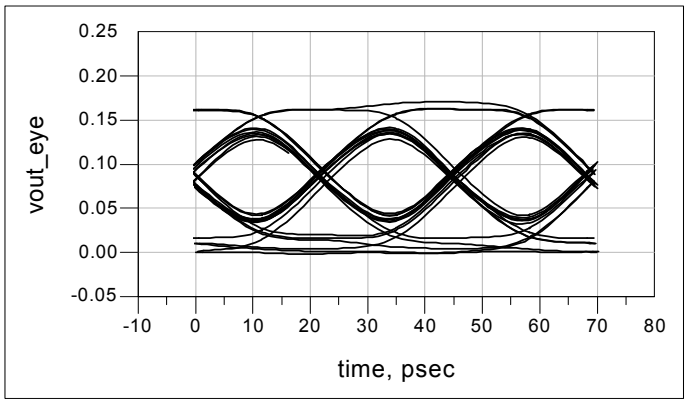

(c)

Fig. 4.6 (a) Eye diagram of the 43 Gbit/s at the input after 5th order Bessel filter. Eye opening are observed for (b) 4cm and (c) 8cm long conductor-backed CPW lines

4.2. Resistive power divider circuit design and measurement

A resistive power divider divides an input signal into two having a 6 dB insertion loss. Therefore, the divided signal amplitude is halved. Once each port is terminated with Z_0 (50 Ω) in Fig. 4.7(a), the input impedance shows a matched condition written by,

$$Z_{in} = \frac{Z_0}{3} + \frac{4Z_0}{3} \| \frac{4Z_0}{3} = Z_0 \qquad \textbf{(4.13)}$$

If the input voltage to the input is V, then the output voltage at port 2 and 3 is found as,

$$V_{out} = V \cdot \frac{2Z_0/3}{Z_0/3 + 2Z_0/3} \cdot \frac{Z_0}{Z_0/3 + Z_0} = \frac{1}{2}V \,. \qquad \textbf{(4.14)}$$

If this network is symmetric, then the 3 port S-parameter matrix is given by

$$\begin{bmatrix} S_{11} & S_{12} & S_{13} \\ S_{21} & S_{22} & S_{23} \\ S_{31} & S_{32} & S_{33} \end{bmatrix} = \frac{1}{2}\begin{bmatrix} 0 & 1 & 1 \\ 1 & 0 & 1 \\ 1 & 1 & 0 \end{bmatrix}. \qquad \textbf{(4.15)}$$

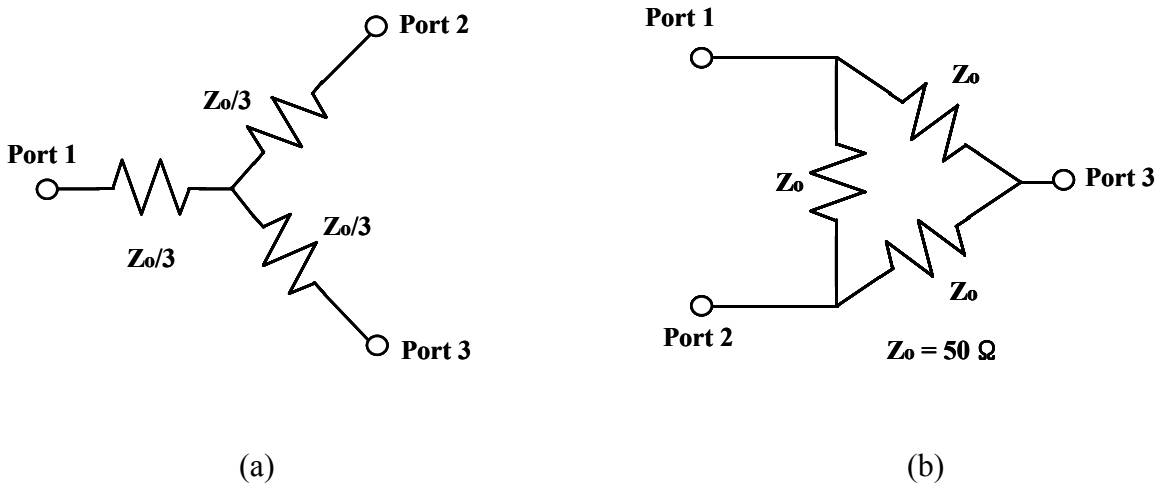

(a) (b)

Fig. 4.7 Resistive power divider configuration (a) Star configuration (Z_o=16.67 Ω) (b) Delta configuration (Z_o = 50 Ω)

The resistive power divider can be implemented using the two configurations. One is a star configuration, named after its position of the resistance 16.67 Ω (Fig. 4.7(a)), and the other is a delta configuration (Fig. 4.7(b)). In fact, the larger resistance value is employed, the better performance shall be acquired because of the fabrication tolerance. Using the Y-Δ transformation equations according to Fig. 4.8, the *star* configuration is converted into the delta configuration. The delta configuration is preferred in the hybrid implementation due to the magnitude of the resistance value.

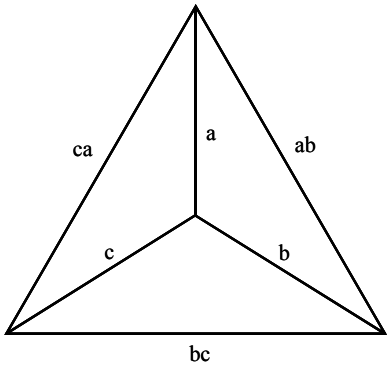

$$Z_a = \frac{Z_{ab} \cdot Z_{ca}}{Z_{ab} + Z_{bc} + Z_{ca}}$$

$$Z_{ab} = Z_a + Z_b + \frac{Z_a \cdot Z_b}{Z_c}$$

Fig. 4.8 Y-Δ transformation diagram [75].

In Fig. 4.9(a), the actual layout is illustrated. Both the *star* and the *delta* configurations are utilized for the implementation. Fig. 4.9(a) illustrates the *delta* configuration layout. The designed conductor-backed CPWs are used for the resistive power divider implementation. The sheet resistance is 100 Ω/□. *Anritsu* integrated V connector (model V115FCPW) is employed for the transition. This connector includes the solder-in CPW line with a ground-lip in the structure. The frequency range is from DC to 65 GHz [76].

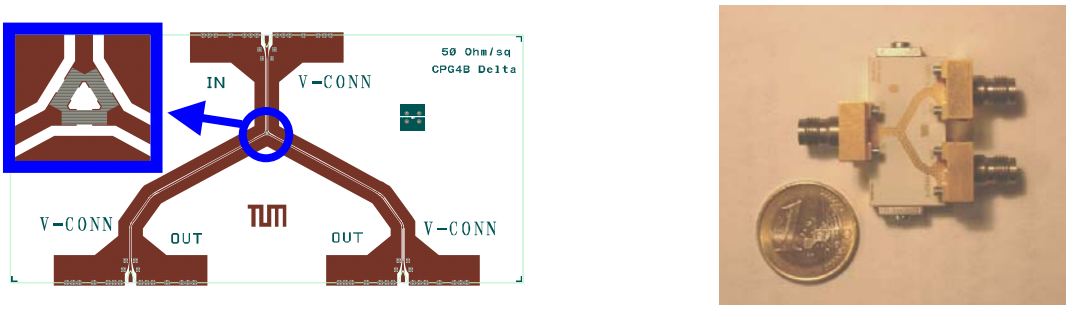

(a) (b)

Fig. 4.9 (a) Resistive power divider circuit layout, and (b) fabrication module.

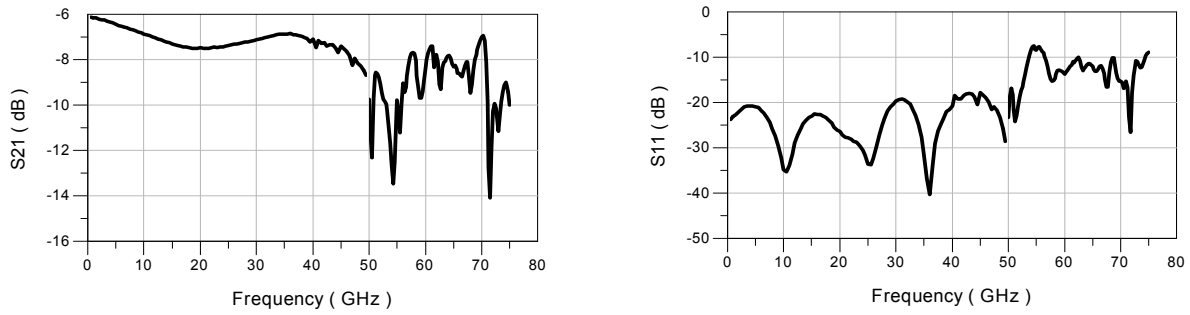

(a) (b)

Fig. 4.10 Resistive power divider (delta configuration) on-wafer measurement results for (a) S_{21} and (b) S_{11}.

First of all, on-wafer measurement is performed for the delta configuration. For the measurement purpose, 50 Ω on-chip is intentionally added to the port 3 for the two port network measurement system and drawn in the layout. Two separate frequency bands are measured separately: 45 MHz-49.5 GHZ and 50 GHz-75 GHz. A slight discontinuity around at 50 GHz is due to the measurement frequency discontinuity from 49.5 GHz to 50 GHz. Two measurement results are merged and depicted in Fig. 4.10, altogether. The 3 dB cutoff frequency is about 50 GHz. Up to 50 GHz, S_{11} shows below –20 dB. The star configuration is also fabricated and measured for the same frequency bands. Even though the small resistance value (16.67 Ω) in the star configuration is fabricated, the measurement results are very similar to the delta configuration's. We test the fabricated module using the transient 43 Gbit/s *nonreturn-to-zero* (NRZ) signal and 86 Gbit/s return-to-zero (RZ) signal. The module includes the V type connector shown in Fig. 4.9(b). In Fig. 4.12, the eye diagram measurement results are shown. Due to the 6 dB insertion loss characteristic of the resistive power divider circuit, the output amplitude is reduced by half. For the 43 Gbit/s electrical signal, the output eye waveform of the divider looks good for the following sampling circuit applications (Fig. 4.12(b)). The output amplitude is exactly halved as 100 mV_{pp}. For the 86 Gbit/s RZ signal measurement, the output signal from the photodiode having a bandwidth of 55 GHz is measured and shown in Fig. 4.12(a). For the 86 Gbit/s RZ signal case, eye opening is observed even though the opening is considerably reduced. This might be due to insufficient bandwidth characteristic and the capacitive nature of the transition in the V-connectors. Nevertheless, up to 86 Gbit/s electrical signal applications, this resistive power divider circuit might be applicable for the circuit demonstration purposes.

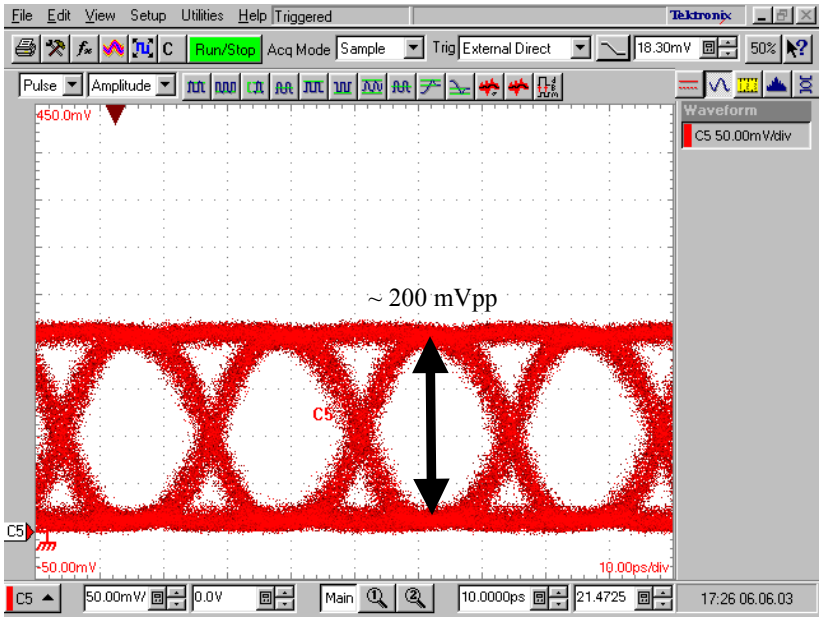

(a)

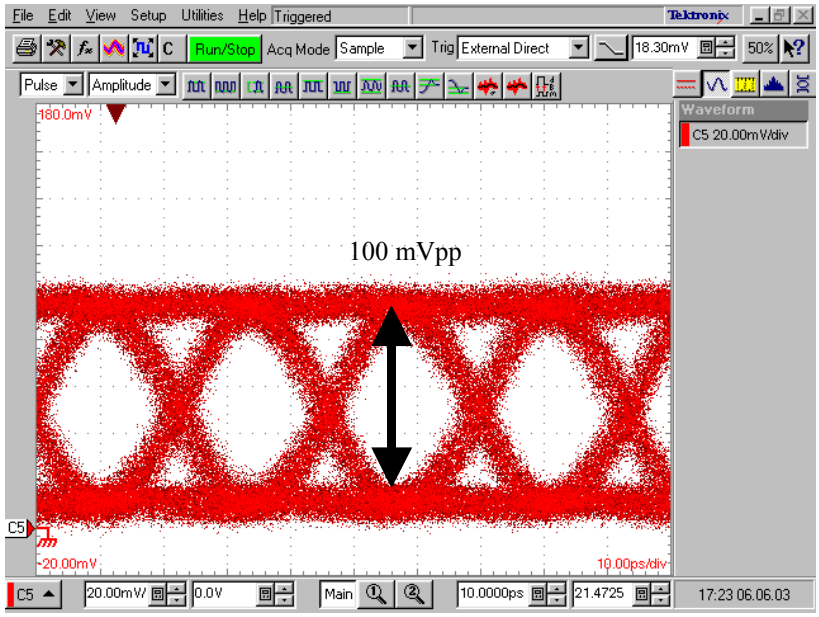

(b)

Fig. 4.11 Eye diagrams for (a) 43 Gbit/s NRZ input signal and (b) the resistive power divider output.

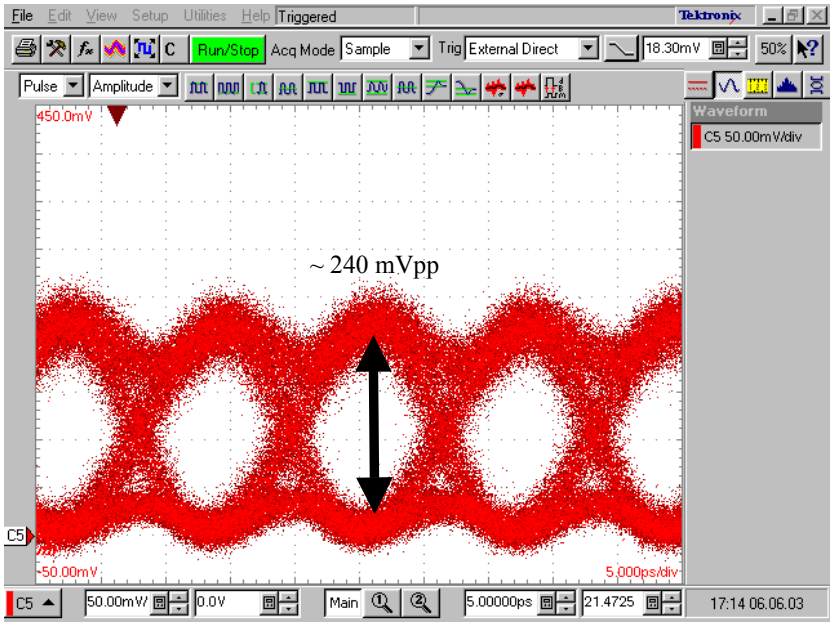

(a)

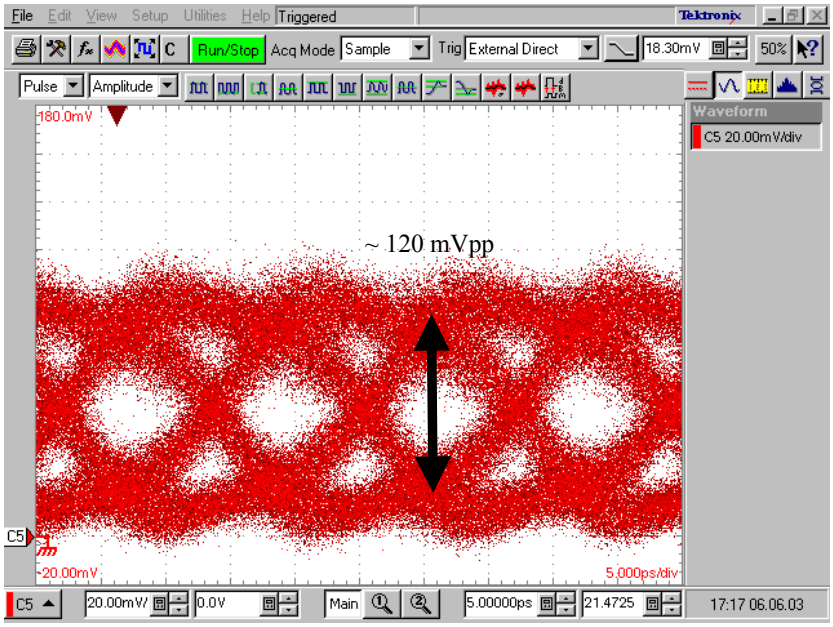

(b)

Fig. 4.12 Eye diagrams for (a) 86 Gbit/s RZ input signal and (b) the resistive power divider output.

4.3. Sampling circuit measurement

Using the developed Root-diode model and the flip-chip equivalent circuit, the 43 Gbit/s sampling circuit using Si Schottky diodes is successfully designed, and fabricated employing the hybrid technology. Diodes are flip-chip bonded at 300 °C. Fig. 4.13 shows the fabricated sampling circuit module (5.3 cm x 4.5 cm). Four K-connectors are assembled with metal block, and attached to the gold-plated metal block.

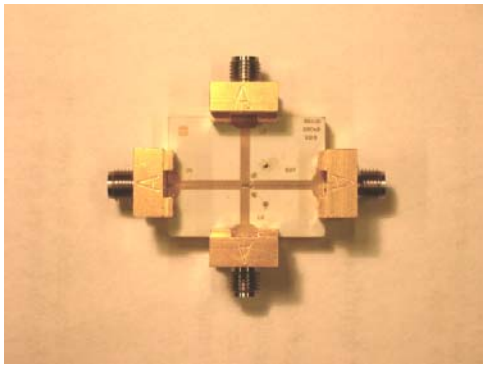

Fig. 4.13 The fabricated 43 Gbit/s sampling circuit module. Flip-chip bondings are done under 300 °C temperature condition.

Fig. 4.14 depicts the full measurement set-up including all exterior passive and active components used in the measurement. An *Anritsu* pulse pattern generator (MP1763B) and a 43 Gbit/s multiplexer made at Siemens are used to generate 43 Gbit/s pseudo random binary sequence (PRBS) pattern. The pulse-pattern generator has two data output ports. The output data signals are 10.617 Gbit/s NRZ signal with an amplitude of 1 V_{pp}. Two clock output signals in the pulse pattern generator are used for frequency tuning in frequency monitor (Anritsu MP1764B) and transient pattern synchronization for a digital sampling oscilloscope (Tektronix 8000). We use the bit error rate tester (Anritsu MP1764B) as a frequency monitor. The 43 Gbit/s multiplexer multiplexes two data signal into 42.468 Gbit/s NRZ signal in time domain using two clock signals. One clock is from the pulse pattern generator and another is from a signal generator (Agilent 83630B), which generates a 21.234 GHz clock signal with 10 dBm power (2 V_{pp}). The multiplexed signal is measured using the digital sampling oscilloscope, which has a trigger signal level of 190 ± 10 mV_{pp}. It is around 700 mV_{pp} at 42.468 Gbit/s as shown in Fig. 4.15.

The output waveforms of the sampling circuit are measured using Tektronix 8000, and illustrated in Fig. 4.16. In order to synchronize the input signal with the oscillator signal, two variable delay lines are attached to the oscillator input port of the sampling circuit. The oscillator signal is kept to be constant around 2 dBm. Two output results are obtained varying the oscillator signal phase by 180 degrees. Thus, they correspond to channel 1, and channel 2 output signal, respectively, or vice versa. Around 17 dB insertion loss is measured.

Setting up the threshold line, the bit information can be obtained simply comparing the threshold with the measured data output. The arrows in Fig. 4.16 display sampling instants with an interval of 47.1 psec. We compare the measurement results (Fig. 4.16) with the simulation results having the same bit pattern (Fig. 4.17). The output voltage ringing phenomena is observed. They are attributed to the capacitive behavior of the connector, and the interactions between the chips. In addition, as demonstrated in the simulation part, that is due to the bit pattern dependency of the output waveform. This ringing phenomenon might be considerably reduced using the proposed transversal filter, and will be demonstrated in experiments.

Comparing the output voltage amplitude, the decision level for logic ‘1’ and ‘0’ can be decided. Both channels (see Fig. 4.16) have the same threshold level at ground. The decision point, namely eye opening maximum point, can be evaluated after processing the signal using the proposed linear transversal filter.

Up to now, the sampling of the multiplexed data signal is performed using the flip-chip bonded Si Schottky diode sampling circuit. The measurement results of the sampling circuit shows a relative amplitude difference depending on the data bits, ‘1’ or ‘0’. The threshold voltage is chosen in order to determine the bit information. It should be noted that the MMIC implementation of the sampling circuit using Si Schottky diodes will lead to better performance with less parasitic interactions. A compact integration with the linear equalizer results in an ultimate demultiplexer performance.

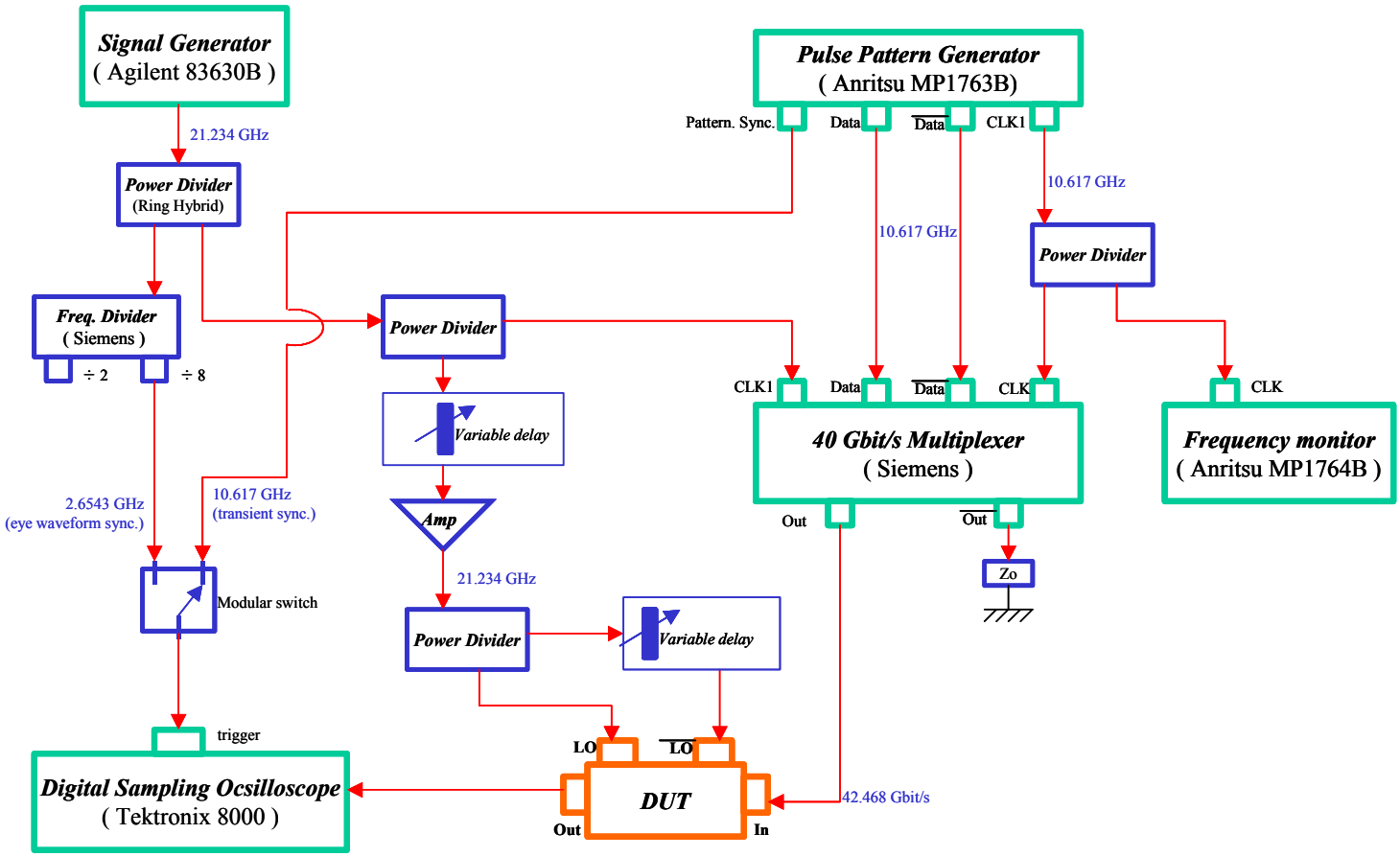

Fig. 4.14 Sampling circuit measurement set-up.

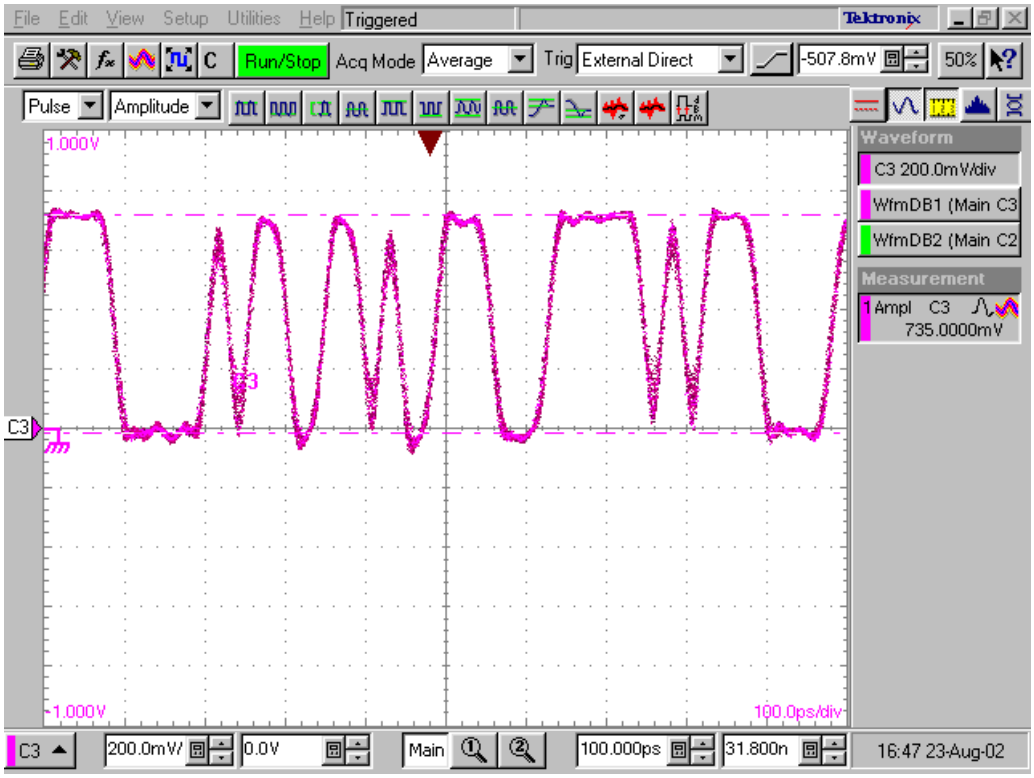

Fig. 4.15 42.468 Gbit/s NRZ signal source generated in 43 Gbit/s ETDM multiplexer.

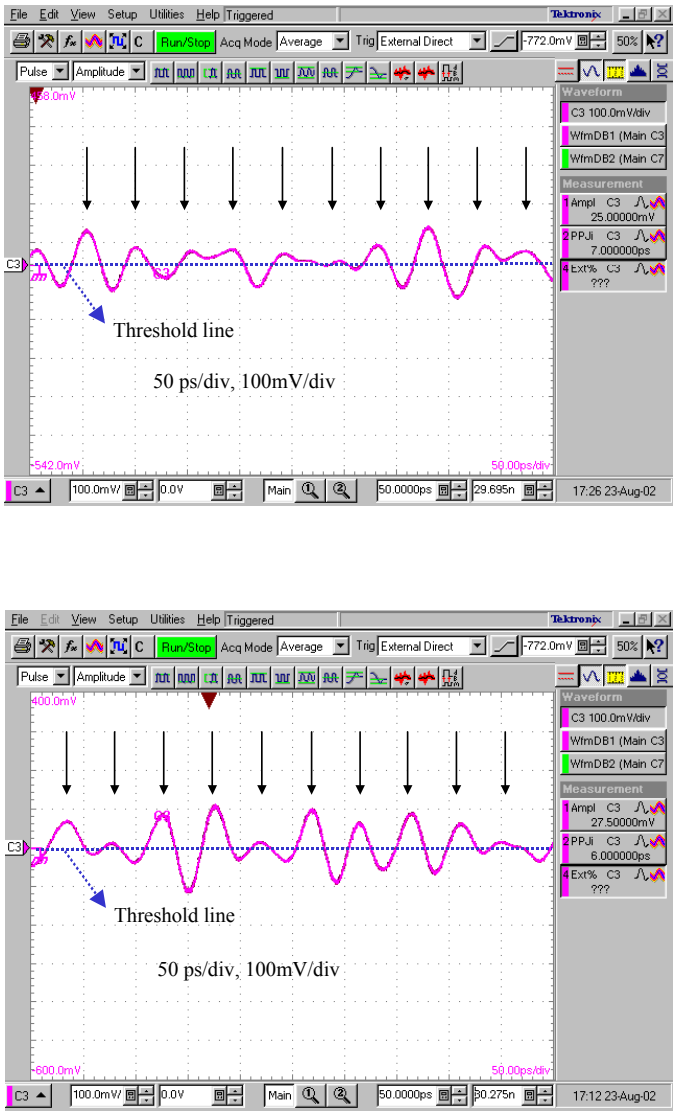

Fig. 4.16 The measured output waveform. The arrows indicate the sampling instant.

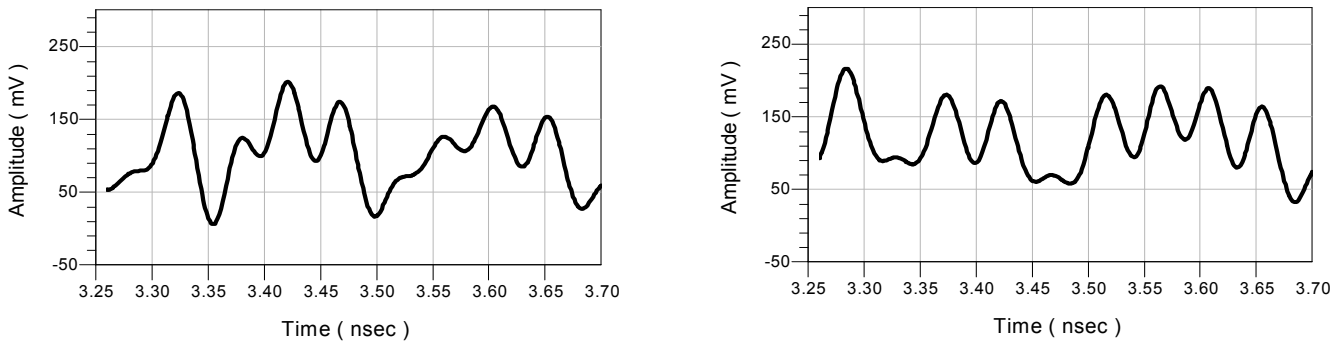

Fig. 4.17 Simulation is performed using the same input bit patterns in Fig. 4.16.

Chapter 5 Conclusion and outlook

For a high-speed demultiplexer circuit implementation, we proposed and demonstrated a sampling circuit combining with a linear equalizer. For the circuit demonstration, we carried out the *Root-diode* modeling. This diode model is suitable for the accurate performance prediction of Si Schottky diodes in high frequency operation. It is a *nonquasi-static* and a *charge-conservative* model. The developed Root-diode model showed a good agreement with the measurement data for both DC and CV. This characteristic is well suited for the sampling circuit simulation since the large and the small-signal analysis are needed in the simulation.

For hybrid implementations, we have carried out the simulation of the *flip-chip* interconnection using a full wave electromagnetic simulator. We established an equivalent circuit model and obtained discrete model components value by interpolating simulation results. In order to verify the equivalent circuit model, we simulated, fabricated, and measured the flip-chip bonded Si Schottky diode on the alumina substrate employing the developed Root-diode model and the flip-chip bonding equivalent circuit. A good agreement has been found between the simulation result and the measurement up to 50 GHz.

Then, the sampling circuit was designed, and simulated for the realization of the demultiplexer circuit. We used the Root-diode model and the flip-chip equivalent circuit. Both hybrid and *monolithic microwave IC* (MMIC) implementations were considered in the circuit simulation for the 43 Gbit/s demultiplexer circuit. We compared the impulse responses and investigated the eye diagrams for two cases. We successfully designed the sampling circuit based on the Si Schottky diodes for the 43 Gbit/s 1:2 demultiplexer circuit operation. In order to eliminate the deterministic intersymbol interference (ISI), we proposed a linear equalizer circuit. Using a zero-forcing algorithm, we calculated the tap coefficient analytically and simulated the eye waveform combining with the equalizer circuit. We have identified the eye opening enhancement in the simulation.

For the circuit fabrication, first of all, we designed a conductor-backed CPW with via holes. The cutoff frequency of 72 GHz was obtained. It was analyzed in terms of the losses and the dispersion analytically. We simulated how these two affect signal waveform as the propagation length increases. The resistive power divider was also designed employing the designed CPW with via holes. It was measured under on-wafer condition, and about 50 GHz

bandwidth was acquired. We tested the resistive power divider module employing the 43 Gbit/s NRZ and 86 Gbit/s RZ electrical signal. The 6 dB insertion loss was observed and a good eye opening was maintained for both signal schemes.

We measured the fabricated sampling module. The experimental set-up was illustrated in detail. A 42.468 Gbit/s NRZ signal is synchronized with the oscillator signal. The measured output signal was obtained in time domain and showed a ringing phenomenon. It was attributed to the connector parasitics and the chip interactions. After choosing a threshold level, we could decide the bit information ('1' or '0'). Improvements should be made to achieve a good eye waveform. When the circuit would be made in a MMIC chip, it is expected that the chip shows a better performance. Furthermore, the linear equalizer also should be tested. Tap coefficients might be decided experimentally and compared with the theoretical value. Those works are remained as future works.

The proposed sampling circuit based demultiplexer circuit with a linear equalizer circuit is a significant step toward 160 Gbit/s Si based optical receiver circuit implementation. In this work, we successfully designed the demultiplexer circuit using only Si Schottky diodes. This approach contrasts to the conventional one in that we pursue Si Schottky diodes for the demultiplexer circuit implementation. Our primary intention behind this work is to integrate this demultiplexer circuit with the push-push oscillator circuit, and complete the optical receiver circuit using Si technologies. A push-push oscillator is also built up with Si *heterojunction biploar transistors* (HBTs), which is the only three terminal devices in the whole receiver circuit and has been reported in [13]. Considering the fact that the Si Schottky diodes have achieved over 1 THz cutoff frequency and the the reported push-push oscillator is feasible to be integrated with the sampling circuit for the demultiplexer circuit, we can conclude that the high-speed optical receiver circuit up to 160 Gbit/s will be constructed in silicon monolithic millimeter-wave integrated circuits (SIMMWICs).

Appendix A

Photocurrent and noise statistics

In [39] and [47], it is shown that the photocurrent variance is calculated using the *semiclassical* theory of the photoelectric detection of light. This approach enables the photodetector's impulse response to be associated with the theory of the detection of the light. Here we will explain the detailed derivation processes of the photocurrent autocovariance using the *Gaussian* nature of the noise.

First of all, we pursue for the autocorrelation function of the photocurrent. From the equation (2.40),

$$\left\langle i_{PD}(t)\cdot i_{PD}(t')\right\rangle = \left\langle \sum_{k=-\infty}^{\infty}\sum_{l=-\infty}^{\infty} X(k\Delta t)h(t-k\Delta t)\cdot X(l\Delta t)h(t-l\Delta t)\right\rangle$$

$$= \left\langle \sum_{k=-\infty}^{\infty} X(k\Delta t)X(k\Delta t)h(t-k\Delta t)h(t-k\Delta t)\right\rangle + \left\langle \sum_{k=-\infty}^{\infty}\sum_{\substack{l=-\infty \\ k\neq l}}^{\infty} X(k\Delta t)X(l\Delta t)h(t-k\Delta t)h(t-l\Delta t)\right\rangle$$

[A.1]

We identify that $X^2 = X$ since $X \in \{1, 0\}$. Taking a limit as $\Delta t \to 0$ and using (2.39), (2.41) and (2.44), we can simplify the equation [A.1] as,

$$\left\langle i_{PD}(t)\cdot i_{PD}(t')\right\rangle = \lim_{\Delta t\to 0}\sum_{k=-\infty}^{\infty}\left\langle X(k\Delta t)\right\rangle h^2(t-k\Delta t) + \lim_{\Delta t\to 0}\sum_{k=-\infty}^{\infty}\sum_{\substack{l=-\infty \\ k\neq l}}^{\infty}\left\langle X(k\Delta t)X(l\Delta t)\right\rangle h(t-k\Delta t)h(t-l\Delta t)$$

.

$$= \int_{-\infty}^{\infty}\left\langle \lambda(\tau)\right\rangle h^2(t-\tau)d\tau + \int_{-\infty}^{\infty}\int_{-\infty}^{\infty}\left\langle \lambda(\tau)\lambda(\tau')\right\rangle \cdot h(t-\tau)h(t-\tau')d\tau d\tau'$$

[A.2]

Next, performing the product of the two ensemble averages we also get the equation given by,

$$\begin{aligned}\langle i_{PD}(t)\rangle\langle i_{PD}(t')\rangle &= \big(\langle\lambda(t)\rangle * h(t)\big)\cdot\big(\langle\lambda(t')\rangle * h(t')\big) \\ &= \int_{-\infty}^{\infty}\int_{-\infty}^{\infty}\langle\lambda(\tau)\rangle\langle\lambda(\tau')\rangle h(t-\tau)h(t-\tau')d\tau d\tau'\end{aligned} \qquad \textbf{[A.3]}$$

Therefore, we conclude that the autocovariance of the photocurrent is written as,

$$C_{\Delta i}(t,t') = \langle\lambda(t)\rangle * h^2(t) + \int_{-\infty}^{\infty}\int_{-\infty}^{\infty}\big(\langle\lambda(\tau)\lambda(\tau')\rangle - \langle\lambda(\tau)\rangle\langle\lambda(\tau')\rangle\big)\cdot h(t-\tau)h(t-\tau')d\tau d\tau' \qquad \textbf{[A.4]}$$

From now on, we associate the photoelectron generation rate with the complex optical field intensity. Then, we will calculate the variance component with respect to the optical field. From (2.51), (2.52) and (2.53),

$$\begin{aligned}\langle\lambda(t)\rangle * h^2(t) &= R\cdot q\Big(\big\langle|\mathbf{O_{RX}(t)}|^2\big\rangle * h^2{}_{PD}(t)\Big) \\ &= R\cdot q\Big(\big\langle|O_{SIG}(t)|^2 + |\mathbf{O_N(t)}|^2 + 2\Re\big(O_{SIG}(t)\mathbf{O_N}^*\mathbf{(t)}\big)\big\rangle * h^2{}_{PD}(t)\Big) \\ &= R\cdot q\big(p_{SIG}(t) + P_N\big) * h^2{}_{PD}(t)\end{aligned} \qquad \textbf{[A.5]}$$

where we assume that the signal field and the noise are uncorrelated, the zero-mean Gaussian noise characteristic, and $P_N = S_{ASE}(\nu)\cdot B_O = n_{sp}^{\ eff}(\nu)(G(\nu)-1)\cdot h\nu\cdot B_O$ is the average ASE noise power with the optical filter bandwidth, B_O. Here it is noted that using the semiclassical theory of the photoelectron detection of the light we express the ensemble average of the photocurrent incorporating with the PD's impulse response.

The autocovariance of the photoelectron generation rate is expressed using the complex optical field written by,

$$\langle\lambda(\tau)\lambda(\tau')\rangle - \langle\lambda(\tau)\rangle\langle\lambda(\tau')\rangle = \left(\frac{R}{q}\right)^2\Big\langle|\mathbf{O_{RX}(\tau)}|^2|\mathbf{O_{RX}(\tau')}|^2\Big\rangle - \Big\langle|\mathbf{O_{RX}(\tau)}|^2\Big\rangle\Big\langle|\mathbf{O_{RX}(\tau')}|^2\Big\rangle \qquad \textbf{[A.6]}$$

Here we apply the *Gaussian moment theorem* to the ASE Gaussian noise calculation. If $x_1, x_2, \ldots$ are Gaussian variates, the Gaussian moment theorem states [39],

$$\left\langle z_1 z_2 z_3 z_4 \cdots z_m \right\rangle = \begin{cases} 0 & \text{if m is odd} \\ \sum_{\text{all } (m-1)! \text{ pairings}} \left\langle z_1 z_2 \right\rangle \left\langle z_3 z_4 \right\rangle \cdots \left\langle z_{(m-1)} z_m \right\rangle & \text{if m is even} \cdot \end{cases} \quad \textbf{[A.7]}$$

Then, the variance derivation process is straightforward. Using the following equation,

$$\left\langle \left|\mathbf{O}_N(\boldsymbol{\tau})\right|^2 \left|\mathbf{O}_N(\boldsymbol{\tau}')\right|^2 \right\rangle = \left\langle \mathbf{O}^*{}_N(\boldsymbol{\tau})\mathbf{O}_N(\boldsymbol{\tau}) \right\rangle \left\langle \mathbf{O}^*{}_N(\boldsymbol{\tau}')\mathbf{O}_N(\boldsymbol{\tau}') \right\rangle + \left\langle \mathbf{O}^*{}_N(\boldsymbol{\tau})\mathbf{O}_N(\boldsymbol{\tau}') \right\rangle \left\langle \mathbf{O}^*{}_N(\boldsymbol{\tau}')\mathbf{O}_N(\boldsymbol{\tau}) \right\rangle \quad \textbf{[A.8]}$$

the autocovariance equation reduces to

$$C_{\mathbf{O_{RX}}}(\tau,\tau') = 2\Re\left\{ O_{SIG}(\tau) O_{SIG}(\tau') \left\langle \mathbf{O}^*{}_N(\boldsymbol{\tau})\mathbf{O}_N(\boldsymbol{\tau}') \right\rangle \right\} + \left| \left\langle \mathbf{O}^*{}_N(\boldsymbol{\tau})\mathbf{O}_N(\boldsymbol{\tau}') \right\rangle \right|^2 \quad \textbf{[A.9]}$$

Substituting [A.4] with [A.5] and [A.9], we finally acquire the expression for the autocovariance of the photocurrent.

$$\begin{aligned} C_{\Delta i}(t,t') &= \left\langle \Delta i(t) \cdot \Delta i(t') \right\rangle = \left\langle i(t) i(t') \right\rangle - \left\langle i(t) \right\rangle \left\langle i(t') \right\rangle \\ &= R\left(\left\langle \left|\mathbf{O_{RX}}(t)\right|^2 \right\rangle * {h_{PD}}^2(t) \right) + R^2 \int_{-\infty}^{\infty}\int_{-\infty}^{\infty} C_{\mathbf{O_{RX}}}(\tau,\tau') h_{PD}(t-\tau) h_{PD}(t-\tau') d\tau d\tau' \\ &= R \cdot q({p_{SIG}}(t) * {h_{PD}}^2(t)) + R \cdot q(P_N * {h_{PD}}^2(t)) \\ &\quad + 2R^2 \cdot \Re\left\{ \int_{-\infty}^{\infty}\int_{-\infty}^{\infty} O_{SIG}(\tau) O_{SIG}(\tau') \left\langle \mathbf{O_N}^*(\tau)\mathbf{O_N}(\tau') \right\rangle h_{PD}(t-\tau) h_{PD}(t-\tau') d\tau \cdot d\tau' \right\} \\ &\quad + R^2 \cdot \int_{-\infty}^{\infty}\int_{-\infty}^{\infty} \left| \left\langle \mathbf{O_N}^*(\tau)\mathbf{O_N}(\tau') \right\rangle \right|^2 h_{PD}(t-\tau) h_{PD}(t-\tau') d\tau \cdot d\tau' \end{aligned} \quad \textbf{[A.10]}$$

Appendix B

Si Schottky diode demultiplexer circuit *MATLAB* program

```
%-----------------------------------------------------------------------%
% Author : Jung Han Choi
% Parameter definitions
%-----------------------------------------------------------------------%
% Nyquist wavefrom Roll-off factor. Ref : IEEE Journal of Light. Tech. Vol.19, No. 9, pp. 1263-1273, Sep. 2001.
alpha=0.4;

% td : pulse width
%         40 Gbps NRZ : td=25.00e-12 sec,          80 Gbps RZ  : td= 6.25e-12 sec
td=6.25e-12;

% Number of periods in the Nyquist waveform
num_period=1;

% Number of points in one period of waveform
pts=100 ;

%-----------------------------------------------------------------------%
% Simulation range definition in time domain.
%         start and stop points should be integer times of period
%         e.g.) start_time=0,stop_time=100 means that simulation time is
%                 from 0(sec) to 100*td   ( sec ) ( 0 ~ 100T ) for NRZ signal
%                 from 0(sec) to 100*td*2 ( sec ) ( 0 ~ 100T ) for  RZ signal
%-----------------------------------------------------------------------%
start_time=0; stop_time=30;

%-----------------------------------------------------------------------%
% Random input signal generation combining with Nyquist waveform and pseudo-random binary sequence ( PRBS )
%-----------------------------------------------------------------------%
e=[]; e=input_signal(td, alpha, pts, num_period, start_time, stop_time);

%-----------------------------------------------------------------------%
% 5th order Bessel-Thompson filter . Input_signal passes through the filter. We depict eye diagram after the filter.
%-----------------------------------------------------------------------%
num=[0 0 0 0 0 945]; den=[1 15 105 420 945 945];
[A B C D]=tf2ss(num,den); % Converts into the state-sapce domain
[G H]=c2d(A, B, 0.01375); % 55GHz / 8000GHz ( 80G NRZ ) *2
% 8000GHz : sampling frequency. One period of 80 Gbit/s RZ signal ( 2*6.25psec ) is subdivided by 'pts'.
% Thus,sampling time difference is 2*6.25psec / 100 pts, which corresponds to 8000 GHz.

[numz denz]=ss2tf(G,H,C,D); y=filter(numz, denz, e);
eye_waveform(y, td, pts, 0);  % Draw eye diagram
```

```
%-------------------------------------------------------------------%
% Sampling process ( demultiplexing )
%-------------------------------------------------------------------%
figure;x=start_time:1/pts:stop_time; subplot(5,1,1); plot(x,y);  % Plot PRBS Nyquist waveform after Bessel filter

subplot(5,1,2);
% Generate impulse train for channel 1 and draw it
imp_sampler_ch1=transfer_sampler(2*td, 2*pts, start_time, stop_time, 6.25e-12);
% Perform sampling ( demultiplexing ) for channel 1
output_sampling_ch1=sampling(y, imp_sampler_ch1);

subplot(5,1,3);
% Generate impulse train for channel 2 and draw it
imp_sampler_ch2=transfer_sampler(2*td, 2*pts, start_time, stop_time, 12.5e-12);
% Perform sampling ( demultiplexing ) for channel 1
output_sampling_ch2=sampling(y, imp_sampler_ch2);

% Depict the sampled waveform in time domain for channel 1 and 2
subplot(5,1,4); plot(x,output_sampling_ch1);
subplot(5,1,5); plot(x,output_sampling_ch2);

%-------------------------------------------------------------------%
% The sampled signal passes through a low-pass filter ( LPF ) to make its demultiplexed waveform.
%-------------------------------------------------------------------%
[G H]=c2d(A, B, 0.005); % 20 GHz /8000GHz ( 40G NRZ ) *2
[numz denz]=ss2tf(G,H,C,D);
% Sampled signal ( channel 1 ) is filter out by the 5th order Bessel filter
% which has a bandwidth of 20GHz.
yy=filter(numz, denz, output_sampling_ch1');
% Draw eye diagram
eye_waveform(yy, td, pts, 0);
```

----------SUBROUTINE 1----------

```
%-------------------------------------------------------------------%
% Signal modeling
%   Function usage : input_signal(td, alpha, pts, num_period, start_time, stop_time)
%
%   This function generates PRBS waveform in time domain.
%   The pulse used here is Nyquist waveform with roll-off factor, 0<alpha<1.
%
%       1. Pulse width                      : td
%       2. Nyquist coefficient              : alpha
%       3. # of points in one pulse duration    : pts
%       4. # of periods in Nyquist waveform : num_period
%       5. start time point                 : start_time
%       6. stop time                        : stop_time
%-------------------------------------------------------------------%

function e=input_signal(td, alpha, pts, num_period, start_time, stop_time)

% Nyquist waveform generation with Roll-off factor and pts.
pulse=Nyquist_pulse(alpha,pts,num_period);

% PRBS sequence 2^8-1 generation (Subroutine PRBS_seq)
PRBS_sequence=PRBS_seq(8);

% input signal matrix initialization
e([1:(stop_time)*pts+1],:)=0;
```

```
% 80 Gbps RZ case
for i=start_time:stop_time+num_period-1,
  if(-i<-num_period)        p_start=-num_period; else p_start=-i;       end;
  if(i+num_period)>stop_time p_stop=stop_time-i;  else p_stop=num_period;end;

  temp_pulse=pulse([(p_start+num_period)*pts+1:(p_stop+num_period)*pts+1],:);
  if(i<=num_period)                    index=0;                          else index=i-num_period;end;
  temp_index=0;
  for k=index*pts+1:index*pts+size(temp_pulse,1),
    temp_index=temp_index+1;
    e(k,:)=e(k,:)+temp_pulse(temp_index)*PRBS_sequence(i+1);
  end
end
```

----------SUBROUTINE 2----------

```
%-----------------------------------------------------------------------%
% PRBS (Pseudo-random Binary Sequence) generator Program
% PRBS(num_stage)
%               PRBS() generate PN sequences with user-defined recurrence relation.
%               num_register ; # of shift register in Linear Feedback Shift Register(LFSR)
%               Note that Student version of MATLAB supports not more than 14 shift registers.
%-----------------------------------------------------------------------%
function p=PRBS_seq(num_register)

if (num_register<2|num_register>33)
  error('Num_register represents the number of shift register in Linear Feedback Shift Register');
  error('num_register should be larger than 2, or smaller than 33 in this version');
end

% Tap reference
ref_tap=[2 1 0 0;3 1 0 0;4 1 0 0;5 2 0 0;6 1 0 0;7 1 0 0;8 4 3 2;9 4 0 0;10 3 0 0;11 1 0 0;12 6 4 1;
  13 4 3 1;14 12 2 1;15 13 10 9;16 12 3 1;17 3 0 0;18 7 0 0;19 5 2 1;20 3 0 0;21 2 0 0;22 1 0 0;
  23 5 0 0;24 7 2 0;25 3 0 0;26 6 2 1;27 5 2 1;28 3 0 0;29 2 0 0;30 23 2 1;31 29 21 17;32 22 2 1;
  33 13 0 0];

tap=ref_tap(num_register-1,:); temp=0;
for i=1:size(tap,2), if tap(i)>0, temp=temp+1; end; end;
size_tap=temp; num_stage=max(tap);

% Seed is assumed to be '1'.
state(1:num_stage)=1; p=[];p_final=[];

for index=1:2^num_stage-1,
  tot=0;
  for sub=1:size_tap,tot=XOR(tot,state(tap(sub))); end;
  state(1:num_stage)=[tot,state(1:num_stage-1)];
  p=[p;state(num_stage)];
end
return
```

----------SUBROUTINE 3----------

```
%-----------------------------------------------------------------------%
% Nyquist pulse generation and plotting
%  function usage ; Nyquist_pulse(alpha,pts, num_period);
%               Nyquist Roll-off factor             : alpha
%               Number of points in one period : pts
%                # of periods to calculate          : -num_period*T ~ num_period*T
```

```
%-----------------------------------------------------------------------%

function pulse=Nyquist_pulse(alpha, pts, num_period)
x=[];pulse=[];temp=[];

% Ref. IEEE journal of Light. Tech. Vol. 19, No. 9, pp.1263-1273, Sept. 2001.
% d_cycle means duty cycle of Return-to-Zero signal.
% If d_cycle is equal to '1', then the waveform becomes Nonreturn-to-Zero.
d_cycle=0.33;

for x=-num_period:1/pts:num_period,
  if alpha*d_cycle<x & x< d_cycle
     pulse=[pulse,1];
  elseif (0<=x&x<=alpha*d_cycle)|(d_cycle<=x&x<(1+alpha)*d_cycle)
    pulse=[pulse,(1-sin(pi/(alpha*d_cycle)*(abs(x-(1+alpha)/2*d_cycle)-1/2*d_cycle)))/2];
     else pulse=[pulse,0];
  end
end

% The Nyquist pulse drawing
pulse=pulse'; x=[-num_period:1/pts:num_period]'; figure;plot(x, pulse);
return
```

----------SUBROUTINE 4----------

```
%-----------------------------------------------------------------------%
% Eye waveform Drawing
% Function Usage ; eye_waveform(signal_sequence, period, pts, offset)
%               signal_sequence  :  signal column vector which stores signal waveform
%               period                  :     one cycle duration ( sec )
%               pts                     :     # of points in one period
%               offset                  :     offset time at which integer multiples of period start ( sec )
%-----------------------------------------------------------------------%
function eye_waveform(signal, period, pts, offset)

offset_pos=round(offset/(period/pts)); figure;hold on;

% 80 Gbps RZ
x=-2:1/pts:2;
for i=2:2:((size(signal,1)-1)/pts)-1,
  plot(x,signal([(i-2)*pts+1+offset_pos:(i+2)*pts+1+offset_pos],:));
end
hold off;
```

----------SUBROUTINE 5----------

```
%-----------------------------------------------------------------------%
% Sampling Process
% Function usage ; sampled_signal=sampling(signal, pulse_train)
%         signal          : input signal to sample
%         pulse_train     : impulse train
%-----------------------------------------------------------------------%
function sampled_signal=sampling(signal, pulse_train);

if ( size(signal,1)~=size(pulse_train,1)) error(' Two signal dimensions are different!!'); end
for i=1:size(signal,1),    sampled_signal(i)=signal(i)*pulse_train(i); end
return
```

----------SUBROUTINE 6----------

```
%-----------------------------------------------------------------------%
% Impulse response of the sampler
% transfer_sampler(t_sampling, pts,start_time, stop_time, offset)
%       t_sampling   ; sampling period ( sec )
%       pts          ; number of points in one sampling period
%       start_time   ; start time
%       stop_time    ; stop time
%       offset       ; # of time to make offset, nonnegative value.(sec)
%-----------------------------------------------------------------------%

function sample=transfer_sampler(t_sampling, pts, start_time, stop_time, offset);

% As a first example, let's assume that the transfer function of  the sampler is rectangular function. F(t)=rect(t/T)
% Practically, that should be replaced with the impulse response of the real diode sampler.
% impulse response initialization
impulse_response([1:pts],:)=0;

% pulse width of rectangular function ( # of samples ): pulse_width_time =(t_sampling/pts)*(pulse_width-1)
pulse_width=51;

for i=(pts/2)+1-(pulse_width-1)/2:(pts/2)+1+(pulse_width-1)/2,
  impulse_response(i,:)=1;
end

%.....................................................%
offset_pos=offset/(t_sampling/pts)+1;

sample=[];

for i=1:(stop_time)*pts/2/(size(impulse_response,1)),
  sample=[sample;impulse_response];
end
sample=[sample;0];

temp_sample([1:size(sample,1)],:)=0;
for i=1:size(sample),
  if(i+offset_pos>size(sample,1)) temp_pos=i+offset_pos-size(sample,1);
  else temp_pos=i+offset_pos;
  end
  temp_sample(temp_pos)=sample(i);
end
sample=temp_sample; x=start_time:2/pts:stop_time; plot(x,sample);
return
```

References

[1] S. Kawanishi, "High bit rate Transmission over 1 Tbit/s," *IEICE Trans. Commun.*, vol. E84-B, no.5, pp.1135-1141, May 2001.

[2] Greg Freeman, Jae-Sung Rieh, B. Jagannathan, Zhijian Yang, F. Guarin, A. Joseph, "Device scaling and application trends for over 200 GHz SiGe HBTs," *2003 Topical meeting on Silicon Monolithic Integrated Circuits in RF systems*, Garmisch, Germany, pp.6-9, 2003.

[3] M. Meghelli, "A 108Gb/s 4:1 multiplexer in 0.13 um SiGe-bipolar technology," *ISSCC 2004*, San Francisco, USA, 2004.

[4] A. Felder, M. Möller, M. Wurzer, M. Rest, T.F. Meister, and H.-M. Rein, "60 Gbit/s regenerating demultiplexer in SiGe bipolar technology," *Electronics. Lett.*, vol. 33, no. 23, pp.1984-1986, Nov. 1997.

[5] Mounir Meghelli, Alexander V. Rylyakov, and Lei Shan, "50-Gb/s SiGe BiCMOS 4 : 1 Multiplexer and 1 : 4 Demultiplexer for Serial Communication Systems," *IEEE Trans. Solid-State Circuits,* vol. 37, no. 12, pp.1790-1794*,* Dec. 2002.

[6] Daniel Kehrer, Hans-Dieter Wohlmuth, Herbert Knapp, Martin Wurzer, and Arpad L. Scholtz, "40-Gb/s 2:1 Multiplexer and 1:2 Demultiplexer in 120-nm Standard CMOS," *IEEE Trans. Solid-State Circuits,* vol. 38, no. 11, pp.1830-1837*,* Nov. 2003.

[7] Y. Suzuki, Y. Amamiya, Z. Yamazaki, S. Wada, H. Uchida, C. Kurioka, S. Tanaka, H. Hida, "110 Gb/s multiplexing and demultiplexing ICs," *ISSCC 2004*, San Francisco, USA, 2004.

[8] M. Schlechtweg, A. Leuther, A. Tessmann, C. Schwörer, H. Massler, W. Reinert, M. Lang, U. Nowontny, O. Kappeler, M. Walther, R. Lösch, "Millimeter-wave and mixed-signal integrated circuits based on advanced metamorphic HEMT Technology," *IPRM 2004*, pp.609-614, Kagoshima, Japan 2004.

[9] Peter Russer, "Si and SiGe Milimeter-Wave Integrated Circuits," *IEEE Trans. Microwave Theory and Tech.*, vol.MTT-46, no. 5, pp.590-603, May 1998.

[10] R. Pullela, U. Bhattacharya, S.T. Allen, M.J.W. Rodwell, "Multiplexer/demultiplexer IC technology for 100 Gb/s fiber-optic transmission," *IEEE Trans. Solid-State Circuits,* vol. 31, no. 5, pp.740-743*,* May 1996.

[11] T. H. Hu and P. R. Gray, "A monolithic 480 Mb/s parallel AGC/decision clock-recovery circuit in 1.2 μm CMOS," *IEEE Trans. Solid-State Circuits*, vol. 28, no. 12, pp.1314-1320, Dec. 1993.

[12] Mark Kahrs, "50 years of RF and microwave sampling," *IEEE Trans. Microwave Theory and Tech.*, vol.MTT-41, no. 6, pp.1787-1805, June 2003.

[13] F. X. Sinnesbichler, B. Hautz, G. R. Olbrich, "Low phase noise 58 GHz SiGe HBT push-push oscillator with simultaneous 29 GHz output," *IEEE MTT-S International Microwave Symposium Digest,* Boston, USA, pp. 35-38, 2000.

[14] Govind P. Agrawal, *Fiber Optic Communication Systems*, A Wiley-Interscience publication, NY, 1997.

[15] Govind P. Agrawal, *Nonlinear Fiber Optics*, Academic Press, USA, 2001.

[16] C.P. Sandbank, *Optical Fiber Communication Systems*, A Wiley-Interscience publication, 1980.

[17] Katsusuke Takima, Jian Zhou, Kazuhide Nakajima, Kiminori Sato, "Ultralow loss and long length photonic crystal fiber," *Journal of Lightwave Tech.*, vol. 22, no. 1, pp.7-10, Jan. 2004.

[18] Jake Bromage, "Raman amplification for fiber communications systems," *Journal of Lightwave Tech.*, vol. 22, no. 1, pp.79-93, Jan. 2004.

[19] Peter M. Krummrich, Erich Gottwald, Nancy E. Hecker, Cluas-Jörg Weiske, Andreas Schöpflin, Andreas Färbert, and Klaus Kotten, "40 Gbit/s ETDM for multi terabit/s long haul WDM transmission," *IEICE Trans. Commun.*, vol. E85-B, no. 2, Feb. 2002.

[20] Jae-Seung Lee, Chang-Sup Shim, "Bit-Error-Rate analysis of optically preamplified receivers using an eigenfunction expansion method in optical frequency domain," *Journal of Lightwave Tech.*, vol. 12, no. 7, pp.1224-1229, July 1994.

[21] L. Y. Lin, M. C. Wu, T. Itoh, T. A. Vang, R. E. Muller, D. L. Sivco, A. Y. Cho, "High-power high-speed photodetectors – design, analysis, and experimental demondtration,"

IEEE Trans. Microwave Theory and Tech., vol.MTT-45, no.8, pp.1320-1331, Aug. 1997.

[22] Kazutoshi Kato, "Ultrawide-band/high-frequency phtodetectors," *IEEE Trans. Microwave Theory and Tech.*, vol.MTT-47, no.7, pp.1265-1281, July 1999.

[23] Kazutoshi Kato, Susumu Hata, Kenji Kawano, Junichi Yoshida, and Atsuo Kozen, "A high-efficiency 50 GHz InGaAs multimode waveguide photodetector," *IEEE J. Quantum Electron.*, vol.28, no.12, pp.2728-2735, Dec. 1992.

[24] K. S. Giboney, R. L. Nagarajan, T. E. Reynolds, S. T. Allen, R. P. Mirin, M. J. W. Rodwell, and J. E. Bowers, "Travelling wave photodetectors with 172 GHz bandwidth and 76 GHz bandwidth-efficiency product," *IEEE Photonics Tech. Lett.*, vol.7, no.4, pp.412-414, April 1995.

[25] *Datasheet of photodetector* (model : XPDV) in u2t photonics AG.

[26] Mark C. Foisy, P.E. Jeroma, G.H. Martin, "Large-Signal Relaxation-Time Model for HEMTs and MESFETs," *IEEE International Microwave Symposium MTT-S Digest*, Albuquerque, New Mexico, pp.251-254, 1992.

[27] Robert R. Daniels, A.T. Yang, J.P. Harrang, "A universal large/small signal 3-terminal FET model using a nonquasi-static charge-based approach," *IEEE. Trans. Electron Devices*, vol.40, no.10, pp.1723-1729, Oct. 1993.

[28] David E. Root, "Measurement-based large signal diode modelling system for circuit and device design," *IEEE Trans. Microwave Theory and Tech.*, vol.MTT-41, no.12, pp.2211-2217, Dec. 1993.

[29] Y. Arai, M. Sato, H.T. Yamada, T. Hamada, K. Nagai, H. Fujishiro, "60 GHz Flip-Chip Assembled MIC Design Considering Chip-Substrate Effect," *IEEE Trans. Microwave Theory and Tech.*, vol.MTT-45, no.12, pp.2261-2266, Dec. 1997.

[30] Chun-Long Wang and Ruey-Beei Wu, "A locally matching technique for broadband flip-chip transition design," *IEEE International Microwave Symposium MTT-S Digest*, Seattle, Washington, pp.1397-1400, 2002.

[31] Peter J. Winzer, M. Pfennigbauer, M.M. Strasser, W.R. Leeb, "Optimum filter bandwidths for optically preamplified NRZ receivers," *Journal of Lightwave Tech.*, vol. 19, no. 9, pp.1263-1273, Sep. 2001.

[32] Benjamin Chan and Jan Conradi, "On the non-Gaussian noise in Erbium-doped fiber amplifiers," *Journal of Lightwave Tech.*, vol. 15, no. 4, pp.680-687, April 1997.

[33] Chris Lawets and John C. Cartledge, "Performance of optically preamplified receivers with Fabry-Perot optical filters," *Journal of Lightwave Tech.*, vol. 14, no.11, pp.2467-2474, Nov. 1996.

[34] Stamatios V. Kartalopoulos, *Introduction to DWDM technology*, IEEE press, 2000.

[35] Martin Pfennigbauer, Martin Pauer, Peter J. Winzer and Martin M. Strasser, "Performance optimization of optically preamplified revievers for return-to-zero and non return-to-zero coding," *AEÜ Int. J. Electron. Commun.*, 56, no.4, pp.261-267, 2002.

[36] Athanasios Papoulis, S. Unnikrishna Pillai, *Probability, Random variables and stochastic processes*, 4Th Ed., McGraw-Hill, 2002.

[37] Peter J. Winzer, "Shot-noise formula for time-varying photon rates: a general derivation," *J. Opt. Soc. Am. B*, vol.14, no.10, pp.2424-2429, Oct. 1997.

[38] Peter J. Winzer, "Linking equations between photon statistics and photocurrent statistics for time-varying stochastic photon rates," *Quantum Semiclass. Opt.*, no.10, pp. 643-655, 1998.

[39] Mandel and Wolf, *Optical coherence and quantum optics*, Cambridge University Press, 1995.

[40] Athanasios Papoulis, S. Unnikrishna Pillai, *Probability, random variables, and stochastic processes*, 4th Ed., McGraw-Hill, Inc., 2002.

[41] Bahaa E.A. Saleh, Malvin Carl Teich, *Fundamental of photonics*, John Wiley & Sons, Inc., 1991.

[42] L. Möller *et al.*, "ISI mitigation using decision feedback loop demonstrated with PMD distorted 10Gbit/s signals," *Electronics. Lett.* , vol. 35, no. 24, pp. 2092-2093, Nov. 1999.

[43] Hussein H. M. Ghouz, EL-Badawy EL-Sharawy, "An accurate equivalent circuit model of flip chip and via interconnects," *IEEE Trans. Microwave Theory and Tech.*, vol. MTT-44, no. 12, pp.2543-2554, Dec. 1996.

[44] Dylan F. Williams, Kate A. Remley, "Analytic sampling-circuit model," *IEEE Trans. Microwave Theory and Tech.*, vol. MTT-49, no. 6, pp.1013-1019, June 2001.

[45] Dylan F. Williams, Kate A. Remley, and Donald DeGrrot, "Nose-to-nose response of a 20-GHz sampling circuit," 54th *ARFTG Conf. Dig.*, Dec. 1999.

[46] Andrea Jentzsch and Wolfgang Heinrich, "Theory and measurements of flip-chip interconnects for frequencies up to 100 GHz," *IEEE Trans. Microwave Theory and Tech.*, vol. MTT-49, no. 5, pp.871-877, May 2001.

[47] Peter J. Winzer and András Klamár, "Sensitivity enhancement of optical receivers by impulsive coding," *Jounrnal of Lightwave Tech.*, vol. 17, no. 2, pp.171-177, Feb. 1999.

[48] Q. Lee, S.C. Martin, D. Mensa, R.P. Smith, J. Guthrie, S. Jaganathan, Y. Betser, T. Mathew, S. Krishnan, L. Samoska, and M.J.W. Rodwell, "Submicron-Transferred-Substrate Heterojunction Bipolar Transistors with Greater than 1 THz f*max*," *57th Device Research Conference*, University of California, Santa Barbara, CA, pp. 28-30, June 1999.

[49] D. E. Johnson, J. R. Johnson, and H. P. Moore, *A Handbook of Active Filters*, Englewood Cliffs, NJ, Prentice Hall, 1980.

[50] Jack H. Winters, Richard D. Gitlin, and Sanjay Kasturia, "Reducing the effects of transmission impairments in digital fiber optic systems," *IEEE Comm. Magazine*, pp.68-76, June 1993.

[51] John G. Proakis, *Digital communications*, 3rd Ed., McGraw-Hill, 1995.

[52] Datasheets of 104P linear power amplifier, SHF communication Technologies AG.

[53] Dieter Schlump, Berthold Wedding, Henning Bülow, "Electronic equalisation of PMD and chromatic dispersion induced distortion after 100 km standard fibre at 10 Gbit/s," *ECOC 98*, pp.20-24, Madrid, Spain, Sept. 1998.

[54] Jack H. Winters, and Mario A. Santoro, "Experimental equalization of polarization dispersion," *IEEE Photonics Tech. Lett.*, vol. 2, no. 8, pp.591-593, Aug. 1990.

[55] Jack H. Winters, and Richard D. Giltin, "Electrical signal processing technique in lonh-haul fiber-optic systems," *IEEE Trans. Comm.*, vol 38, no. 9, pp.1439-1453, Sept. 1990.

[56] Jack H. Winters, and Sanjay Kasturia, "Adaptive nonlinear cancellation for high-speed fiber-optic systems," *Jounrnal of Lightwave Tech.*, vol. 10, no. , pp. 971-977, July 1992.

[57] Jack H. Winters, Richard D. Gitlin, and Sanjay Kasturia, "Reducing the effects of transmission impairments in digital fiber optic systems," *IEEE Comm. Magazine*, pp.68-76, June 1993.

[58] *Data sheets of BAT14-077D and BAT14-077S,* Infineon technologies.

[59] Kate A. Remley, Dylan F. Williams, Donald C. DeGroot, Jan Verspecht, and John Kerley, "Effects of nonlinear diode junction capacitance on the nose-to-nose calibration," *IEEE Micro. Wireless Comp. Lett.*, vol. 11, Issue 5, pp.196-198, May 2001.

[60] IC-CAP Characterization & Modeling Handbook, *Modeling a Diode*, Chapter 6., Agilent Technologies.

[61] Internal Report, *Messungen zum Mischerverhalten von Silizium-Schottky-Dioden BAT14-077D*, Infineon, 1998.

[62] A. N. Gerkis, "Broadband impedance matching using the real frequency network systhesis technique," *Applied Microwave & Wireless*, vol. 10, no. 6, pp.26-32, July 1998.

[63] Jung Han Choi, Gerhard R. Olbrich, Peter Russer, *80 Gbit/s ETDM optical receiver*, Final report, *Bundesministerium für Bildung und Forschung (BMBF) project*, contract number 01 BP 156.

[64] Septiaji Eko Nugroho, *Design, analysis and simulation of a Si Schottky diode based sampling circuit for 40 Gbps ETDM demultiplexer circuit*, master thesis, Institute for High-frequency Engineering, Munich University of Technology, Oct. 2003.

[65] T. Krems, A. Tessmann, and W.H. Haydl, “Avoiding cross talk and feedback effects in packaging coplanar mm-wave circuits,” *IEEE MTT-S Int. Microwave Symp. Dig.*, pp.1091-1094, June 1998.

[66] Reinhold Ludwig, Pavel Bretchko, *RF circuit design: Theory and applications*, Prentice-Hall, New Jersey, 2000.

[67] W.H. Haydl, “On the used of vias in conductor-backed coplanar circuits,” *IEEE Trans. Microwave Theory Tech.*, vol. MTT-50, no. 6, pp.1571-1577, June 2002.

[68] K. Beilenhoff and W. Heinrich, “Excitation of the parasitic parallel-plate line mode at coplanar discontinuities,” *IEEE MTT-S Int. Microwave Symp. Dig.*, pp.1789-1792, June 1997.

[69] M. Yu, R. Vahldieck, and J. Huang, “Comparing coax launcher and wafer probe excitation for 10 mil conductor-backed CPW with via holes and air bridges,” *IEEE MTT-S Int. Microwave Symp. Dig.*, pp.705-708, June 1993.

[70] Michael Y. Frankel, Shantanu Gupta, Janis A. Valdmanis, and Gerard A. Mourou, “Terahertz attenuation and dispersion characteristics of coplanar transmission lines,” *IEEE Trans. Microwave Theory Tech.*, vol.MTT-39, no. 6, pp.910-916, June 1991.

[71] Martin C. Nuss ans Keith W. Goossen, “Investigtion of high-temperature superconductors with terahertz bandwidth electrical pulses,” *IEEE J. Quantum Electron.*, vol.25, no.12, pp.2596-2607, Dec. 1989.

[72] D. S. Phatak, and A.P.Defonzo, “Dispersion characteristics of optically exicted coplanar striplines: pulse propagation,” *IEEE Trans. Microwave Theory Tech.*, vol. MTT-38, no. 5, pp. 654-661, May 1990.

[73] William R. Eisenstadt, and Yungseon Eo, “S-parameter-based IC Interconnect transmission line characterization,” *IEEE Trans. Components, hybrids, and manufacturing Tech.*, vol.15, no. 4, pp.483-490, Aug. 1992.

[74] K.C. Gupta, Ramesh Garg, and Rakesh chadha, *Computer-aided design of microwave circuits*, Artech-House, 1981.

[75] Hugh Hildreth Skilling, *Electrical engineering circuits*, John Wiley & Sons, Inc., 1959.

[76] *DC-65 GHz Integrated V connectors*. *Anritsu* Preliminary Technical Data Sheet.

[77] Picosecond Pulse Labs, *Application Note AN-4*, 1989.